Measurement of low-mass e^+e^- pair production in 2 AGeV C-C collisions with HADES

Dissertation
zur Erlangung des Doktorgrades
der Naturwissenschaften

vorgelegt am Fachbereich Physik
der Johann Wolfgang Goethe-Universität
in Frankfurt am Main

von
Małgorzata Sudoł
aus Stalowa Wola

Frankfurt 2007
(D 30)

vom Fachbereich Physik der
Johann Wolfgang Goethe-Universität als Dissertation angenommen.

Dekan:	Prof. Dr. W. Assmus
Gutachter:	Prof. Dr. J. Stroth
Datum der Disputation:	

Kurzfassung

Eines der Hauptziele der modernen Kernphysik ist die Untersuchung der Modifikation von Eigenschaften von Hadronen bei normaler und hoher Temperatur und Dichte. Dileptonen-Experimente liefern interessante Ergebnisse und geben einen Einblick in die Eigenschaften der starken Wechselwirkung und in die Natur der Massenerzeugung von Hadronen. Eines dieser Forschungswerkzeuge ist das HADES Spektrometer. HADES ist ein Dileptonen Spektrometer mit hoher Akzeptanz am Schwerionensynchroton der GSI in Darmstadt. Die wesentliche physikalische Motivation des Experiments ist, e^+e^- -Paare im invarianten Massenbereich bis 1 GeV/c^2, sowohl in pion- und protoninduzierten Reaktionen, als auch in Schwerionenkollisionen zu messen. Das Ziel ist die Untersuchung der Eigenschaften der Vektormesonen ρ, ω und anderer Hadronen, welche aus e^+e^- -Paare rekonstruiert werden. Da Dileptonen nicht durch die starke Wechselwirkung beeinflusst werden, machen sie das Studium der Eigenschaften von Hadronen in Kernmaterie möglich. Allerdings ist die Messung dieser Dileptonenpaare schwierig, da Leptonen, die in anderen Prozessen erzeugt werden, einen großen Untergrund erzeugen.

In dieser Arbeit werden die Analyse von Daten, die mit dem HADES Spektrometer aufgenommen wurden, so wie Resultate derselben, diskutiert. Zum ersten Mal wurden mit ausreichender Statistik e^+e^--Paare aufgezeichnet, die in der Kollision C+C bei einer Projektilenergie von 2 GeV per Nukleon erzeugt wurden. Dieses erste Experiment der HADES Kollaboration, da es ermöglicht, den von der DLS Kollaboration bei 1.04 AGeV gemessenen Paar-Überschuss zu verifizieren.

Das erste Kapitel beschreibt die dieser Arbeit zugrunde liegende Physik. Im zweiten Kapitel wird das HADES Spektrometer mit den typischen Eigenschaften der einzelnen Komponenten vorgestellt. Kapitel 3 fokussiert das Thema der Identifikation von geladenen Teilchen. Das 4. Kapitel präsentiert die Rekonstruktion von Dielektronen-Spektren in C+C Kollisionen. In diesem Teil der Arbeit wird auch der Vergleich mit theoretischen Modellen berücksichtigt. Die Schlussfolgerung befinden sich im Kapitel 5.

Abstract

The search for a modification of hadron properties inside nuclear matter at normal and/or high temperature and density is one of the most interesting issues of modern nuclear physics. Dilepton experiments, give insight into the properties of strong interaction and the nature of hadron mass generation.

One of these research tools is the HADES spectrometer. HADES is a high acceptance dilepton spectrometer installed at the heavy-ion synchrotron (SIS) at GSI, Darmstadt. The main physics motivation of HADES is the measurement of e^+e^- pairs in the invariant-mass range up to 1 GeV/c^2 in pion- and proton-induced reactions, as well as in heavy-ion collisions. The goal is to investigate the properties of the vector mesons ρ, ω and of other hadrons reconstructed from e^+e^- decay pairs. Dileptons are penetrating probes allowing to study the in-medium properties of hadrons. However, the measurement of such dilepton pairs is difficult because of a very large background from other processes in which leptons are created.

This thesis presents the analysis of the data provided by the first physics run with the HADES spectrometer. For the first time e^+e^- pairs produced in C+C collisions at an incident energy of 2 GeV per nucleon have been collected with sufficient statistics.

This experiment is of particular importance since it allows to address the puzzling pair excess measured by the former DLS experiment at a beam energy 1.04 AGeV.

The thesis consists of five chapters. The first chapter presents the physics case which is addressed in the work. In the second chapter the HADES spectrometer is introduced with the characteristic of specific detectors which are part of the spectrometer. Chapter three focusses on the issue of charged-particle identification. The fourth chapter discusses the reconstruction of the di-electron spectra in C+C collisions. In this part of the thesis a comparison with theoretical models is included as well. The conclusion and final remarks are given in chapter five.

Contents

Contents i

List of Figures iii

List of Tables vi

1 Introduction 1
- 1.1 Motivation for studying vector mesons . . . 3
- 1.2 Dilepton spectroscopy . . . 4
  - 1.2.1 Ultrarelativistic heavy-ion collisions . . . 5
  - 1.2.2 Low-energy dilepton spectroscopy . . . 7
- 1.3 Overview of the present work . . . 10

2 The HADES spectrometer 12
- 2.1 Start and veto detectors . . . 14
- 2.2 The Ring Imaging Cherenkov Detector . . . 15
- 2.3 The MDC Detectors . . . 16
- 2.4 The Superconducting Magnet . . . 17
- 2.5 The multiplicity electron trigger array detectors . . . 18
  - 2.5.1 The TOF Detector . . . 18
  - 2.5.2 The TOFINO detector . . . 20
  - 2.5.3 The Pre-Shower Detector . . . 20
- 2.6 Trigger System . . . 21
  - 2.6.1 First level trigger . . . 21
  - 2.6.2 Second level trigger . . . 22
- 2.7 Characteristics of the data set - NOVEMBER 2002 . . . 24

3 Single lepton analysis 27
- 3.1 Introduction . . . 27
- 3.2 Low-resolution momentum reconstruction . . . 29
- 3.3 Identification of the single lepton tracks in RICH detector . . . 32
- 3.4 Spatial correlation of the RICH hits and the inner MDCs segment . . . 35

3.5 Lepton identification in the Pre-Shower detector 36
3.6 Time-of-flight cut 39
3.7 Results 40

4 Dilepton analysis **49**
4.1 Introduction 49
4.2 Origin of the background 50
4.3 Reconstruction of the background 51
4.4 Background rejection strategy 57
4.5 Efficiency corrections. 66
4.6 Systematic error estimation 67
4.7 Normalization 68
4.8 Comparison of the HADES data with the PLUTO event generator 69

5 Physics results and discussion. **74**
5.1 Comparison of the HADES data with transport models. 74
5.2 The DLS recall 81

6 Conclusions **85**

7 Zusammenfassung **87**

A The PLUTO event generator **91**

B Investigation of the systematic errors introduced by the reconstruction method **95**

C Geometrical acceptance **100**

D Study of the LVL2 trigger efficiency **102**

E Matching windows **106**

Bibliography **111**

List of Figures

1.1 Schematic phase space diagram of strongly interacting matter. 2
1.2 Status of the dilepton experiments. 4
1.3 Inclusive e^+e^- invariant-mass spectrum for Pb+Au collision at 158 AGeV, CERES 5
1.4 Excess spectra in the Pb+Au at 158 AGeV - CERES collaboration 6
1.5 Results of the NA60 experiment. 7
1.6 Schematic view of the DLS spectrometer. 8
1.7 Comparison of the DLS results with the theory for C+C and Ca+Ca at 1.04 AGeV. 8
1.8 Comparison of the DLS data with the RQMD model. 9
1.9 Experimental results of the E325. 10

2.1 The HADES spectrometer 12
2.2 Start and Veto detectors 14
2.3 Schematic cross-section of the RICH detector 15
2.4 Schematic layout of the HADES tracking system 17
2.5 The Superconducting Magnet - ILSE 18
2.6 Schematic view of the META detectors 19
2.7 Schematic view of the Pre-Shower detector (one sector) 21
2.8 Schematic view of the HADES multi-level trigger system 22
2.9 Schematic view of the events selection used for the data acquisition 23
2.10 Schematic view of the sub-detectors in experiment in NOV02. 24
2.11 Impact parameter distribution of C+C@2AGeV in UrQMD. 25
2.12 Statistics collected during each day of the experiment. 26

3.1 Schematic view of the analysis flow. 28
3.2 Schematic view of the HADES spectrometer. 29
3.3 Momentum resolution of the low resolution method 30
3.4 xPull distribution of the kick plane algorithm. 31
3.5 Schematic of the hough transformation. 32
3.6 Schematic of the pattern matrix method. 33
3.7 Spatial correlation between RICH hits and inner MDCs segment 35
3.8 Angular correlation between RICH rings and MDC's segments. 36

3.9 Schematic view of the electromagnetic shower identification in the Pre-Shower. 37
3.10 Pre-Shower parametrization. 38
3.11 β calculated in the TOFINO detector in two momentum bins 39
3.12 β calculated in the TOF detector in two momentum bins 40
3.13 Momentum distribution of the lepton candidates. 41
3.14 Reconstructed distribution of the azimuthal emission angle for positrons and electrons separately in the experiment and simulation. 42
3.15 Reconstructed distribution of the polar emission angle for positrons and electrons separately in the experiment and simulation. 43
3.16 Reconstructed distribution of the momenta for positrons and electrons separately in the experiment and simulation. 44
3.17 Efficiency and purity of the lepton sample after all applied cuts 46
3.18 Schematic view of the wrongly identify leptons. 47
3.19 Lepton multiplicities in the experiment and simulation. 47
3.20 Correlation of electron and positron multiplicities per event. 48

4.1 Invariant mass distribution for the like-sign and unlike-sign pairs. 50
4.2 Example of the combinatorial pairs. 51
4.3 Example of a correlated combinatorial pair. 52
4.4 Comparison between the like-sign (e^-e^-) and mixed event background 54
4.5 Comparison between the like-sign (e^+e^+) and mixed event background 55
4.6 Comparison between the like-sign and mixed event background 56
4.7 Schematic view of the pair classification 57
4.8 Schematic view of the pair classification 58
4.9 Schematic way of the direct and recursive way of cutting. 59
4.10 Opening angle distribution for various lepton sources. 60
4.11 Pair cuts 61
4.12 Comparison of the true signal with the reconstructed one and background in the analysis. 61
4.13 Purity of the pair signal as function of the invariant mass. 62
4.14 Comparison of the uncorrected pair spectra 62
4.15 Signal-to-background ratio as a function of invariant mass. 63
4.16 Reduction of the experimental signal and background as a cut number 65
4.17 Efficiency corrections for single leptons. 66
4.18 Comparison of the invariant mass spectrum before and after efficiency correction. 67
4.19 Comparison of the HADES dilepton mass spectrum to the PLUTO cocktail A. . 70
4.20 Comparison of the HADES dilepton mass spectrum to the full PLUTO cocktail. 71
4.21 Comparison of the rapidity distribution between the experimental data and the PLUTO simulation 72
4.22 Comparison of the HADES data to the PLUTO cocktail as a function of $P_\perp$ . . 73

5.1 Experimental data compared to transport model cocktails composed of free π^0 and η decays. 75

5.2 Comparison of the efficiency corrected HADES data with the vacuum calculation of the transport models . . . 76
5.3 Comparison of the rapidity distribution between experimental data and HSD model calculation . . . 77
5.4 Comparison of the P⊥ distribution between experimental data and HSD model calculation . . . 78
5.5 Ratio of the experimental data and transport model calculations to PLUTO cocktail A . . . 79
5.6 Comparison of the efficiency corrected HADES data with the in-medium calculation of the transport models . . . 80
5.7 Comparison of the HADES data with vacuum and in-medium cocktails of HSD and RQMD transport models. . . . 81
5.8 Comparison of the experimental results with the η contribution. . . . 82
5.9 Scaling of the excess dielectron multiplicities as a function of beam energy. . . . 83

6.1 Comparison of the experimental invariant mass spectrum with new HSD calculations . . . 86

A.1 TAPS cross sections . . . 92
A.2 Schematic view for the $m_T - scaling$ . . . 93
A.3 Invariant mass spectrum for different parametrization . . . 94
A.4 Transverse momentum and rapidity for different parametrization . . . 94

B.1 Self-consistency check . . . 96
B.2 Angular dependence of the signal pairs as a function of opening angle . . . 97
B.3 Self consistency check after all corrections have been applied . . . 98
B.4 Systematic error from the efficiency correction . . . 99

C.1 Geometrical acceptance. . . . 101
C.2 Acceptance for e^+e^- pairs . . . 101

D.1 Comparison of the azimuthal angle distribution for leptons inside LVL1 and LVL2 events. . . . 103
D.2 Comparison of the polar angle distribution for leptons inside LVL1 and LVL2 events. . . . 104
D.3 Comparison of the dilepton spectra for LVL1 and LVL2 trigger based analysis . 105

E.1 Comparison of the theoretical and experimental widths of the signal. . . . 107
E.2 Azimuthal correlation of RICH and inner MDC hits for all sectors together as a function of momentum . . . 108
E.3 Polar correlation of RICH and inner MDC hits for all sectors together as a function of momentum . . . 109

List of Tables

1.1 Characteristic quantities of light vector mesons. 3

3.1 Cut efficiency of the single-lepton candidates in the experiment. 41

4.1 Reduction of the true signal with the cut number in simulation. 64
4.2 Reduction of the signal and the combinatorial background with the cut number for experimental data. 65
4.3 Multiplicities of charged pions in the HADES acceptance. Quoted errors are systematical only, statistical ones are negligible. 69
4.4 Transverse momentum ($P_\perp$) and rapidity (Y) integrated yields. 71

5.1 Derived enhancement factor for the DLS and HADES measurements. 83

A.1 Inverse slope parameters for C+C at 1 and 2 AGeV energies [1]. 92

D.1 Second level efficiency for leptons in both systems. 102

E.1 Radiation length and multiple scattering angle of the radiator components in the RICH detector for electrons with momentum p=0.5 GeV/c. 106

Chapter 1

Introduction

The investigation of the properties of nuclear matter over a wide range of temperature and density is one of the major topics of contemporary nuclear physics. A common goal of experiments in this context is the investigation of the equation of state (EOS), which is of fundamental importance, not only for nuclear physics, but is also required for a deeper understanding of astrophysical processes related to the final phase of the stellar evolution.

When nuclear matter is heated and/or compressed, initially confined quarks and gluons start to percolate between hadrons to be ultimately liberated. This phase transition to a plasma of deconfined quarks and gluons is accompanied by a melting of the quark condensate indicating chiral symmetry restoration. Even before the critical region is approached, the chiral symmetry of QCD is partially restored by the presence of hadrons. This has originally provided the basis for models of the quark-hadron transition, which has been confirmed numerically by the **q**uantum **c**hromo**d**ynamics (QCD) solved on the lattice for finite temperature.

The various states of matter that can be accessed by a proper selection of collision system and energy are schematically shown in Fig. 1.1 [4, 8]. For heavy-ion collisions at low energies of 1-2 AGeV accessible at the GSI[1] SIS[2] facility and formerly at the BEVALAC, a baryon density of 3-4 times larger than normal nuclear density and temperatures of the order of order 100 MeV can be achieved in a fireball with a mean lifetime of $\tau \sim 10$ fm/c [9, 10]. At higher beam energies, beyond 10 AGeV, temperatures of the chemical freeze-out approaching the critical temperature T_c were achieved, as indicated by data points extracted from the AGS experiments at BNL [4, 5]. At 30-200 AGeV beam energy accessible at SPS[3] in CERN a matter dominated by pions and by a low or vanishing net baryon density near the transition point is investigated. At the highest available energies at RHIC[4] and, in the near future at LHC[5], the quark-gluon phase of nuclear matter can be explored systematically.

[1] Gesellschaft für Schwerionenforgung
[2] SchwerIonen Synchrotron
[3] Super Proton Synchotron
[4] Relativistic Heavy-Ion Collider
[5] Large Hadron Collider

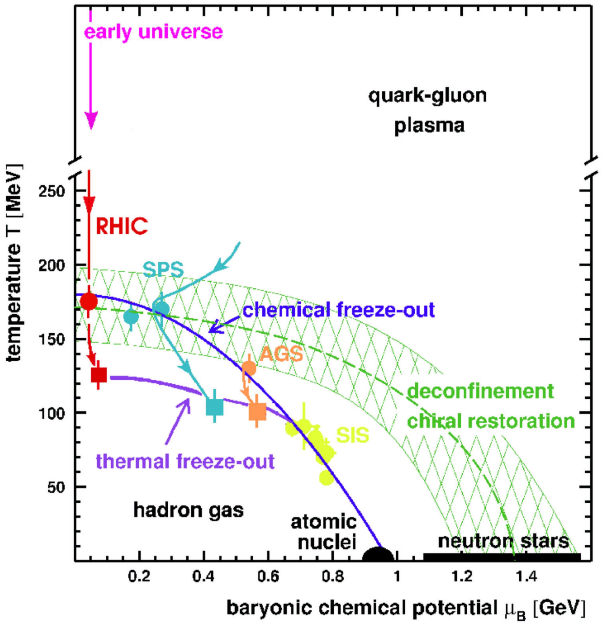

Figure 1.1: Schematic phase-diagram of strongly interacting matter on the T - μ_B plane. Depicted are lines of chemical and thermal (kinetic) freeze-out [2] within the framework of a statistical model, together with corresponding results from various collision energies available at existing accelerators [3, 2, 4, 5, 6, 7]. The chemical freeze-out parameters are deduced from hadron yields, while the thermal freeze-out parameters result from analysis of transverse momentum spectra. The crosshatched area indicates the region of the onset of deconfinement and chiral symmetry restoration.

Lattice QCD predicts the phase transition between a hadron gas and a quark-gluon plasma, where quarks and gluons become deconfined (this transition is expected at T $\sim$ 170 MeV for μ_B=0 and T=0 for μ_B > 1), as shown in the diagram as hatched area. The 'confined phase' consists of an interacting gas of hadrons, while the 'deconfined' phase can be interpreted as a dense liquid of quarks and gluons. Also the chemical and thermal freeze-out curves are marked by blue lines on this diagram. Chemical freeze-out refers to the stage where the fireball acquires its final particle composition, while thermal freeze-out refers to the stage where also elastic collisions cease and the final momenta are fixed. The chemical freeze-out is calculated under the assumption of thermodynamical equilibrium [3], via an hydro-chemical analysis of the particle species.

The chemical and thermal freeze-out curves merge at SIS energies. The corresponding matter state is clearly within the confinement region. In this energy regime, the achieved state of strongly interacting matter consists of nucleons which are excited into bayronic resonance states to a substantial fraction, along with accompanying meson production, mainly pions. At this density (up to $\rho \simeq 3\,\rho_0$) one expects a trend towards chiral symmetry restoration, that implies a decrease of the scalar quark condensate [11] with increasing temperature and density. As a result one should expect that some properties of light hadrons, such as their masses, spectral functions and their couplings, change considerably in the nuclear environment. Since the quark condensate is sensitive to changes of the density, one expects valuable insight into its properties at SIS energies.

1.1 Motivation for studying vector mesons

Vector mesons are suitable probes for investigating the hot and dense states of nuclear matter, since their lifetime is compatible with the lifetime of the fireball they are produced in and can therefore provide information about it. The ρ meson is of particular interest since, due to its even shorter lifetime, it is considered the ideal probe for in-medium effects. Its lifetime is indeed very short in comparison to the typical lifetime of the fireball, so that the ρ meson decays mostly inside the fireball (see Tab. 1.1). On the contrary, assuming the free (vacuum) decay width the ω and ϕ mesons decay mostly outside of the high density region.

meson	mass (MeV/c^2)	width (MeV/c^2)	lifetime τ (fm/c)	e^+e^- branching ratios
ρ	768	152	1.3	4.4×10^{-5}
ω	782	8.43	23.4	7.2×10^{-5}
ϕ	1019	4.43	44.4	3.1×10^{-4}

Table 1.1: Characteristic quantities of light vector mesons.

Since dileptons interact only electromagnetically and weakly, they have a long mean free path much larger than the size of the system. They are produced during the entire space-time evolution of the system, beginning at the early, hot stage. Thus, they carry information from the interior of strongly interacting matter to the outside world, and bring forth information not accessible by measuring purely hadronic final states.

Based on a effective chiral Lagrangian with incorporation of QCD scaling, a 30 $\%$ reduction of the ρ mass at normal ground state density (ρ_0 = 0.17 cm^{-3}) has been deduced [12]. And the mass of the vector mesons ρ and ω would be reduced by:

$$M_\rho = M_{\rho_o}\sqrt{1 - 0.3(\rho/\rho_o)} \tag{1.1}$$

i.e. 16$\%$ corresponding to about 130MeV/c^2 [13, 14].

Simple extrapolation to higher density would indicate that the chiral symmetry should be restored at $\rho = 3\rho_o$. In this context hadron mass modifications were proposed as a key observable for the chiral symmetry restoration when temperature and/or density of nuclear matter is increased.

More specifically, QCD sum rules [15, 16, 17, 18] and hadronic models [19, 20, 21, 8] predict significant changes in mass and resonance width of vector mesons, when embedded into nuclear matter. Models based on a mean-field approach or constituent quark models [12, 22, 23] predict such changes too.

1.2 Dilepton spectroscopy

Experimentally, electromagnetic decays of the vector mesons are rare probes due to their small branching ratio. In Tab. 1.1 are listed the main decay of vector mesons and their branching ratios. Di-electron spectroscopy is experimentally very challenging due to several reasons. There are strong competing background processes generating di-electrons like: NN bremsstrahlung and Dalitz decays of the Δ resonance, π^0 and η. These decays dominate e^+e^- pair production in the small invariant-mass region. Since dileptons are monitoring the full time evolution of strongly interacting matter, the observed spectra consist of a convolution of all stages with the respective emission strength, making an interpretation of the results difficult.

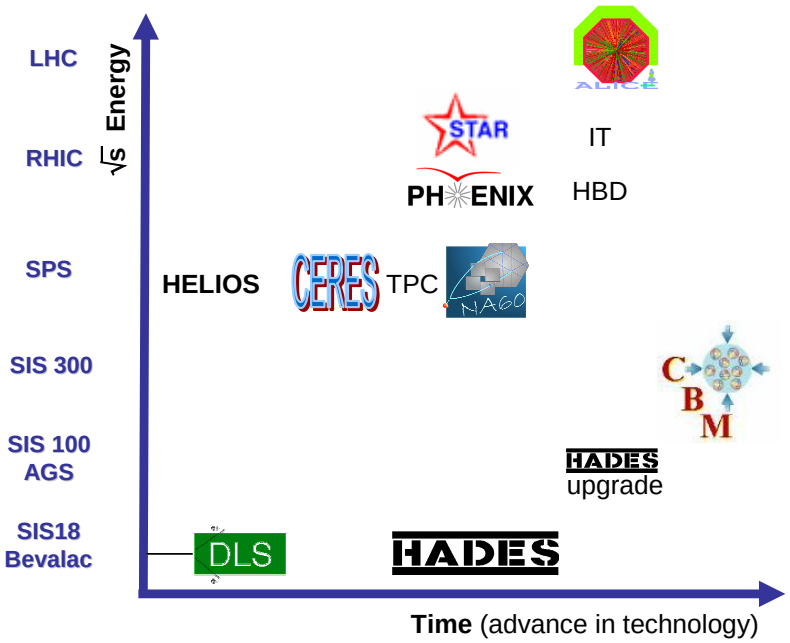

Figure 1.2: Status of the dilepton experiments as a function of time and c.m. energy.

The experimental efforts to establish the presence of *in-medium* effects have followed three main approaches by exploiting: hadronic probes in heavy-ion collisions, leptonic probes in heavy-ion collisions and photon induced reactions. Attention is focussed here only on leptonic probes as the HADES spectrometer is devoted to their detection. Figure 1.2 depict heavy-ion dilepton experiments grouped according to the c.m. energy used and the time period they were/are operational.

1.2.1 Ultrarelativistic heavy-ion collisions

The CERES experiment

The CERES experiment at CERN-SPS has completed a systematic physics program including the measurement of electron pairs in p-Be and p-Au at 450 AGeV, S-Au at 200 AGeV and Pb-Au at 158 AGeV and 40 AGeV. Fig. 1.3 shows the latest results of the invariant-mass spectrum from the analysis of Pb+Au at 158 AGeV in comparison to a hadronic cocktail [24] (left panel).

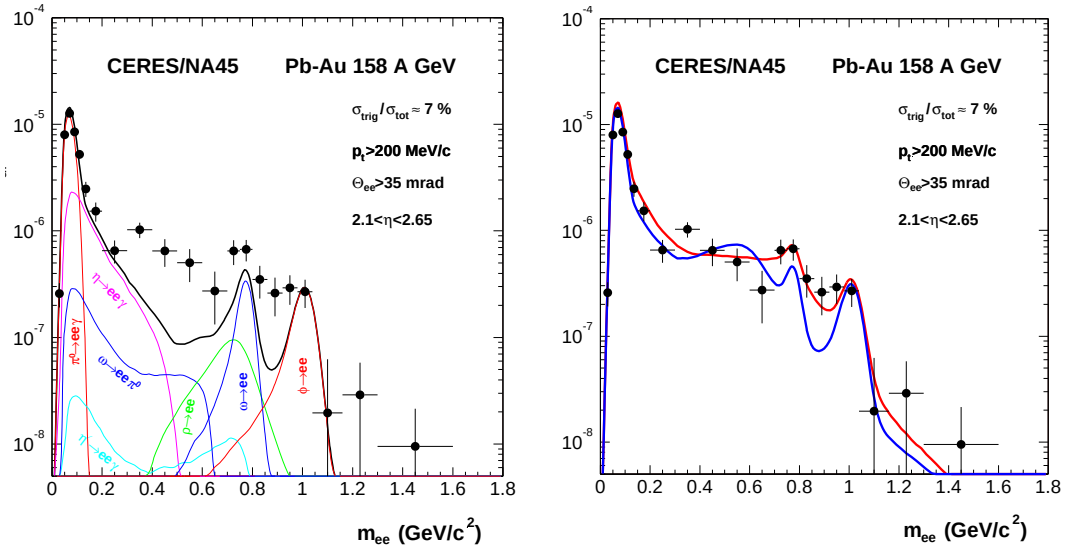

(a) hadronic cocktail (b) full calculations

Figure 1.3: Inclusive e^+e^- invariant-mass spectrum for Pb+Au collision at 158 AGeV [24].

Obtained invariant-mass spectrum is shown in Fig. 1.3 - left panel) together with the hadronic cocktail. For masses above the π^o Dalitz peak ($0.2 < m_{ee} < 1.1$ GeV/c^2) the yield exceeds the cocktail by a factor of 2.58 ± 0.32 [stat] $\pm$ 0.41 [syst] $\pm$ 0.77 [decay]. The enhancement is mostly pronounced in the mass region $0.2 < m_{ee} < 0.6$ GeV/c^2. Comparison of these data with a full theoretical calculation is presented in Fig. 1.3 (right panel). The dropping-mass scenario (blue line), which assumes a shift of the in-medium ρ mass [12, 25, 26], and the broadening scenario (red line) where the ρ spectral function is smeared due to the coupling to the hadronic medium [8, 27] have been taken into account. Both calculations described the mass region $0.2 < m_{ee} < 0.6$ GeV/c^2 reasonably well, however, for masses above (ω and ϕ region) the broadening scenario clearly fits the data better than the dropping-mass scenario.

In order to exhibit the shape of the in-medium contribution, the hadronic cocktail can be subtracted (except of the ρ vector meson), both from the experimental data as well as from the theoretical calculations. The result is shown in Fig. 1.4 [28].

After subtraction of the cocktail the data exhibit a very broad structure reaching to the lowest masses. The broadening scenario describes quite well the yield and shape of the excess,

while the dropping mass scenario is not at all consistent with it.

The NA60 experiment

The NA60 apparatus combines the muon spectrometer previously used by the NA50 experiment and a newly added telescope of radiation-tolerant silicon pixel detectors. The research programm of the NA60 experiment is very broad. One of the goal is to investigate the excess emission of lepton pairs for masses below the ρ meson.

Compared to the results of the CERES experiment, NA60 has been able to improve the statistical accuracy by a factor of more than 1000 and the mass resolution by a factor of 2-3. The experimental setup has an excellent mass resolution of 20 MeV/c^2 at the ω meson mass. This allowed for the first time in nuclear collisions to completely resolve the ω and ϕ vector mesons in the dilepton channel and to isolate the excess by substraction of the expected sources (cocktail). The remaining di-muon invariant-mass yield is attributed mainly to the $\rho \rightarrow \mu^+\mu^-$ decay.

NA60 studied In+In collisions at 158 AGeV [29, 30]. The final signal after background subtraction in comparison to the hadronic cocktail is shown in Fig. 1.5 (left panel). The analysis of the data is done in four classes of collision centrality: peripheral, semiperipheral, semicentral and central. Theoretical predictions taking into account a broadening [8, 31, 20] or shifting-mass [12, 25, 26] of the ρ vector meson are compared with the data for the semicentral bin (Fig. 1.5, right panel).

Just like in the CERES experiment, the broadening scenario appears to be more realistic, whereas the vacuum ρ and shifting-mass scenario is ruled out. The mass region above 0.9 GeV/c^2 can be explained by 4 π annihilation and other processes [27, 32, 33].

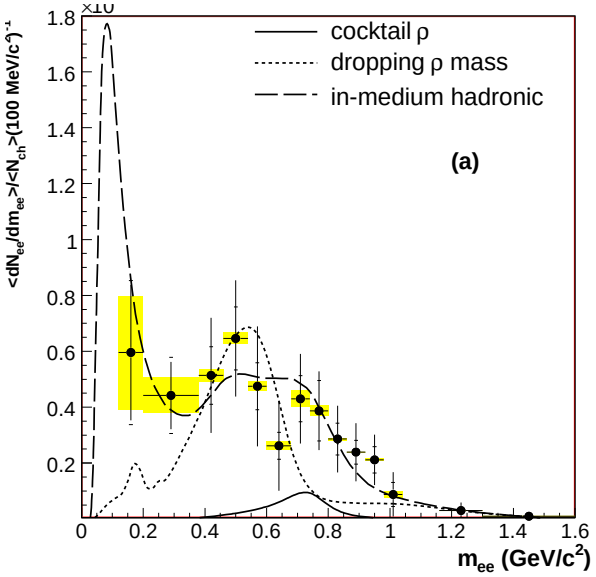

Figure 1.4: e^+e^- pair yield in Pb-Au collisions at 158 AGeV after substraction of the hadronic cocktail in comparison with theoretical calculations [27].

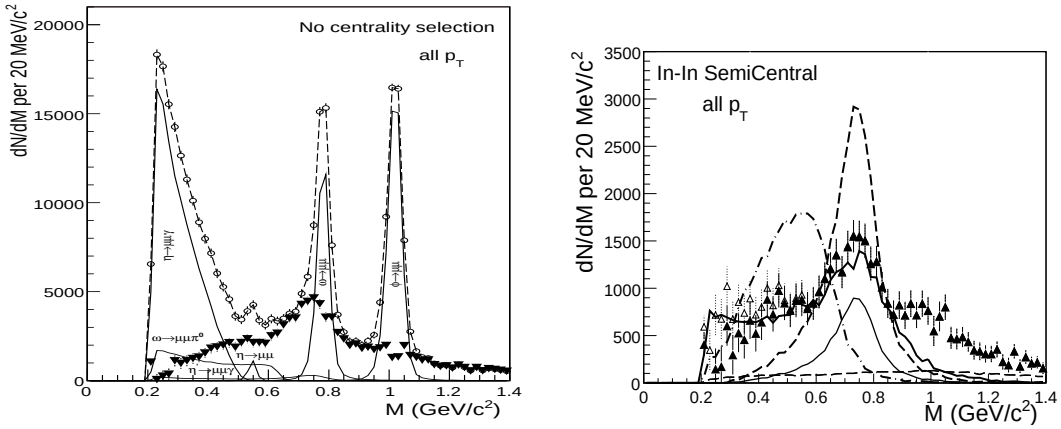

(a) Isolation of excess by substraction of experimental sources: total data (open symbols), expected sources (solid lines), difference data (thick triangles), sum of cocktail sources and difference data (dashed lines).

(b) Comparison of the excess mass spectrum for the semicentral bin to model predictions. Cocktail ρ (thin solid), unmodified ρ (dashed), in-medium broadening ρ [8, 31, 20] (thick solid), in-medium moving ρ [26, 12] (dashed dotted)

Figure 1.5: The excess mass spectrum for In+In at 158 AGeV.

In conclusion, the e^+ e^- and μ^+ μ^- data from the high energy experiments clearly favor models including a broadening scenario of the ρ spectral function in a hot and dense hadronic medium over a density-dependent ρ mass shift.

1.2.2 Low-energy dilepton spectroscopy

In the context of this work it is mandatory to discuss the low-energy dilepton spectroscopy done at the Bevelac.

The DLS experiment

The DLS experiment placed at the BEVALAC [34] was in operation in the late 80's and in early 90's. It was designed as a magnetic spectrometer combining of two identical arms which fanned out from the interaction zone on either side of the beam line. A schematic drawing of the spectrometer is shown in Fig. 1.6

DLS measured the dilepton invariant-mass spectra for p + p and p + d collisions with beam energies from 1.04 to 4.88 GeV, Ca + Ca at 1 and 2 GeV [35] and also systems such as C + C [36], d + Ca and He + Ca. This spectrometer had two significant drawbacks: a small acceptance and a low resolution in invariant mass (only $\sigma_{M_{ee}} \simeq 10\%$).

Up to the present day some of the DLS results remain unexplained by the theory. In the Ca+Ca data the discrepancy with theoretical calculations (HSD [37, 38]) leads to a factor of 7

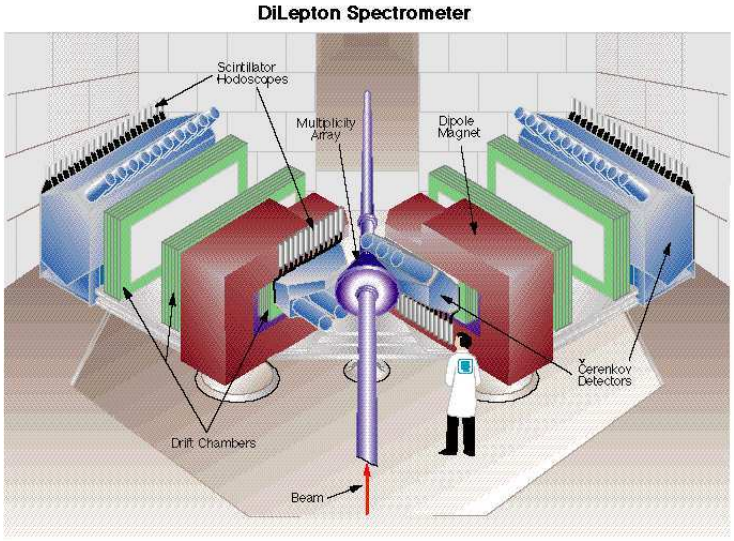

Figure 1.6: Schematic top view of DLS spectrometer.

larger yield than the predictions, especially in the intermediate mass region (200 - 600 MeV/c^2), as shown in Fig. 1.7.

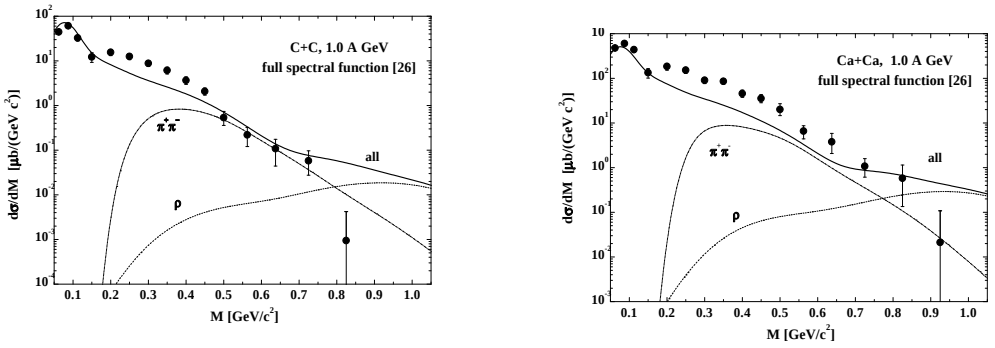

(a) (b)

Figure 1.7: The dilepton spectra for Ca+Ca and C+C at 1.04 AGeV calculated with free spectral function in extended approach of BUU calculations [37] in comparison with the data from DLS [36].

This discrepancy could be reduced to a factor 3 by more refined theoretical calculations

[39] in which the in-medium spectral function of the ρ meson was included.

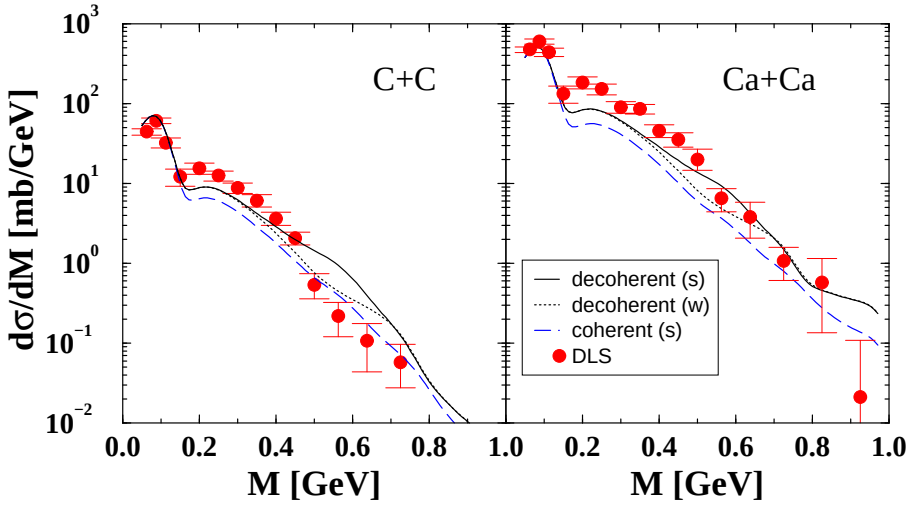

Figure 1.8: Comparison of the DLS data with the RQMD model [39].

Up to now, none of the models has found a consistent description of the dilepton enhancement observed by the DLS collaboration and the "DLS puzzle" is thus still unresolved.

The observed disagreement between theory and the DLS data was one of the incentives to built a new experiment, HADES, which can explore the dilepton signal in the same energy regime of nuclear collisions as DLS, but with a much better instrumental acceptance and resolution.

The E325 experiment

Dilepton production induced in nuclei in reaction with beams of photons and protons is very useful to investigate its behavior at low temperature and normal nuclear matter density. A few such measurements have been conducted during the last years by the CB-TAPS experiment at ELSA [40], the CLAS-G7 experiment at JLAB [41], and the E325 experiment at KEK [42]. Various changes in the reconstructed spectral shape of ρ, ω and ϕ mesons have indeed been reported. As an example the results from the E325 experiment are presented in the following.

The E325 experiment [43, 44, 42] has been performed at the KEK 12-GeV Proton Synchrotron to measure the invariant-mass spectra of ρ, ω and ϕ decaying into e^+ e^- pairs and ϕ decaying into K^+K^- simultaneously in p+A reactions [45].

A comparison has been done for the data with a model considering the in-medium mass modification. In this model, the mass of the vector mesons decreases linearly as a function of the density ρ following the Hatsuda, Lee parametrization [15, 46]:

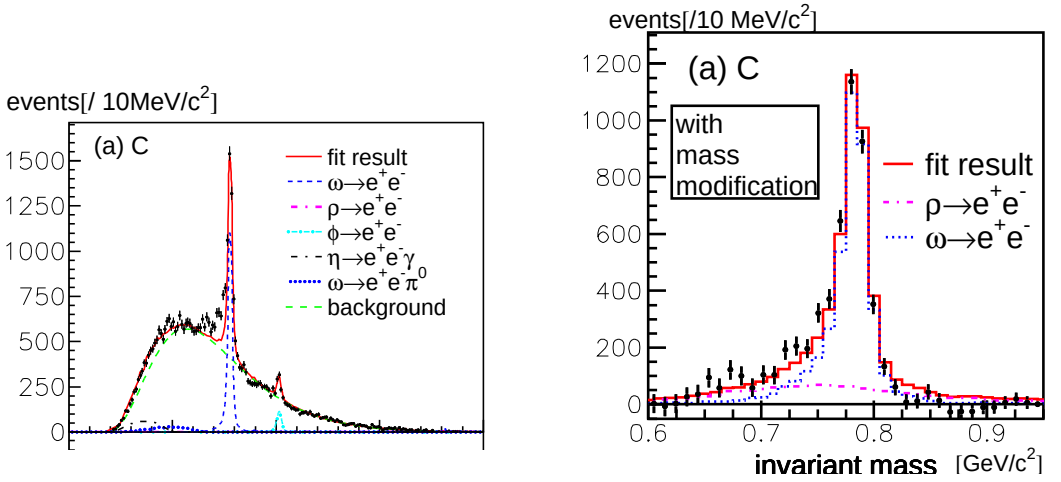

(a) Full spectra together with model cocktail.

(b) after background and η Dalitz and ω Dalitz components substraction.

Figure 1.9: Invariant mass spectra of e^+e^- pairs

$$\frac{m(\rho)}{m(0)} \simeq 1 - \kappa(\frac{\rho}{\rho(0)}) \tag{1.2}$$

where κ was expected to be 16 ± 6 % for ρ and ω mesons, $\rho(0)$ is the normal nuclear density. In the calculation it was assumed that the probabilities of ρ meson decays inside a nucleus are 46% and 61% for the C and Cu targets, respectively, while those of ω are 5% and 9%.

E325 claims a drop of the ρ meson mass by 9% and no in-medium broadening.

1.3 Overview of the present work

The results presented in this work are an important prerequisite for the investigation of in-medium vector meson properties in A-A collisions. The powerful experimental method of dielectron spectroscopy allows for the determination of in-medium vector-meson masses. The experimental method, spectrometer performance and analysis strategy are presented in this work. The thesis is devoted to the study of dilepton production in ^{12}C + ^{12}C collisions at 2 AGeV using the HADES spectrometer.

The thesis is organized as follows:

- The general physics background and the motivation for the HADES experiment was presented in this chapter.

- The second chapter describes the HADES spectrometer itself, the performance of the detectors, as well as a summary of the experimental runs already done.
- In the third and fourth chapters the analysis strategy is described in detail. The analysis is split into two steps. The third chapter deals with the single lepton analysis, and the fourth with the reconstruction of the pair spectra.
- In the last (fifth) chapter the status of the theoretical interpretation of the HADES data is presented.

Chapter 2

The HADES spectrometer

The *H*igh *A*cceptance *D*i-*E*lectron *S*pectrometer (HADES) [47], shown in Fig. 2.1 , is a second generation dilepton spectrometer which has been set up at the heavy ion synchrotron (SIS) at GSI Darmstadt to measure and reconstruct the decay products of elementary (pion and proton) and heavy ion induced reactions, with beam energies up to few AGeV.

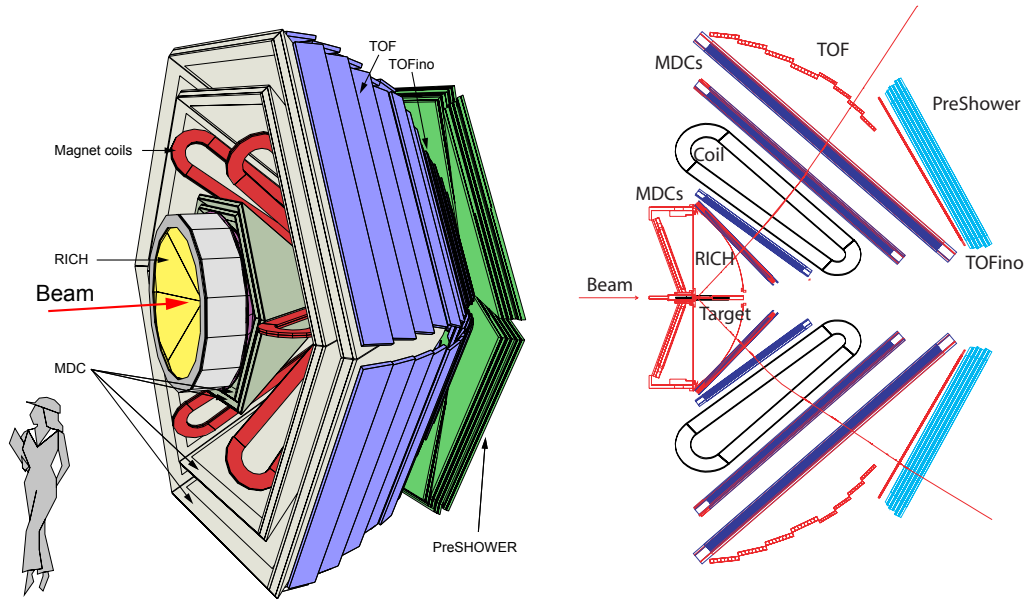

(a) An artistic 3D view

(b) Side view

Figure 2.1: The HADES spectrometer.

The main experimental goal of the HADES physics program is focused on in-medium properties of a light vector mesons, as well as on other important topics in hadron physics: validity of the VDM (Vector Dominance Model) hypothesis in the description of mesons and baryon Dalitz decays, electromagnetic form-factors of the nucleon in the time-like region and the study

of vector meson-nucleon coupling strengths. For these studies a systematic di-lepton spectroscopy in various reactions like: *pp*, *AA*, *pA*, π *p*, π *A* in 1-2 AGeV energy range has been selected. In the most challenging case of central Au+Au collisions at the maximum SIS energy (1.5 AGeV) the expected total yield of di-leptons from the vector meson decays is about 10^{-6} per event. In order to fulfill the task of hte experiment, several requirements need to be taken into account in the design of the detector and in the software development:

- large acceptance for the di-leptons,
- high rate capability, allowing operation at a beam intensity of up to 10^8 s^{-1},
- ability to cope with high particle multiplicities,
- highly selective trigger to enrich the event sample with lepton candidates,
- sufficient mass resolution to enable the recognition of structures with narrow width (light vector mesons),
- flat acceptance in invariant mass and transverse momentum in order to reduce systematic errors in the analysis,
- sufficient rejection of the hadronic and electromagnetic background.

These requirements are satisfied by a spectrometer that covers about 50 $\%$ of the total phase space with a good acceptance in the mid rapidity region for the products from nuclear reactions. The HADES spectrometer (see Fig. 2.1) is built out of 6 identical sectors, where each one covers 60 degrees of azimuthal angle and polar angle between 18° and 85°. The whole spectrometer is rotationally symmetric around the beam pipe.

The innermost detector of HADES is the hadron-blind **R**ing **I**mage **CH**erenkov detector (RICH). It is followed by a set of 4 MDCs (**M**ulti-wire **D**rift **C**hamber), two chambers placed in front of and the other two behind a magnetic field created by the coils of a super-conducting magnet. The six coils produce a toroidal magnetic field of radially (increasing polar angle) declining strength. The momentum of a particle produced in the collision is then deduced by reconstructing the particle trajectory with the help of the hits in the four MDC modules. At the outermost shell of the spectrometer the META detector (**M**ultiplicity and **E**lectron **T**rigger **A**rray) is located. It consists out of the TOF (**T**ime **O**f **F**light) detector covering polar angles from 45° to 85°, and TOFINO and Pre-SHOWER detectors covering polar angles up to 45°. The META measures the particles' velocity and provides information for particle identification. Two diamond detectors (START, VETO) are used for triggering of the events. The Pre-Shower detector provides additional information for the particle identification in a phase space region where the particle density is higher and the flight time obtained is not sufficiently precise to fully distinguish pions from electrons. In the following sections, all the individual, detector components are described in more detail with the emphasis on the electron/positron identification.

2.1 Start and veto detectors

The first detectors in the HADES spectrometer are the two diamond detectors [48, 49], placed 75 cm upstream (START) and 75 cm downstream (VETO) from the target (see Fig. 2.2). The main purpose of the START-VETO system is the delivery of the reference time stamp, which is used for the time-of-flight measurement between target and META detectors [50]. In addition the VETO detector is used to reject all particles which do not react with the target. The important advantages of the diamond material in this application are:

- high rate capability,
- radiation hardness,
- fast signal collection time,
- low noise.

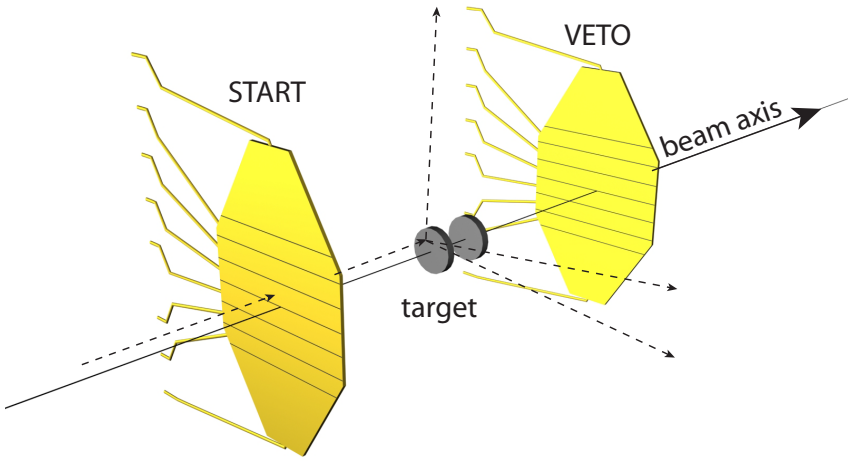

Figure 2.2: Start and Veto detectors

Both detectors have identical design and each has 8 stripes of variable width ranging from 5.4 mm for the most outer strips to 1.55 mm for the inner strips. The width are optimized such that a coincidence of one START strip with one of the 3 inner VETO strips is sufficient for a veto efficiency of 96 %. The detector thickness of 100μm is chosen to minimize multiple scattering and secondary reactions.

2.2 The Ring Imaging Cherenkov Detector

The RICH detector [51, 52], see Fig. 2.3, has been designed to identify electron/positron with momenta in the range 0.1 GeV/c < p < 1.5 GeV/c.

The RICH is surrounding the target in the forward hemisphere, covering the full azimuthal range and a polar range between 18 and 85 degrees. Very selective electron identification is done using the Cherenkov effect [54]. A Cherenkov detector is able to identify and select particles on the basis of their velocity. Electrons with energies in the MeV range move almost at the speed of light in vacuum ($\beta \cong 1$). When a particle traversing a medium at a velocity faster than the speed of light in the medium: $v > v_{th} = c/n$, where n is the refraction index of the traversed medium, then Cherenkov light is emitted at an constant opening angle of θ_c with respect to the particle trajectory. This angle is given by the following formula:

$$cos\theta_c = \frac{1}{n\beta} \tag{2.1}$$

$$\beta = \sqrt{1 - \frac{1}{\gamma^2}} \tag{2.2}$$

where β is the velocity of the particle in units of the speed of light and γ is the relativistic factor. For each material there is a minimum velocity ($\beta > \beta_{th} = 1/n$) that the particle must exceed to produce Cherenkov photons. Therefore, by choosing a material with the proper refraction index n the detector can be operated such that it is blind to specific particles. One of the most important components of Cherenkov detectors is the radiator gas, where the Cherenkov light is generated by particles traversing it. The radiator gas in the HADES RICH detector is chosen to be C_4F_{10}, which has a refraction index of n = 1.00151 corresponding to a threshold

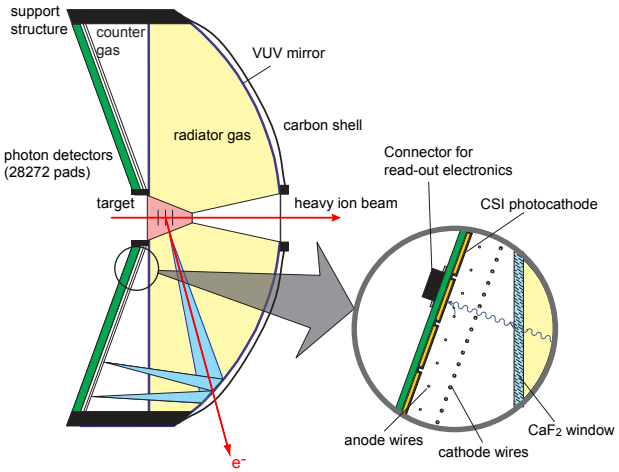

Figure 2.3: Schematic cross-section of the RICH detector [53]

for Cherenkov effect of γ = 22. Therefore, only particles with velocity β > 0.9985 produce Cherenkov light, guaranteing the hadron blindness of the detector. All protons and most of the pions produced at SIS energies have momenta significantly below the radiator threshold:

- protons: $p_{th} \simeq$ 17.1 GeV/c
- pions: $p_{th} \simeq$ 2.5 GeV/c
- electrons: $p_{th} \simeq$ 9.3 MeV/c

The number of emitted photons for each particle depends on the path length of the particle in the gas radiator. In the RICH detector this length varies from 38 to 68 cm depending on the track polar angle. On average, a lepton with a momentum of 100 MeV/c produces about 110 photons in the radiator. In addition, the gas is transparent down to wavelengths λ = 145 nm and does not show any significant scintillation from charged particles.

The photon-detector has to provide a sufficient position resolution and multi hit capability to allow for unambiguous ring identification. Furthermore, it has to match the following requirement: minimum sensitivity volume for charged particles, very fast charge collection and short recovery time. The detection for single photo-electrons is ϵ > 95 $\%$.

2.3 The MDC Detectors

The essential spectroscopic information delivered by the HADES spectrometer is the invariant mass of di-leptonic pairs, defined as the modulus of the four-momentum sum of the lepton pair. The Multi-wire Drift Chambers (MDC) [55, 56, 57] are used for the tracking of the particles and the determination of the momentum from the deflection in the magnetic field.

The HADES tracking system [55] has been optimized for a very good electron momentum resolution. In order to resolve the various vector mesons, a di-lepton invariant mass resolution of the order of the natural ω width $\delta M/M$ = 1$\%$ is required which corresponds to a momentum resolution $\delta p/p \leq$ 1.5 $\%$.

The tracking system consists of 4 MDC planes (MDC I-IV), two in front of and two behind the magnetic field in order to determine the direction of the particles before and after the deflection. The geometry allows an independent reconstruction of straight track segments before and after the field. This property is advantageous for the following reasons:

- the reconstruction of the kick angle is not affected by multiple scattering between the target and the first tracking detector,
- the reconstruction of close hits is very much improved thus allowing a better rejection of track pairs originating from external conversion processes.

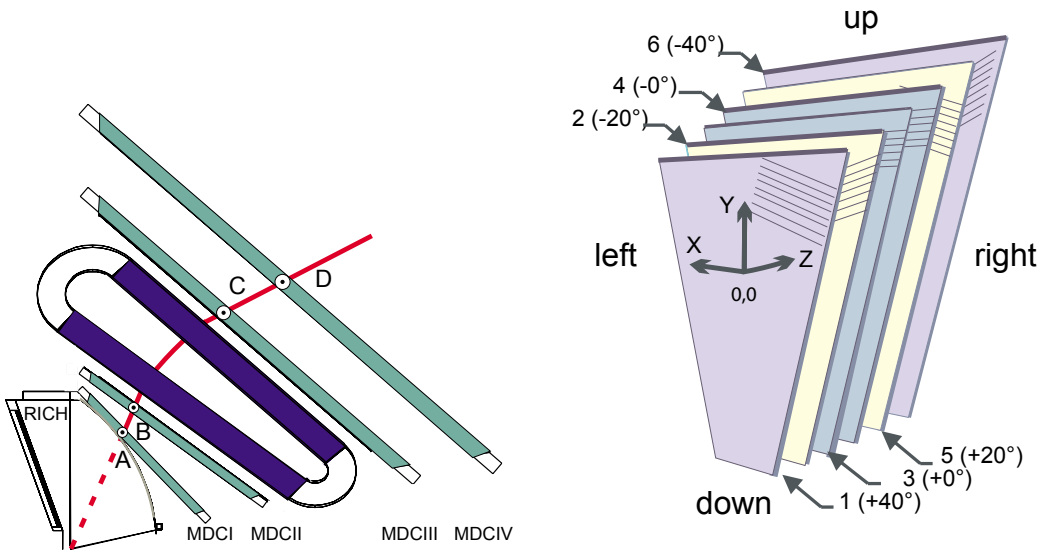

(a) arrangement of the MDC chamber with respect to the magnetic coils

(b) view of the six anode wire frames inside a HADES drift chamber

Figure 2.4: Schematic layout of the HADES tracking system

Each tracking plane is composed of six trapezoidal chambers, covering 60^o of the azimuthal angle each. All 6 chambers together cover the full acceptance in the azimuth and polar angles range from 18^o to 85^o. To cope with ambiguities in track reconstruction in a high multiplicity environment of a heavy ion reaction all chambers are composed of six sense/field wire layers oriented in five different stereo angles, i.e. $\pm\ 0^o$, $\pm\ 20^o$, $\pm\ 40^o$, as seen on Fig. 2.4. This layout is optimized with respect to resolution in the direction of the momentum kick θ, minimization of double hits, and resolving power with respect to track ambiguities.

2.4 The Superconducting Magnet

A high magnetic field is created in such a way that the momentum of the deflected particles can be obtained with high resolution (dp/p = 1 % - 1.5 %). On the other hand, lepton identification with the RICH detector requires a nearly field free region around the target. Furthermore, a large momentum range of p = 100 - 1500 MeV/c must be accepted simultaneously within a large solid angle. The HADES magnet (ILSE) [58] , shown in Fig. 2.5 consists out of 6 super-conducting coils surrounding the beam axis and produces a toroidal field which bends the particles in first approximation only in the polar direction.

The maximum field of 3.7 T is obtained at the coil surface inside the forward arc. The field strength reache about 0.7 T in the HADES acceptance (in the middle of the sector), resulting in a momentum kick of the order of 50 MeV/c, and higher (100 MeV/c) at smaller polar angles. In

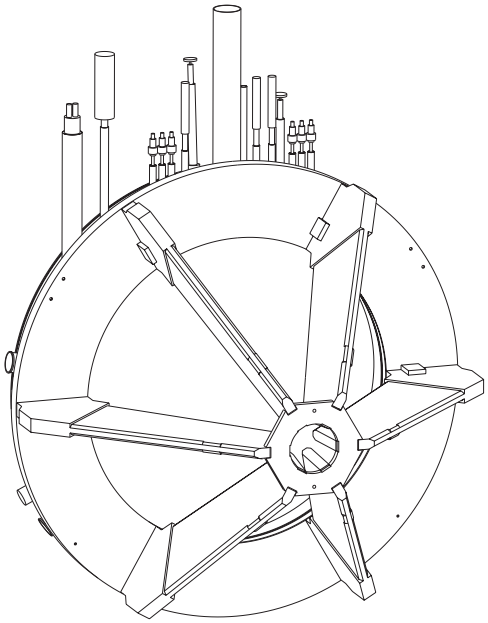

Figure 2.5: ILSE magnet

this way, a good momentum resolution can be achieved without losing low-momenta particles [58].

2.5 The multiplicity electron trigger array detectors

The **M**ultiplicity **E**lectron **T**rigger **A**rray (META) is positioned behind the tracking system and is the outermost detector system of the HADES spectrometer. It consists of two **T**ime **O**f **F**light detectors (TOF and TOFINO) and a Pre-SHOWER detector covering forward polar angles (18° - 45°). The META detectors provide a fast determination of the charged particle multiplicity in each event in order to select events by the centrality of the collision. Furthermore, it measures the time-of-flight of each detected particle in order to provide particle identification by means of the momentum associated to a track and also to separate electrons and positrons from hadrons.

2.5.1 The TOF Detector

The TOF detector [59, 60] provides the particle identification by measuring the time between the start detector and the particle arrival signals and therefore, assuming a given path length, measuring the velocity of the particle.

The TOF covers polar angles from 44° to 88°. The TOF wall is made of 6 sectors, each consist of 64 rods. In total, TOF consists of 384 scintillator rods connected on both sides to photomultipliers. The length and the width of the rods increase with larger polar angles such that the cross-section varies from 20 × 20 mm^2 for the innermost 192 rods to 30 × 30 mm^2 for the outermost rods resulting in a finer granularity in the more forward angular region.

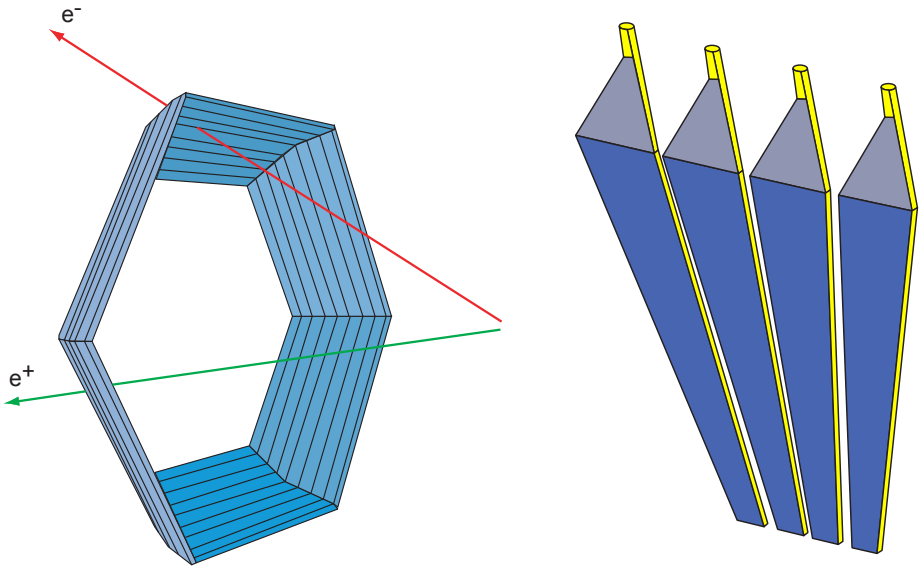

(a) TOF detector (b) TOFINO detector (one sector)

Figure 2.6: A schematic view of the META detectors

From the measured signals (t_{left} and t_{right}) the following information can be extracted: the time-of-flight (t_{TOF}) of particles, the hit position on the rod (x), and the energy deposited in the rod by the passing particle (ΔE). These relations can be represented by the following formulas:

$$t_{TOF} = \frac{1}{2}(t_{right} + t_{left} - \frac{L}{v_{group}}) \tag{2.3}$$

$$x = \frac{1}{2}(t_{right} - t_{left})v_{group} \tag{2.4}$$

$$\Delta E = k\sqrt{A_{left}A_{right}}e^{L/\lambda_{at}} \tag{2.5}$$

where t_{right}, t_{left} is the time measured on the left and the right side of the rod corresponding to the time between the reaction and the readout of the signal, v_{group} is the group velocity in the rod (average velocity of light in the rod), L is the length of the rod, A_{left} and A_{right} are the signal amplitudes at the left and the right ends of the rod, λ_{at} represents the light attenuation length of the rod and k is a constant. The time resolution for the C+C at 2 AGeV of about 150 ps is achieved by the TOF. This corresponds to a resolution in hit position of 2.5 cm.

2.5.2 The TOFINO detector

The region between 18° and 44° of polar angle is covered by another time-of-flight detector: TOFINO [61]. It consists of 24 scintillator paddles (6 sectors $\times$ 4 modules).

The signal is read out only from one end of the paddle. The typical time resolution of the TOFINO detector is about 420 ps for C+C at 2 AGeV, dominated mainly by the geometrical factor of light collection.

The time-of-flight of a crossing particle is calculated according to the formula:

$$tof = t - \frac{x}{V_g} \tag{2.6}$$

where t represents the time interval between the reaction and the arrival of the light pulse at the PMT, V_g the light group velocity in the pad and x the distance from the particle hit position in the cell to the PMT.

The reduced granularity increases the probability of multiple hit in the same TOFINO pad, which makes problematic tof extraction in these events.

The replacement of the TOFINO detector by a timing Resistive Plate Chamber (tRPC) [62, 63] wall with roughly 100 times more channels and time resolution well below 100 ps is foreseen in the near future.

2.5.3 The Pre-Shower Detector

At forward angles the separation of electrons from hadrons by means of a time-of-flight measurement is more difficult than at large angles due to the higher hadron momenta and larger hit densities. For the time resolution that is achieved by the TOFINO detector the number of fake electrons is about 10 times larger than in the TOF wall. To provide additional lepton identification for polar angles of less than 45° the Pre-Shower detector [64, 65] has been added to the HADES setup. It is located directly behind the scintillator paddles and provides precise position measurement essential for the flight time propagation corrections. Figure 2.7 shows the schematic view of the Pre-Shower detector and also the way how it is joined together with the TOFINO detector. The Pre-Shower detector [66] is composed of two lead converters placed between three wire chambers (pre-chamber, post1-chamber, post2-chamber).

The idea of the e^+, e^- identification via electromagnetic shower measurement is presented in Fig. 2.7 (left). The discrimination of leptons from hadrons is done by comparing the integrated charge on the pads before and after the lead converters; the electrons and positrons passing the detector induce much higher charges in the second and the third chamber than in the first one, because of the electromagnetic shower produced in the lead converters [67].

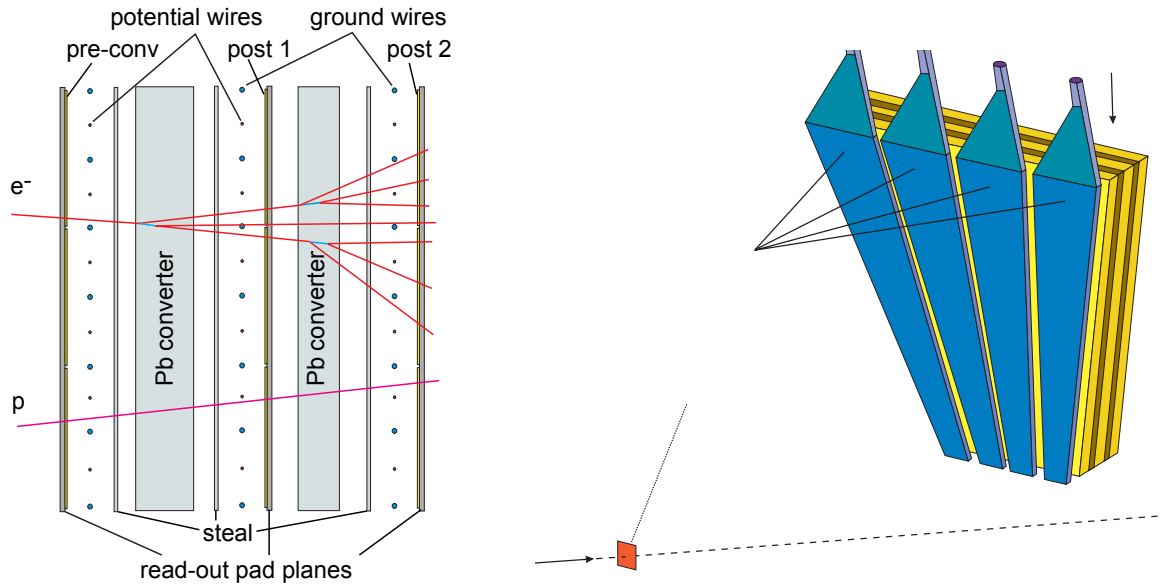

(a) side view of the Pre-Shower detector (b) schematic layout of the Pre-Shower and forward TOF

Figure 2.7: Schematic view of the Pre-Shower detector (one sector)

2.6 Trigger System

The branching ratio for the direct decay of the ρ, ω or ϕ mesons into e^+e^- pairs is very small ($4.4 \cdot 10^{-5}$, $7.2 \cdot 10^{-5}$ and $3.1 \cdot 10^{-4}$ respectively). The main task of the trigger system is to do on-line selection of the events which have dilepton tracks. There are two levels of the trigger which contribute to the event selection.

2.6.1 First level trigger

The data acquisition is started by the positive first level trigger (LVL1) decision. The signal from the photomultipliers of the TOF and TOFINO detectors is read out by the trigger module. The decision of the LVL1 trigger is made in very short time t < 100 ns based on the analysis of the multiplicities in the META detectors. The trigger which is used for the LVL1 decision can be written in very simple way:

$$(M_{TOF} + 2 * M_{TOFINO})/2 > M_{Thr} \tag{2.7}$$

where M_{TOF} and M_{TOFINO} are the signal multiplicities (number of fired photomultipliers) in the TOF and TOFINO detectors. In the November 2002 run the threshold for the first level trigger was set to 4. Multiplicity defined in this way is not strictly connected to the charged particle multiplicity in the acceptance since in some cases single particle can produce light in two neighboring rods/padels.

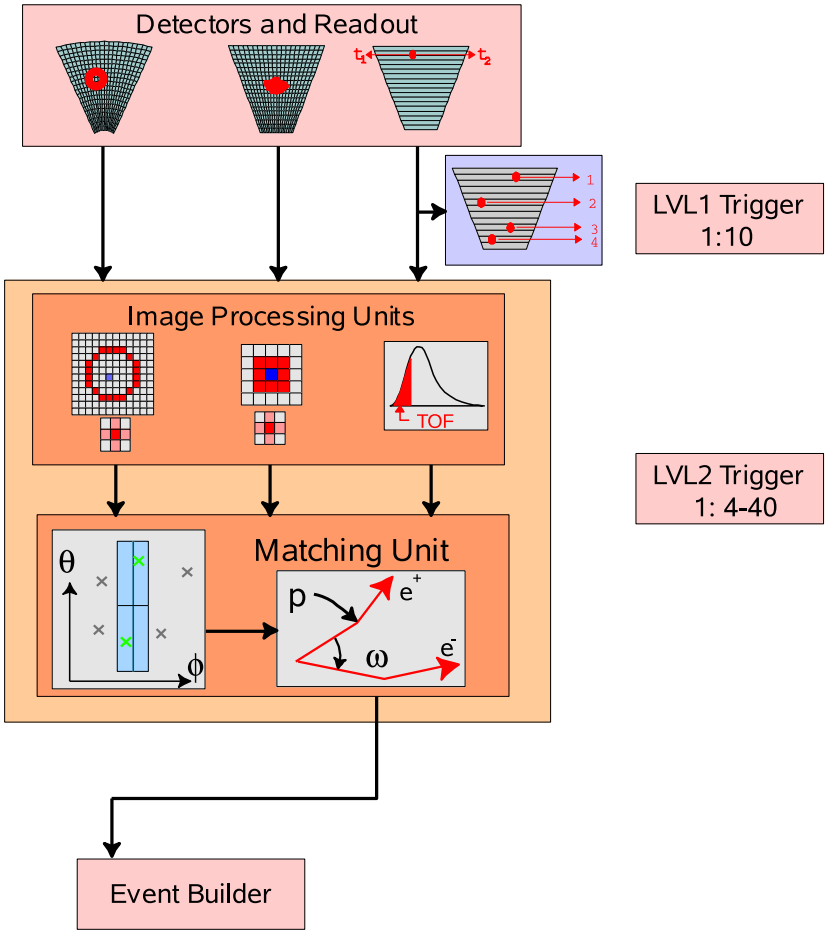

Figure 2.8: Schematic view of the HADES multi-level trigger system

2.6.2 Second level trigger

To reduce the amount of events, the second-level trigger (**LVL2**) has been introduced, based on online electron pattern recognition. The main task of the LVL2 is to perform fast ($t < 10\mu s$) real-time dilepton identification and to limit the amount of data written on the tape to events only with electron candidates.

Di-electron identification performed by the LVL2 trigger [68, 69, 70] is made in two steps (see Fig. 2.8):

- searching for the lepton candidates in the corresponding detectors (RICH and META). For each of these signatures position information is provided.
- angular correlation of the lepton candidates before and after magnetic field with the Matching Unit (MU),

The downscaling box purpose is to select and scale down events in a statistical fashion, regardless of whether they contain lepton pair or not, for hadronic analysis and normalization factor (downscaled events). It is possible to program via software a **downscaling** factor, which tells the downscaling box the number of events to be discarded between two accepted events.

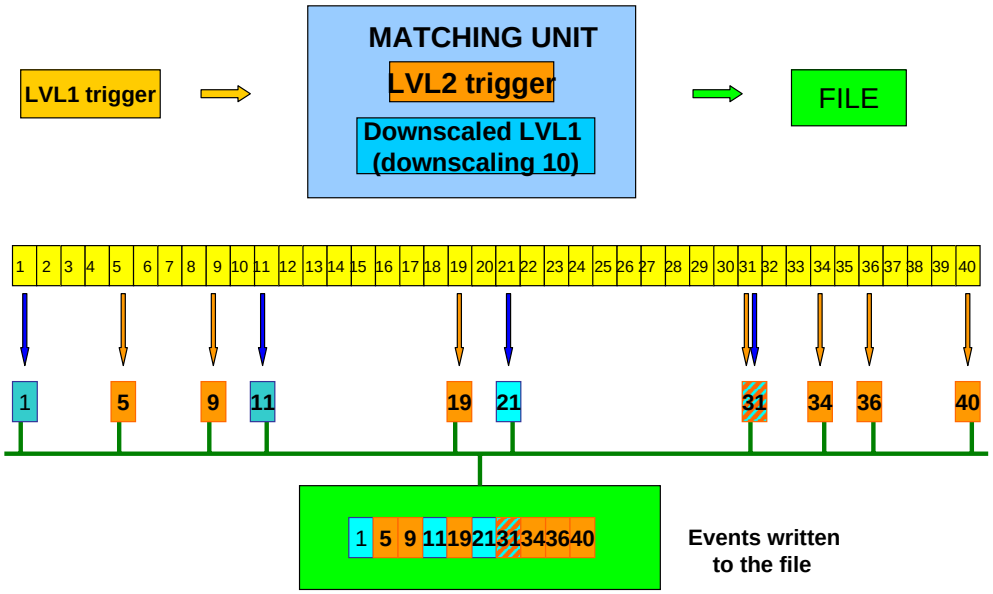

Figure 2.9: Schematic view of the events selection used for the data acquisition

As an example we can take the scheme shown in Fig.2.9, which represents a scheme of the event selection used for data acquisition. A first selection of events is done by the 1^{st} level trigger (yellow boxes), and they are sent to the matching unit, where downscaling factor is set to 4. This means that one event out of ten is stored (1, 11, 21, 31), regarding the 2^{nd} level trigger decision. It is tagged as downscaled and the related downscaling factor is recorded, as well. All the events with a recognized lepton pair are stored as well, and tagged as LVL2 events. This means that an event can be at the same time downscaled (LVL1), as well as having a positive 2^{nd} level trigger decision (LVL2), like for instance the event number 30 in the example. To have a total number of LVL1 events, one need to multiply the number of downscaled events (4) by the downscaling factor (10). In our sample one obtain 41 trigger events, against 10 which are effectively stored to file.

This trigger system currently enables a data reduction by a factor of 10 for the data presented in the thesis. A detailed description of the trigger concept and development can be found in [69, 68, 70, 71, 72]. The LVL2 trigger has an efficiency below 100%, therefore, for evaluating the number of dilepton events in the data sample this correction has to be taken into account (for details see. Appendix D).

2.7 Characteristics of the data set - NOVEMBER 2002

In November 2002 HADES had a commissioning beam time with ^{12}C + ^{12}C at 2 AGeV. A segmented carbon target, consisting of two discs with a diameter of 3 mm and a length of 3 mm, a density of 2.15 g/cm^3 and a spacing of 2 cm was used. Data were taken with a magnet current of I = 2497 A, corresponding to 72 % of the maximum strength of the magnetic field.

The detector setup consisted of the START, RICH and the META detectors which have been fully completed. The MDC tracking system consisted of 18 MDCs chambers: plane I and II were completed and fully operational; in addition, 4 chambers of plane III and 2 chambers of plane IV were installed, as shown in Fig. 2.10. The tracking characterization will be presented in chapter 3.

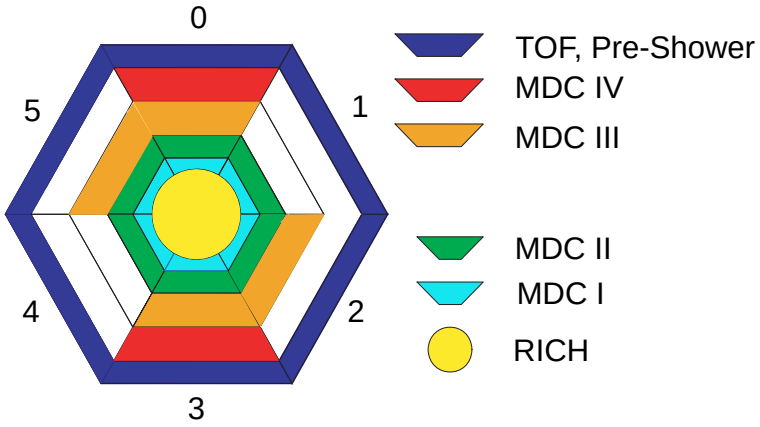

Figure 2.10: Schematic view of the sub-detectors in experiment in NOV02.

The data acquisition was performed by using different 1^{st} level trigger (LVL1) conditions (defined by TOF and TOFINO multiplicities):

- $M_{LVL1} > 2$, about 15 % of the total events
- $M_{LVL1} > 4$, about 85 % of the total events

The LVL1 condition has an influence on the centrality of the reaction. This has been investigated in the Monte Carlo simulations based on events obtained with the UrQMD[1] transport code [73]. Figure 2.11 shows the impact parameter distribution, corresponding to the following scenarios:

- blue: geometrical cross section,

[1] **U**ltra **r**elativistic **Q**uantum **M**olecular **D**ynamics

- red: only events with nuclear interactions (reaction cross section),
- green: events with reaction which pass the LVL1 trigger condition (M $\geq$ 4) (trigger cross section).

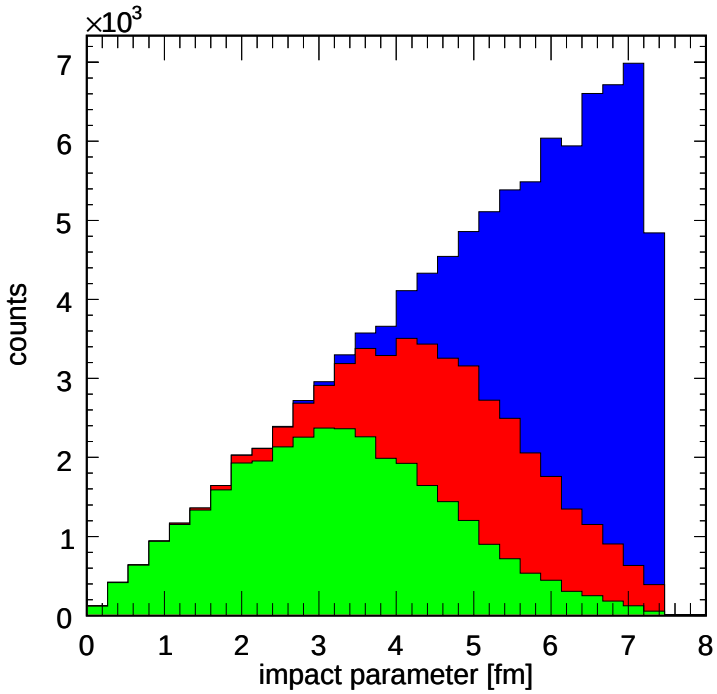

Figure 2.11: Distribution of the impact parameter of C+C@2AGeV in UrQMD.

The geometrical cross section is:

$$\sigma_{geom} = \int_0^{r_0} bdb = \pi r_0^2 \tag{2.8}$$

The reaction cross section is:

$$\sigma_{reac} = \int_0^{r_0} (1 - T(b))bdb = 947mb \tag{2.9}$$

The total trigger reaction cross section is:

$$\sigma_{reac} = \int_0^{r_0} (1 - T1(b))bdb = 570mb \tag{2.10}$$

where T(b) and T1(b) is the transparency function.

Calculating the ration between the total reaction cross section and trigger reaction cross section $\frac{\sigma_{reac}}{\sigma_{LVL1reac}}$ one get 60% reduction of the total reaction cross section by LVL1 trigger decision.

Fig. 2.12 shows the number of collected events during the beam time as a function of the day. Four days of break during experiment (2^{nd} of December - 5^{th} of December) were due atreatment run.

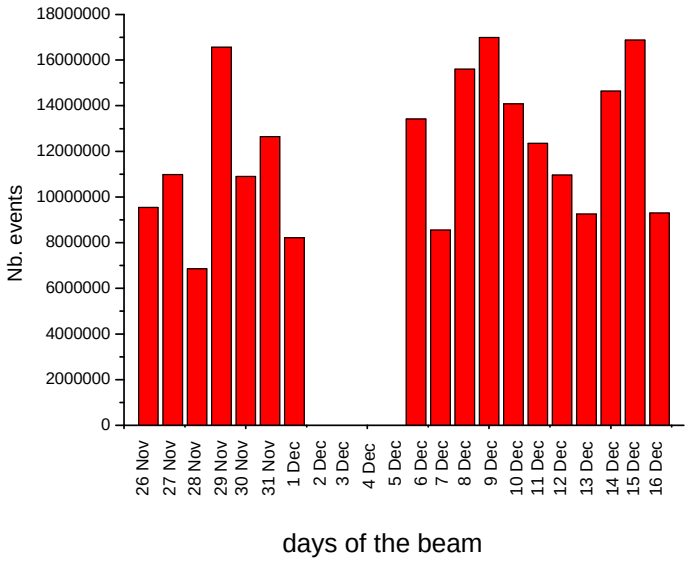

Figure 2.12: Statistics collected during each day of the experiment.

An overall number of $2.13 \cdot 10^6$ events have been stored on tape, corresponding to $2.13 \cdot 10^7$ LVL1 triggered events. Approximately 56% (i.e. about 120 M) of the statistics are downscaled LVL1 events and 44 % (i.e about 93 M) of LVL2 events. Around 8 % of LVL1 events have a positive second level trigger decision.

Before the full analysis has been performed, the quality has been assessed by each detector group for all files. Some of the files have been discarded from the analysis due to various problems with the detector performance. Statistics which has been taken for the analysis corresponds to total of $6.5 \cdot 10^8$ LVL1 (multiplicity 4) events from 28^{th} of November until 16^{th} of December 2002.

Chapter 3

Single lepton analysis

3.1 Introduction

The analysis of the $November\ 2002$ data set will be described in the present and next chapters. As it was described in the technical part of this thesis, the HADES spectrometer covered 6 sectors, except for MDC plane 3 and 4, complete with all detectors. It is important to mention that the present data analysis was performed with so-called **low resolution** tracking method. This means that for the momentum determination only the 2 inner MDC planes were taken into account.

The final analysis was done in 2 steps:

- lepton analysis: selection of single lepton tracks,
- dilepton analysis: pre-selected tracks were combined into like-sign and unlike-sign pairs and an additional rejection strategy was applied.

In the present chapter the reconstruction of the single lepton tracks is presented. A set of cuts was applied to reconstruct tracks which correspond to a true lepton. The lepton identification consisted of the following steps:

- spatial correlation between RICH rings and track segments reconstructed in the inner MDC planes, momentum dependent,
- application of minimum bias ring conditions,
- application of a momentum dependent condition on velocity β using the TOF and TOFINO detectors,
- application of a electromagnetic shower condition in the PreShower detector.

The schematic analysis flow is shown in Fig. 3.1.

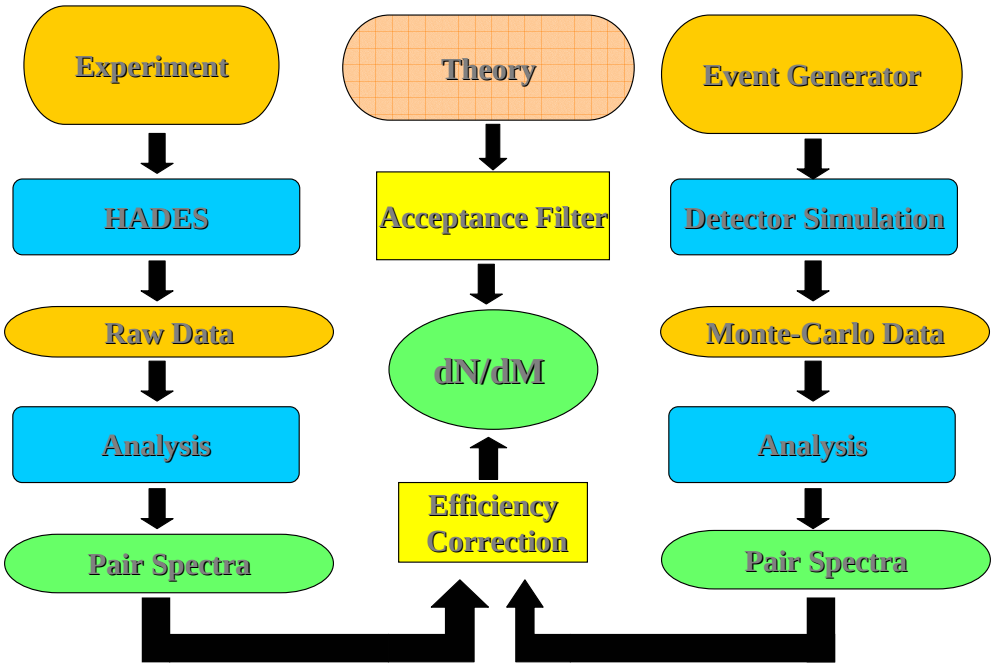

Figure 3.1: Schematic view of the analysis flow.

The HADES online/offline analysis is realized within the HYDRA [74] (**H**ades s**Y**stem for **D**ata **R**eduction and **A**nalysis) framework, based entirely on ROOT C++ classes [75]. This approach allows full and consistent use of all built in features of the ROOT software package developed and maintained at CERN. The object-oriented design of HYDRA is modular, e.g. detector specific, and/or task-specific classes are all derived from a common set of base classes, and therefore it is very flexible and extendable.

The HGEANT [76] is a simulation package for HADES written in FORTRAN and built upon the GEANT [77] program from CERN. The purpose of HGEANT is to simulate the detector response of the HADES spectrometer to the passage of charged particles. This means HGEANT is not used for simulating the heavy ion collision. For this purpose, external programs, called event generators, are used. The event generator output is a file with the description of all particles in the final state of the collision. HGEANT reads that information and tracks the particles through the spectrometer.

The PLUTO event generator [78, 79] was developed to simulate e^+e^- pairs from conventional sources, which consist of the known hadron decays in proton-proton, proton-nucleon and nucleon-nucleon collisions.

The simulated data are produced under conditions that are close to the real measurement. As one can see in the flow diagram the same kind of analysis are performed on the real data (left column), as well as on simulated data (high column). Simulated data holds more information than a real one. One of the important advantage of simulation is access to the original information about parameters of all particles in system during the analysis. This feature allows to compare the reconstructed parameters of particles with the true ones.

3.2 Low-resolution momentum reconstruction

Different methods for the momentum reconstruction have been developed. Each of the methods reflects the proper hardware installation and the different needs of the analysis in different detector configurations. The results presented here are based on the 'kick-plane' method. The momentum of the particle is obtained from its deflection in the magnetic field, which requires measuring the particle's direction before and after the field. This information is provided by the inner MDC chambers before the magnetic field and the META detectors after the magnetic field.

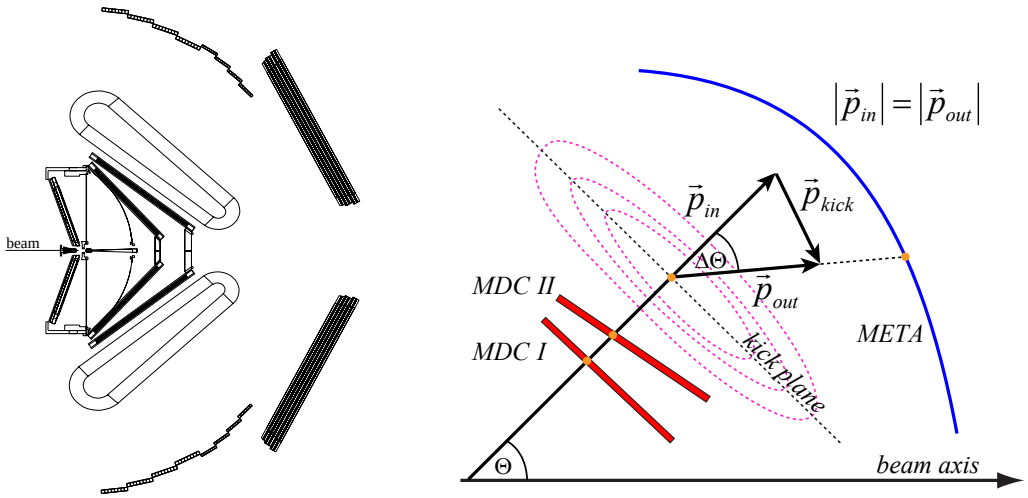

(a) HADES setup in NOVEMBER 2002

(b) Schematic of the *kick plane* algorithm

Figure 3.2: Left: Low resolution setup of the HADES spectrometer (with no outer MDC chambers shown). Right: *Kick plane* approach (schematically shown).

The deflection of a particle in a magnetic field is proportional, both, to the field strength and to the distance traveled by the particle in the field. This allows to replace the original field by an other, which is compressed in space, but at the same time increased in strength. In other words, the field is defined as a 2D plane, where all the deflection takes place. This can be parameterized in the first order approximation in the following way:

$$p = \frac{p_T}{2\sin(\Delta\theta/2)} \tag{3.1}$$

where p_T is the transverse momentum (momentum kick) and $\Delta\theta$ is the deflection angle, as it is shown schematically in Fig. 3.2 (b).

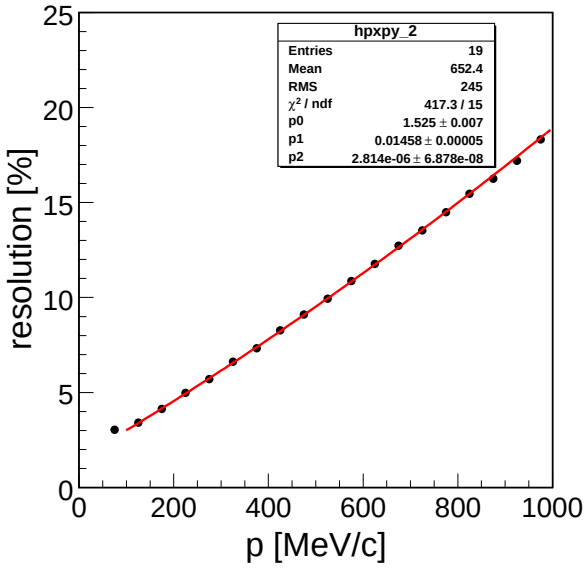

Figure 3.3: Momentum resolution ($\frac{1}{p}$ - $\frac{1}{p_{geant}}$) / $\frac{1}{p_{geant}}$ as a function of reconstructed momentum (p) of the kick plane algorithm.

The momentum resolution achieved with the kick-plane method (including higher-order corrections) is presented in Fig. 3.3 (a) as a function of the reconstructed momentum. In the momentum range of 0.1 GeV/c to 1 GeV/c the resolution varies between 7% - 20%. In front of the magnetic field the track is relatively well known, since the MDC chambers provide high accuracy not only in the direction, but also in the position of the track. The main limitation for the resolution is the relatively poor position resolution of the META detectors (for TOF $\sim$ 1 - 2.3 cm, PreShower $\sim$ 1.3 cm). However one should remember that these detectors have not been designed to provide an excellent resolution in position.

Before the momentum of the track is calculated, the matching of the hits in the META and the inner MDC detectors should be done. The particle track is uniquely defined by 6 parameters (four describing the inner MDC segment and two describing the track intersection with the META detector). The measurement of the track's x-coordinate on the META (x_m) has been chosen as the redundant variable used in the matching. One can then define the variable xPull as [80]:

$$xPull = \frac{x_c - x_m}{\sigma_{x_c - x_m}} \tag{3.2}$$

where x_m and x_c are the measured and calculated x-coordinates of the META hit, respectively. In first approximation one can assume, that

$$\sigma_{x_c - x_m} = \sqrt{\sigma^2(x_c) + \sigma^2(x_m)} \tag{3.3}$$

where σ_{x_m} and σ_{x_c} are an uncertainties in measurement and calculation, respectively. Figure 3.3 (a) shows a typical distribution of the xPull variable for good and fake tracks.

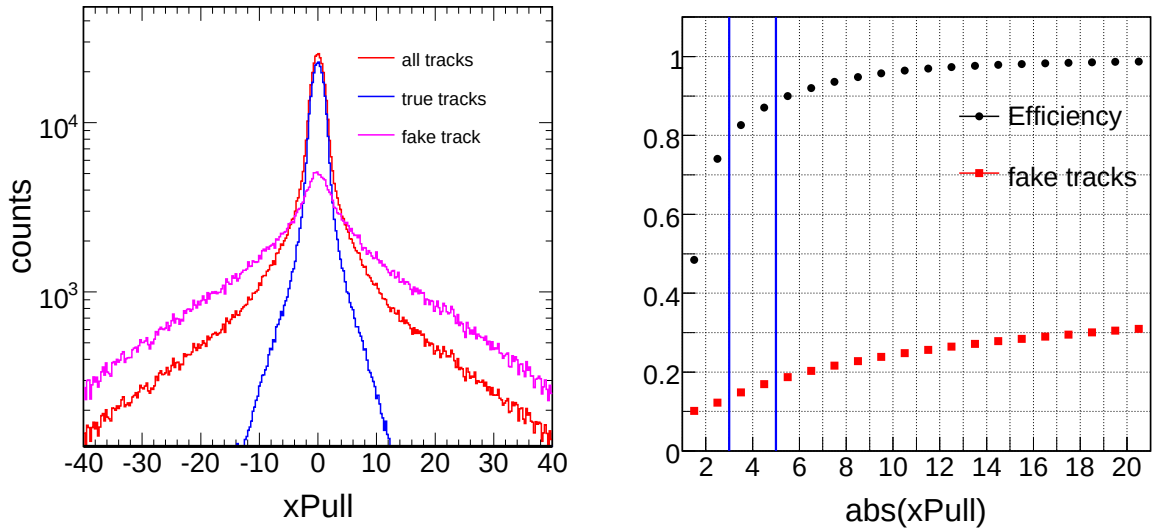

(a) Detail of the xPull distributions for good and fake tracks

(b) Efficiency and fake track contamination ias function of xPull.

Figure 3.4: xPull distribution of the kick-plane algorithm.

In order to discriminate good and bad combinations of the tracks one can just place a cut on xPull. Fig. 3.4 shows the efficiency and fake-track contamination as a function of the cut value. As it was described in [80], using Monte Carlo information the cut on xPull has been done in 2 steps with values of 3 and 5 (horizontal lines). The amount of fake tracks is thus reduced to 15 % and the efficiency is 95 %.

3.3 Identification of the single lepton tracks in RICH detector

Several independent ring image recognition algorithms have been developed. The algorithm based on the **H**ough **T**ransformation (HT) [81] is schematically shown in Fig. 3.5, This is a mathematical transformation of the space of pad combinations on the pad plane into space of the points (centers of the rings). Each combination of three fired pads is associated with ring of known diameter and its centrum. The center of a real Cherenkov ring is found as a local maximum in a virtual plane containing pads with ring centers for all these triplets. The pads from the true rings will be transformed to the points that lie close to each other. The height of this maximum corresponds to the **H**ough **T**ransform **Q**uality.

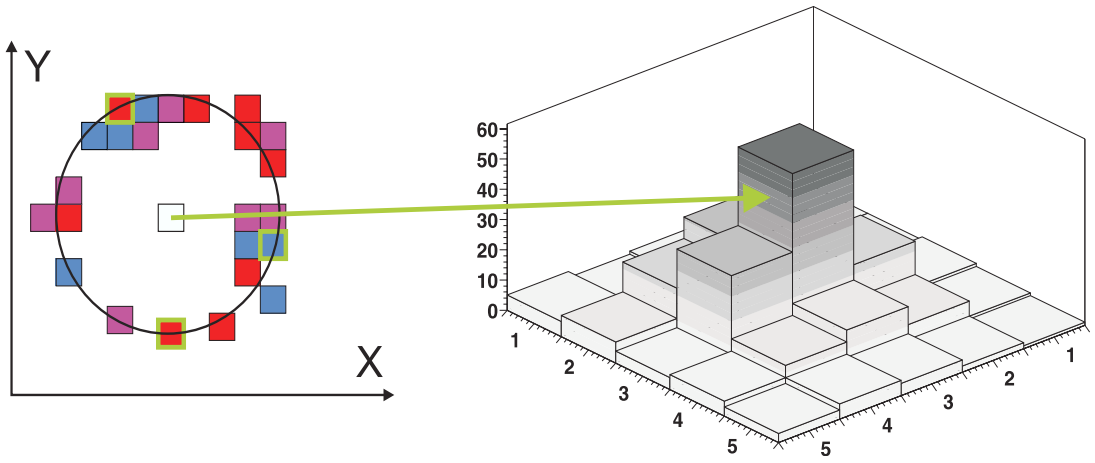

Figure 3.5: Schematic of the hough transformation method for the ring finding [53, 82].

A different approach is used in the **P**attern **M**atrix algorithm which is based on the superposition of a pattern image of a ring on the pad-plane. Fig. 3.6 shows a 11×11 pads pattern matrix. Each cell contains a weight reflecting the ring image. Positive values form a ring, while negative values correspond to those places where no fired pad is expected. The three-dimensional view of the matrix is shown in Fig. 3.6. The pad plane is scanned with the mask and for each pad the measured charged is multiplied with weight on the mask.

For each fired pad the corresponding weight on the matrix is added to produce a quantity defined as Pattern Matrix Quality (PM quality). This parameter is used as selection criterium. If PM is larger then a given threshold value a ring is found. True rings have larger values of PM, than the fake ones.

-46	-40	-25	1	22	27	22	1	-25	-40	-46
-40	-15	27	50	47	41	47	50	27	-15	-40
-25	27	44	12	-9	-15	-9	12	44	27	-25
1	50	12	-24	-33	-35	-33	-24	12	50	1
22	47	-9	-33	-36	-36	-36	-33	-9	47	22
27	41	-15	-35	-36	-36	-36	-35	-15	41	27
22	47	-9	-33	-36	-36	-36	-33	-9	47	22
1	50	12	-24	-33	-35	-33	-24	12	50	1
-25	27	44	12	-9	-15	-9	12	44	27	-25
-40	-15	27	50	47	41	47	50	27	-15	-40
-46	-40	-25	1	22	27	22	1	-25	-40	-46

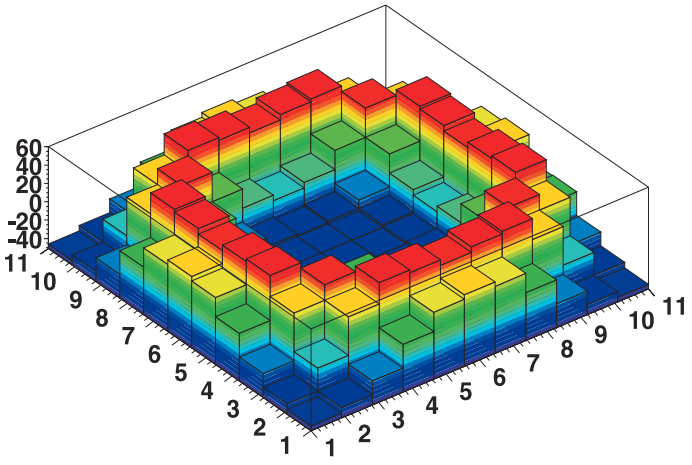

Figure 3.6: Schematic of the pattern matrix method for the ring finding.

The final criterion used for the ring image recognition requires a coincidence between both algorithm with an additional threshold condition set on the ring local maxima values. The quality of each correctly reconstructed ring can be characterized by the following parameters:

- ring centrality (RC), difference between the charge center of gravity as deduced from the pulse heights and the fitted geometrical center of the ring,
- number of fired pads that compose a ring (NP),
- pattern matrix quality (PM),
- average charge (AC), sum of the charges of all pads that compose a ring.

Fig. 3.3 shows the typical distributions for the ring parameters: pattern matrix (a), average charge (b), ring centroid (c) and number of fired pads (d). The vertical red lines represent the threshold value on which the cut has been applied.

The RICH rings position have been spatially correlated with the correctly reconstructed tracks in the inner MDC drift chambers.

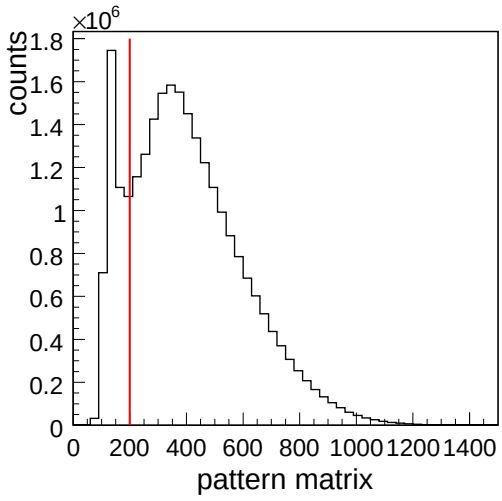
×10^6
counts
1.8
1.6
1.4
1.2
1
0.8
0.6
0.4
0.2
0
0 200 400 600 800 1000 1200 1400
pattern matrix

(a)

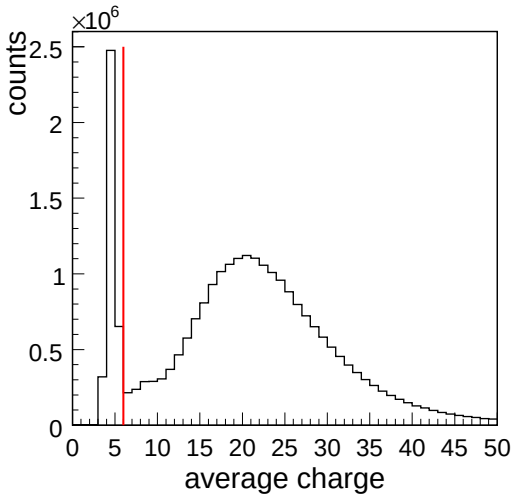
×10^6
counts
2.5
2
1.5
1
0.5
0
0 5 10 15 20 25 30 35 40 45 50
average charge

(b)

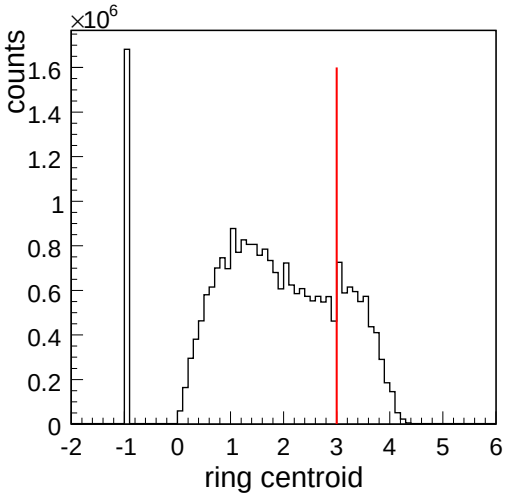
×10^6
counts
1.6
1.4
1.2
1
0.8
0.6
0.4
0.2
0
-2 -1 0 1 2 3 4 5 6
ring centroid

(c)

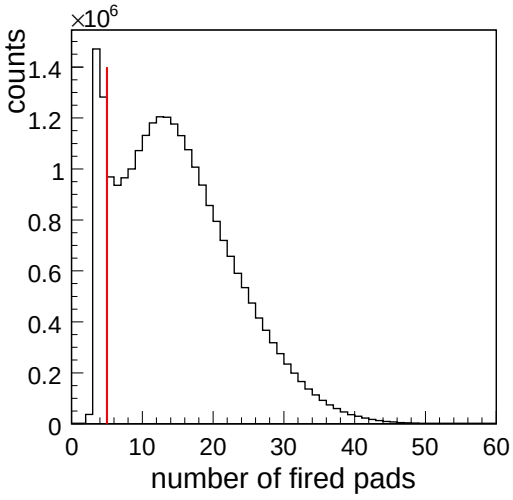
×10^6
counts
1.4
1.2
1
0.8
0.6
0.4
0.2
0
0 10 20 30 40 50 60
number of fired pads

(d)

3.4 Spatial correlation of the RICH hits and the inner MDCs segment

The polar and azimuthal angles of the reconstructed segments in the two inner chambers of the MDC detector must be matched with the polar and the azimuthal angles of ring candidates. Angular correlation is done in 2 steps. First, in the pre-analysis very coarse windows are applied ($\Delta\theta$ = $\pm$ 7^o, $\Delta\phi\sin(\theta)$ = $\pm$ 7^o). The difference in the azimuthal angles between the hits is multiplied by $sin\theta$ to keep the solid angle spanned by the correlation constant as function of polar angle [see. [53]]. Angular correlation is done by creating all possible correlations between rings found by the RICH and the inner MDCs segments which have been used to reconstruct a track. Fig 3.7 shows the matching distributions as function of both angles of the lepton candidates. In the second step of the analysis, tighter matching windows are applied; computed separately for each sector of the spectrometer and with 100 MeV/c steps in momentum (for details see Appendix E). In order to improve the matching precision, a pre-selection of the ring was done by applying a condition on the pattern matrix (PM > 200). A condition on the χ^2 of the track segment has been applied as well.

The correlation signal is fitted with a Gauss function (red line); the background is fitted with the sum of a second Gaussian (blue line) and a constant (pink line)(for details see Appendix E).

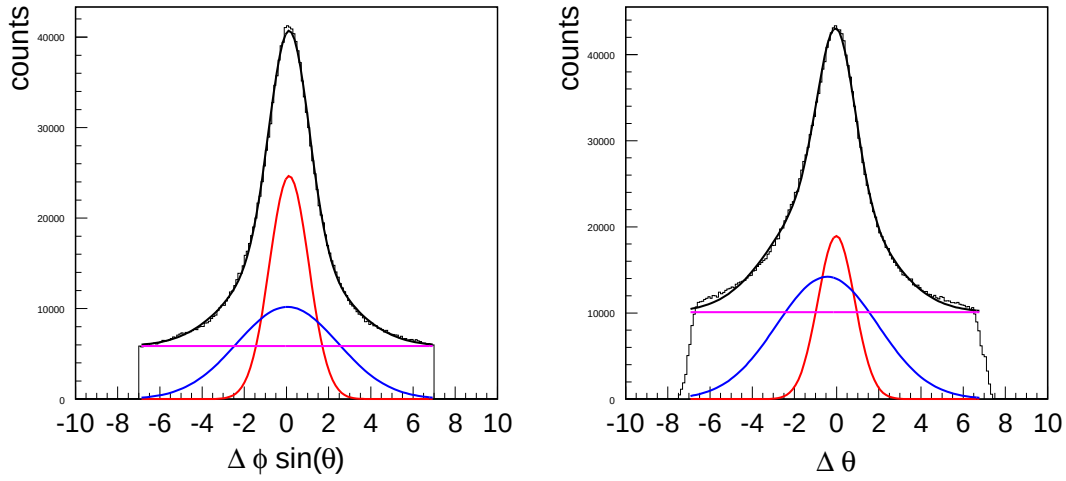

(e) polar correlation

(f) azimuthal correlation

Figure 3.7: Spatial correlation between RICH hits and inner MDCs segment

To select good lepton tracks in the experiment, as well as in the simulation, 2 σ matching windows have been derived:

$$-2\sigma < \Delta\phi\dot{\sin}(\theta) < 2\sigma \tag{3.4}$$

$$-2\sigma < \Delta\theta < 2\sigma \tag{3.5}$$

where $\Delta\phi$ and $\Delta\theta$ are differences in the azimuthal and the polar angles respectively.

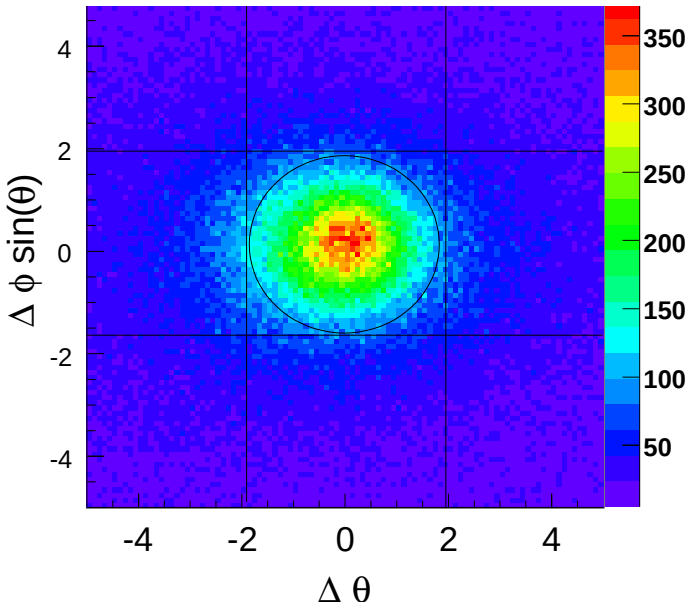

Figure 3.8: Angular correlation between RICH rings and MDCs segments.

Figure 3.8 shows in two dimensions the correlation between the azimuthal and polar angles of the RICH rings and the MDC hits. The straight lines correspond to 2σ cuts in this distribution. They correspond to an independent cutting in $\Delta\theta$ and $\Delta\phi\sin(\theta)$. This results in an inhomogeneous background. The biggest impact on the width of the signal distribution has the position resolution of the RICH detector (1%) and multiple scattering (1% for low momentum leptons) (see Appendix E).

3.5 Lepton identification in the Pre-Shower detector

The main task of the Pre-Shower detector is to improve the lepton identification e^+ and e^- by further reducing the hadron contamination. Lepton identification in the Pre-Shower detector [83, 84] is based on the integrated charge deposited in the pre- and post-converter chambers (see Fig. 3.9). In addition, the information on the energy loss in the pre-converter is used to eliminate slow hadrons with large ΔE.

Based on experimental results and dedicated Monte Carlo simulations a procedure for selecting electron candidates was developed. It consists of the following steps:

- finding of local maxima in the charge distributions in the pre-chamber
- integrating the charge in the pre-converter (Sum$_{pre}$), post1-converter (Sum$_{post1}$) and post2-converter (Sum$_{post2}$) at the same position (see Fig. 3.9).

- finally applying one of the following electron identification algorithms:

  1. constant threshold F_{th1}, F_{th2}

$$\frac{Sum_{post1}}{Sum_{pre}} \equiv F_{max} \geq F_{th1} \tag{3.6}$$

     or

$$\frac{Sum_{post2}}{Sum_{pre}} \equiv F_{max} \geq F_{th2} \tag{3.7}$$

     where F_{th1} and F_{th2} are the threshold values

  2. momentum dependent thresholds $F_{th1}(p)$, $F_{th2}(p)$

$$\frac{Sum_{post1}}{Sum_{pre}} \equiv F_{max} \geq F_{th1}(p) \tag{3.8}$$

     or

$$\frac{Sum_{post2}}{Sum_{pre}} \equiv F_{max} \geq F_{th2}(p) \tag{3.9}$$

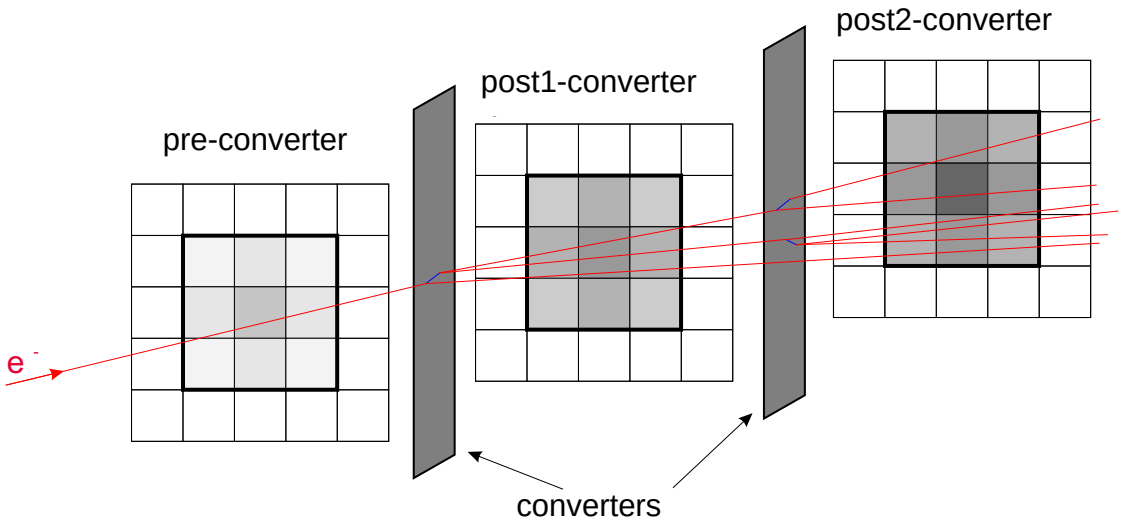

Figure 3.9: Schematic view of the electromagnetic shower identification in the Pre-Shower.

The thresholds for both algorithms have been adjusted based on simulation and are shown in Fig. 3.10.

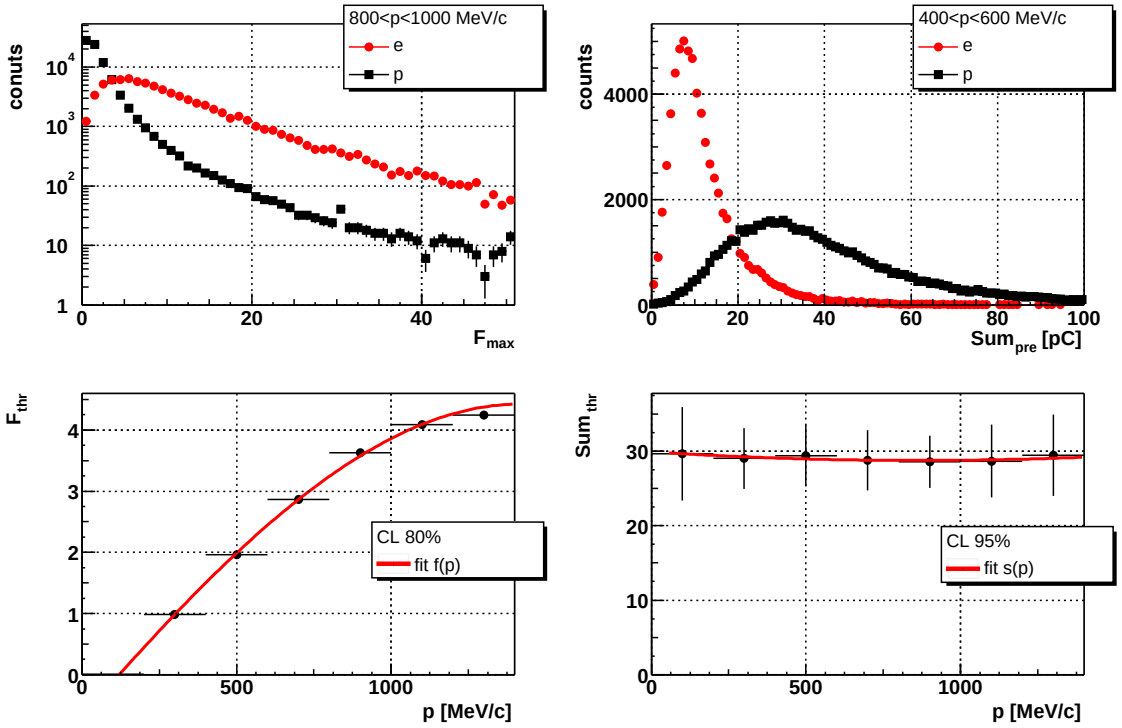

Figure 3.10: Pre-Shower parametrization.

In case of the constant threshold algorithm, the threshold was optimized in order to get the best ratio of recognized electrons to fake ones (protons/pions). For such a threshold the number of accepted electrons at (p = 850 MeV/c) amounts to 80 % and the number of recognized fake electrons is about 10 % (efficiency = 80 %, purity = 90 %).

The momentum-dependent thresholds were optimized to maintain a constant electron recognition efficiency of 80 % over the whole momentum range at the expense of more fakes at low momentum. This kind of threshold means that 80 % of the leptons entering the Pre-Shower detector pass the condition for F_{max} and 95 % pass the condition for Sum_{pre}. The value of $F_{th}(p)$ strongly depends on the momentum of the particle. Lepton candidates which have F_{max} = 0 are not taken into account in further analysis.

The fake contamination can be further reduced without affecting the electron efficiency by applying an additional condition on the TOF and TOFINO detectors, as described below.

3.6 Time-of-flight cut

For lepton candidates which survive the cut on minimum bias ring candidates and the Pre-Shower cut, an additional condition has been applied, based on the time-of-flight information given by the TOF and TOFINO detectors.

Leptons which are traveling with a velocity close to the speed of light have a $\beta \sim 1$, which helps us to distinguish them from hadrons. The correlation between the measurement of β in the TOF, TOFINO detector and the momentum is presented in the Fig. 3.12 and 3.11.

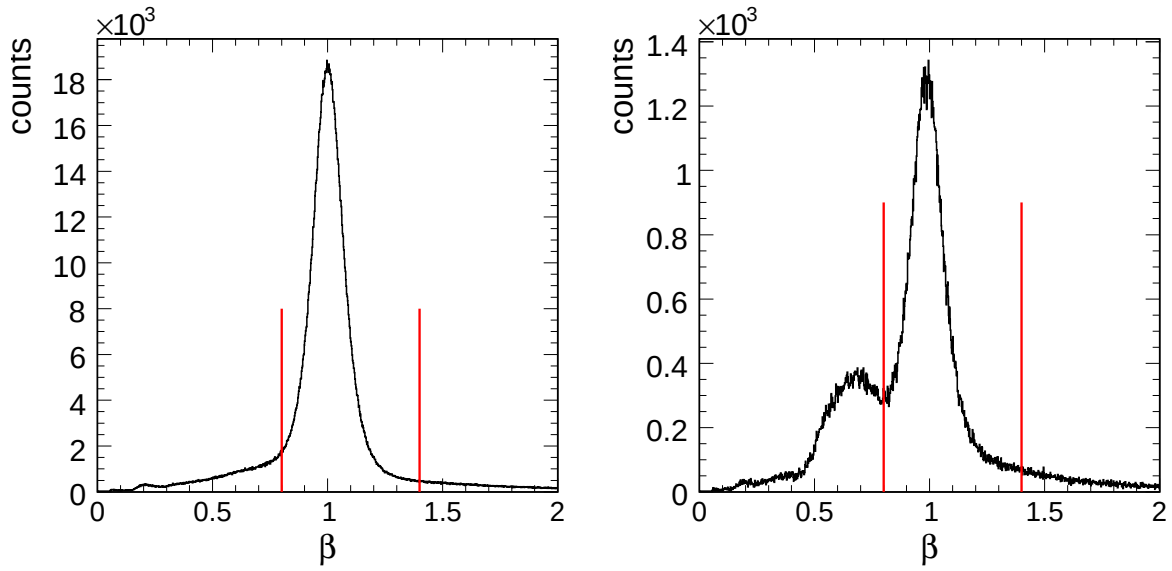

(a) p < 0.5 GeV/c (b) 1 GeV.c > p > 0.5 GeV/c

Figure 3.11: β calculated in the TOFINO detector in two momentum bins

In case of the TOFINO detector only a lower limit on β has been used. 40 % of the events (for C+C@2AGeV) have a multiplicity of more than 1 in a TOFINO pad. As a consequence we are not able to properly calculate the time of flight of those particles. Usually one of them has a too low value of time-of-flight which translates eventually to $\beta > 1$. Applying an upper limit on β would cut out those particles.

A 3σ cut on the β distribution as a function of momentum has been applied, presented as red lines in Fig. 3.11 and Fig. 3.12.

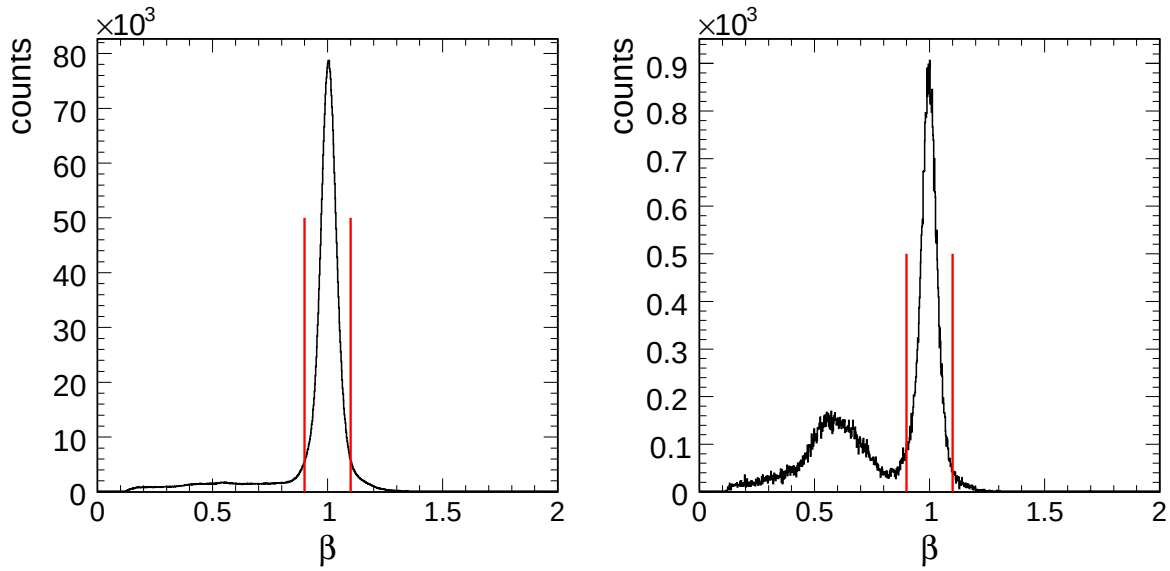

(a) p < 0.5 GeV/c (b) 1 GeV.c > p > 0.5 GeV/c

Figure 3.12: β calculated in the TOF detector in two momentum bins

3.7 Results

The final selection of "good" leptons is made by applying all cuts which were described above:

- cut0 - spatial correlation of the detectors RICH - inner MDC
- cut1 - RICH ring quality
- cut2 - TOF and TOFINO beta vs. particle momentum windows
- cut3 - lepton identification in the Pre-SHOWER detector

There is no special reason why the cuts should be applied in the order they are listed above. Cut number 1 (cut1) could be applied before cut0, as well as cut2 or cut3. However it appears, that the mentioned above order of cuts is preferable for particular reasons, which will be explain below.

Table 3.1 shows the relative reduction of the positive and negative lepton yields as a function of the cut number.

One can see that the suppression of positive particles is larger than for the negative one, especially after the Pre-Shower condition is applied. Positive particles are bent inwards by the magnetic field and hit preferentially the Pre-Shower detector (cut3 is not active in the TOF

CUTs	e^+ candidates	e^- candidates
Matching	100 %	100 %
RICH quality	93 %	91 %
TOF/Tofino	81 %	79 %
Pre-Shower	75 %	63 %

Table 3.1: Cut efficiency of the single-lepton candidates in the experiment.

region !). Figure 3.13 shows the measured momentum distributions after all cuts. The average value of the lepton momentum is around 150 MeV/c.

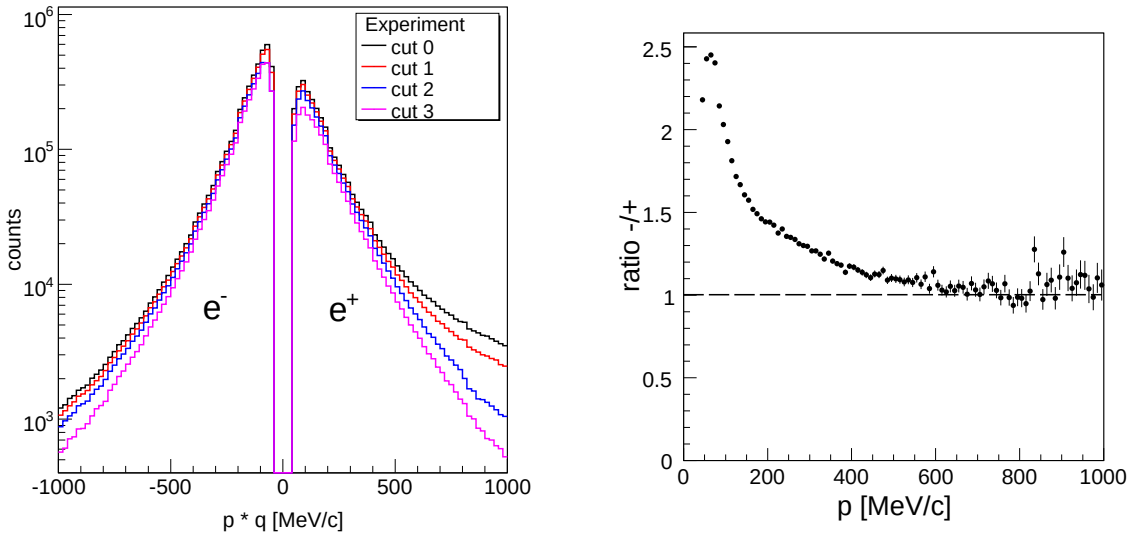

(a) Comparison of the experimentally reconstructed and simulated momenta distributions.

(b) Ratio of the experimental momentum distribution after all single lepton cuts.

Figure 3.13: Momentum distribution of the lepton candidates.

The amount of positive particles with the momenta above 400 MeV/c shows clearly a big contamination from protons, in addition to pions (see, Fig 3.13 (a)). This difference in yield became close to 1 after all lepton cuts have been applied, what is shown in Fig. 3.13 (b). This shows also that after all cuts are applied the contamination of the protons in the lepton sample is very small. Larger yield of the low momenta electrons as compared to positrons is due to the fact, that the positrons are bent inwards and out of the HADES acceptance.

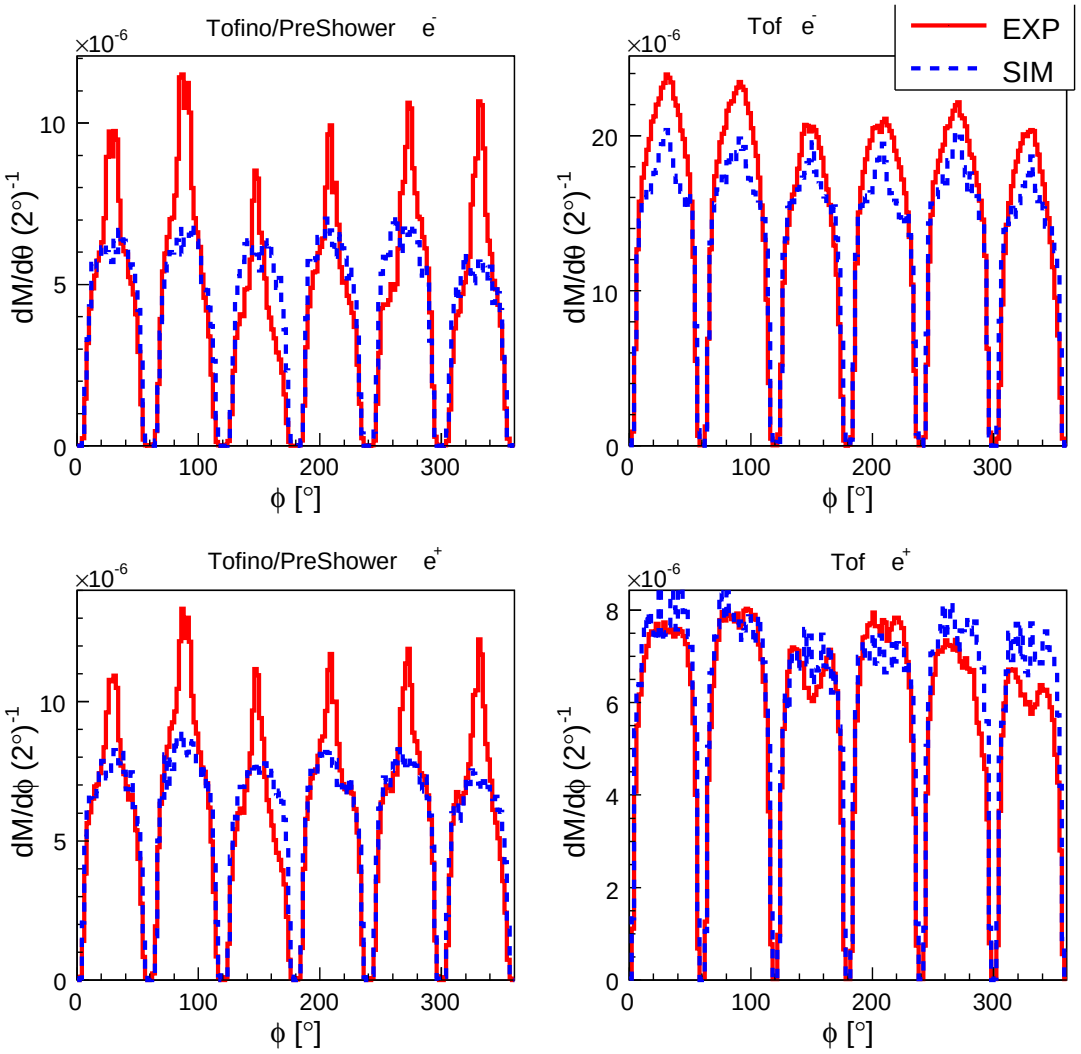

Figure 3.14: Reconstructed distribution of the azimuthal emission angle for positrons and electrons separately in the experiment and simulation.

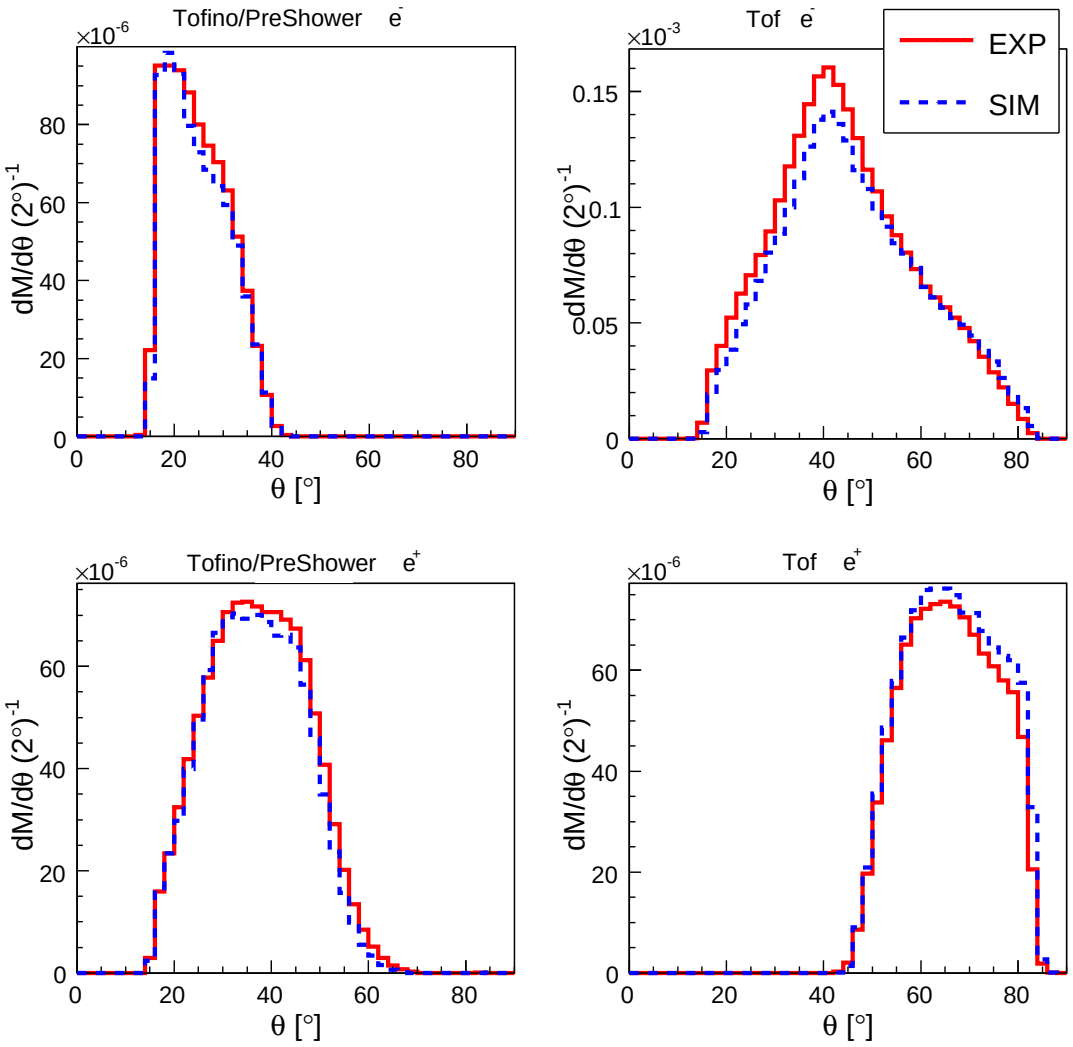

Figure 3.15: Reconstructed distribution of the polar emission angle for positrons and electrons separately in the experiment and simulation.

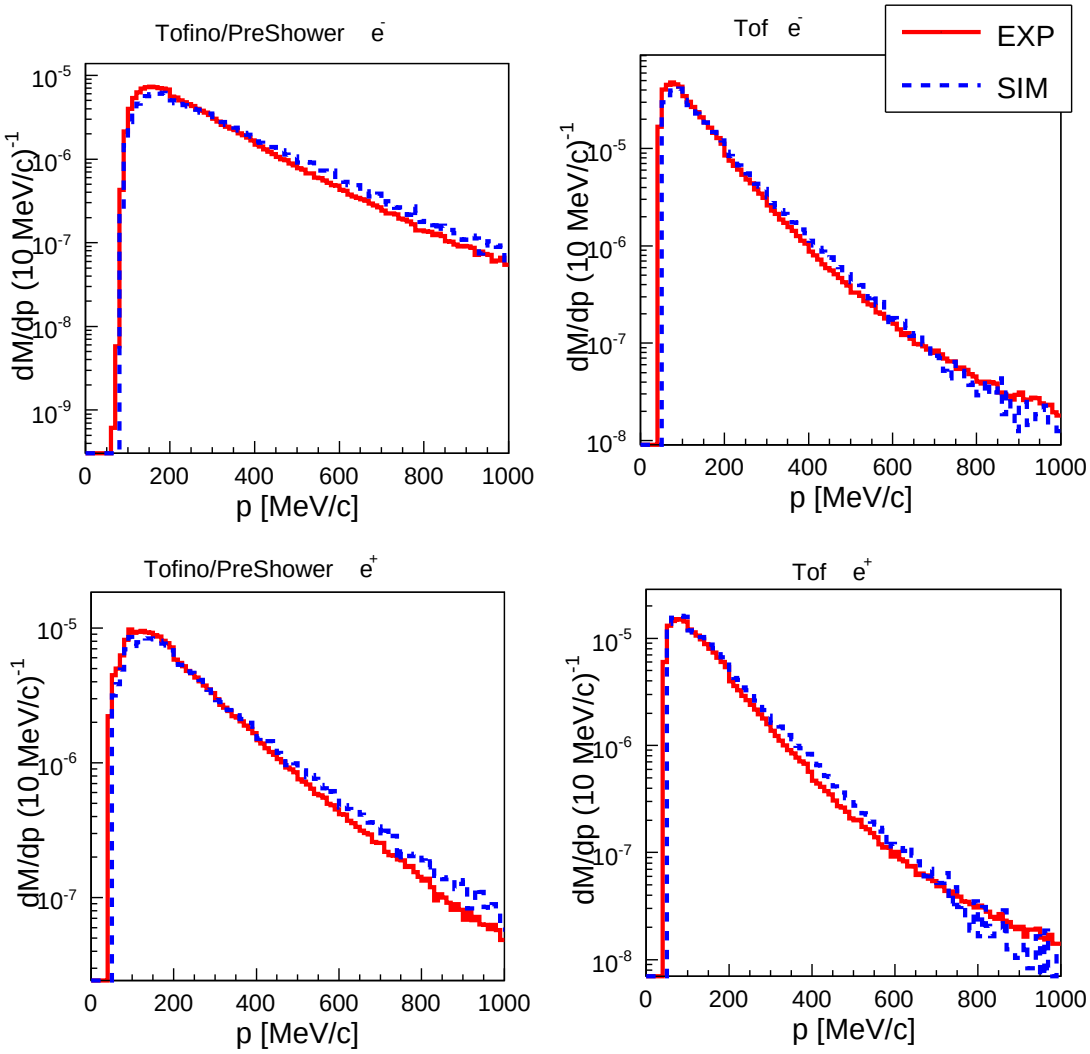

Figure 3.16: Reconstructed distribution of momenta for positrons and electrons separately in the experiment and simulation.

For all figures presenting comparison between leptons yield in experiment and Monte Carlo simulation (UrQMD) distributions are normalized to the corresponding number of LVL1 event with at least one track inside[1].

Figure 3.14 shows the azimuthal emission angle of the leptons for both charges and systems. The separation between different sectors is visible due to the reduction of efficiency at the borders of the sectors. The discrepancy between the simulation and the experimental data visible around mid-sector in the azimuthal distribution for the TOFINO/PreShower is caused by a wrong matching between the PreShower and RICH hits in the second level trigger algorithm used in the NOV02 data run.

The figure 3.15 shows the polar emission angles of the leptons. Electrons emitted at large polar angle are bent out of the HADES acceptance. Therefore the reduction of the yield at high polar angles is visible. Positrons, which are emitted at small polar angle, but having high momenta are less bent and their yield stays relatively high at small polar angles. Fig. 3.16 shows comparison of lepton momenta distributions for the experiment and simulation.

On average, simulation shows very good agreement (within 10%) with the experimental data.

Using the available information in the PLUTO simulation one can determine how good the reconstruction of a lepton track is by checking purity and efficiency of the applied analysis cuts. Figure 3.17 shows the characteristics of the leptons as a function of momentum multiplied by charge for the META detector.

By purity we understand the ratio of all the e^+/e^- (with correctly reconstructed tracks) after all applied cuts to all particles reconstructed as e^+/e^-. Efficiency is the ratio of e^+, e^- with correctly reconstructed tracks after all cuts to the initial number (before any cut has been applied) of e^+, e^- with correctly reconstructed tracks.

$$Purity = \frac{L_{cut}^{true}}{L_{cut}^{rec}} \tag{3.10}$$

$$Efficiency = \frac{L_{cut}^{true}}{L_{cut0}^{true}} \tag{3.11}$$

where L_{cut}^{true} are the leptons with the correctly reconstructed tracks after all single lepton cuts, L_{cut}^{rec} all particles reconstructed as leptons after all cuts, L_{cut0}^{true} the number of all leptons with correctly reconstructed tracks before any cut has been applied.

The purity of identified leptons in the TOFINO/Pre-Shower for momenta above 200 MeV/c is constant and is of the order of 90%. For the lower momenta one can see a strong dependence on momentum. Low momentum particles are bent in the magnetic field and can leave the

[1]In simulation the LVL1 condition is emulated, so the event sample should be fully equivalent to the experimental one. Normalization is done to events with at least one track. the reason for this is to take into account experimental effect which creates a positive LVL1 trigger decision due to noise, a track coming not from the target.

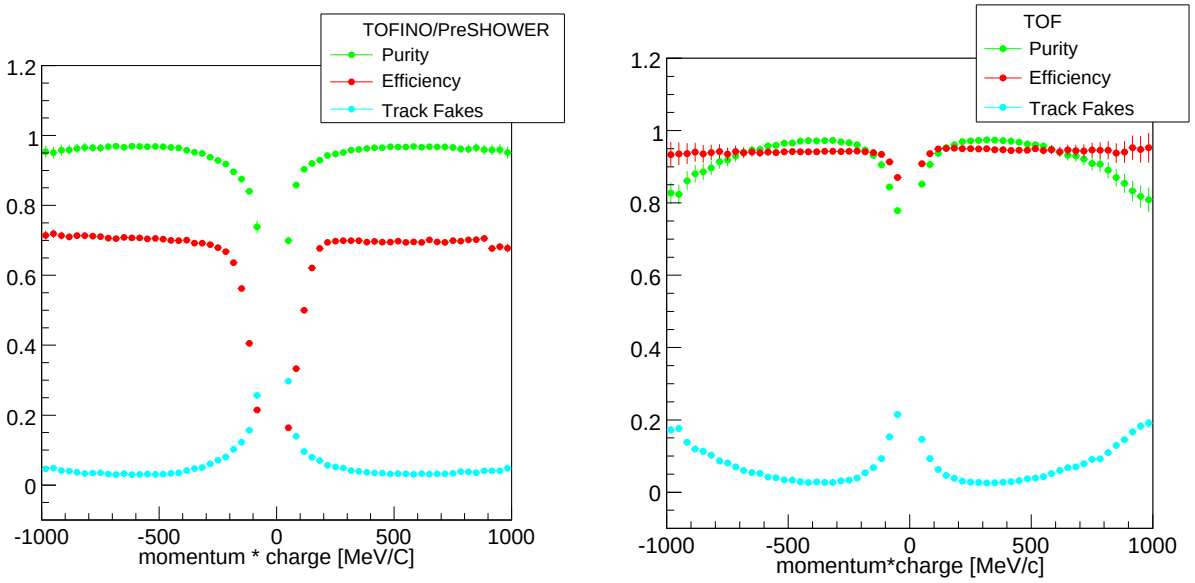

(a) TOFINO/Pre-Shower (b) TOF

Figure 3.17: Efficiency and purity of the lepton sample after all applied cuts

HADES acceptance. In this case part of the tracks in front of and behind the magnetic field are randomly combined with each other. The efficiency of the applied cuts for the system 0 is quite low: 75% for p > 200 MeV/c and even down to 20% for very slow leptons. The reason for this is the momentum-dependant cut of the Pre-Shower detector.

In case of the system 1 (TOF, 3.17) the efficiency and purity are almost constant as a function of momentum of the leptons and amount to 95% and 85% respectively. However for high momentum particles (p > 700 MeV/c), the purity of the lepton sample is decreasing. The reason for this is the contamination by protons and pions which have a velocity close to $\beta = 1$. Looking to the whole HADES spectrometer the purity of the lepton sample is on average 90% and the efficiency of the cuts is 75%. Contamination of fake leptons dominate the low momentum region (15%). Using available information in the simulation it has been checked that the 21% of the track fakes correspond to the case, when there is no hit in the META detectors (only RICH and inner MDCs) and 71% had missing MDC hit (only RICH and META).

Contamination from the real hadron tracks (protons and pions) identified as leptons is very small (less then 5%). This means that hadrons are not the main source of the background, which is mostly dominated by fake leptons.

Main source of the wrongly identified lepton is connected with the method which is used for the track reconstruction. Electron pairs which are coming from the gamma conversion usually do not have enough momentum that both tracks can pass through the magnetic field.

It is likely that one of the leptons is bend out and only one track is registered in the detectors after the magnetic field. Tracking method is joining parts of the track from before and after the magnetic field, creating in this way one or even more wrong combination, what is shown schematically in Fig. 3.18. Conversion pairs in addition have very small opening angle. Very often it happens that they are seen as one hit.

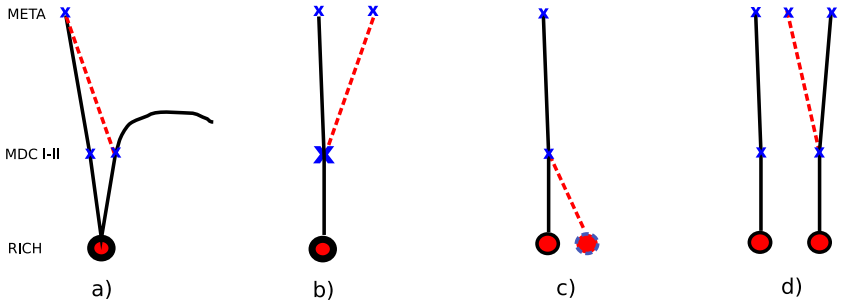

Figure 3.18: Main sources of the wrongly identify leptons.

Clear electron identification with the HADES spectrometer was thus proven even in the so-called *low-resolution* tracking method. Further improvements in this respect are foreseen using the full setup of the tracking detectors [85].

Fig. 3.19 shows comparison of the multiplicity for electrons and positrons in simulation and experiment. The mean multiplicities are around 1.0, as well in simulation as in experiment.

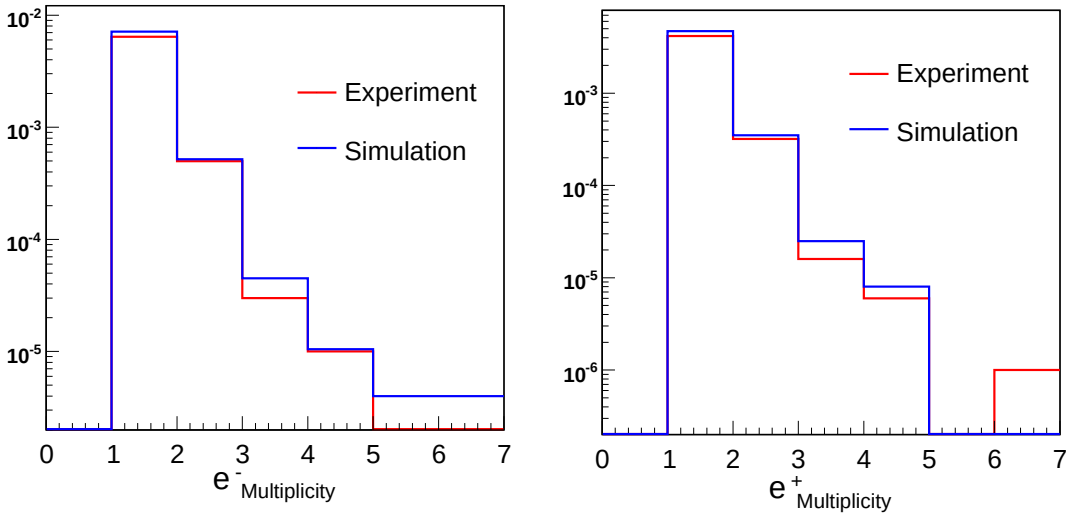

(a) Multiplicities of the electrons.

(b) Multiplicities of the positrons.

Figure 3.19: Comparison of the lepton multiplicities in the experiment and simulation. All spectra are normalized to the corresponding number of events.

Looking into the two dimensional representation of the multiplicities in the experiment Fig. 3.20 one can see that only 30 % of analyzed events are taken into account for the analysis of like-sign and unlike-sign pairs, the remaining 70 % has only one lepton per event.

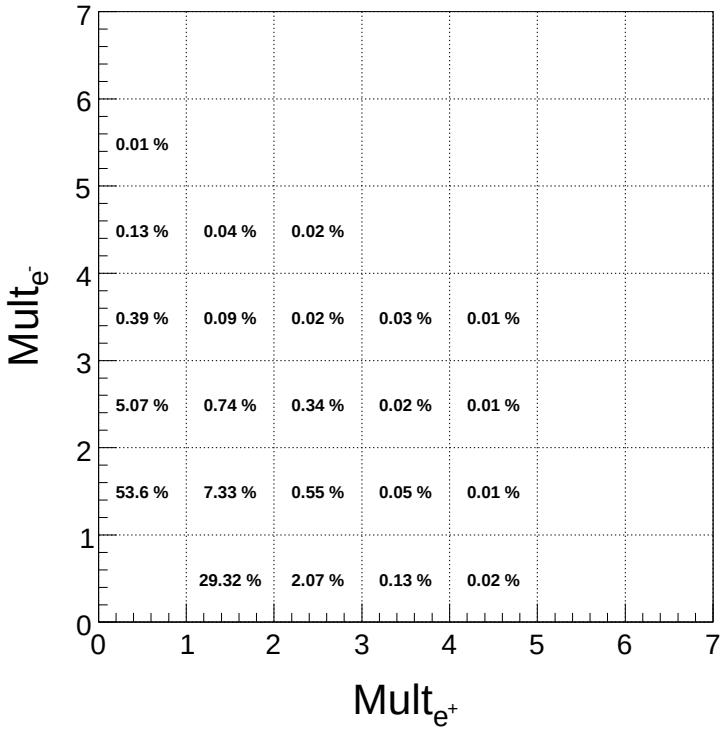

Figure 3.20: Correlation of electron and positron multiplicities per event. All cuts defining single lepton tracks have been applied.

Chapter 4

Dilepton analysis

4.1 Introduction

Dileptons represent a unique probe for nuclear matter under extreme conditions. They allow to study meson properties, like mass and decay width, at various density and temperature regimes. The final aim of the HADES experiment is to identify those lepton pairs, which are originating from the same decay vertex (true pairs).

The following chapter is dedicated to the description of the analysis steps to suppress combinatorial background and to obtain a clean signal of the true pairs.

The invariant mass of the lepton pair is defined by the following equation:

$$M_{e^+e^-}c^2 = \sqrt{(E_{e^+} + E_{e^-})^2 - (\vec{p}_{e^+}c + \vec{p}_{e^-}c)^2} \tag{4.1}$$

where E_{e^+}, E_{e^-} are the total energies and p_{e^+}, p_{e^-} are the momenta of the positron/electron in the laboratory system respectively, and c is the velocity of light (and $|\overrightarrow{p}|$=p). For leptons with energies $E_{e^\pm} \gg m_{e^\pm}$ = 0.511 MeV/c^2, Eq. 4.1 can be written as:

$$M_{e^+e^-}c^2 = \sqrt{2c^2 \cdot p_{e^+}p_{e^-}(1 - \cos\theta_{e^+e^-})} = 2c \cdot \sin(\theta_{e^+e^-}/2) \cdot \sqrt{p_{e^+}p_{e^-}} \tag{4.2}$$

where $\theta_{e^+e^-}$ is the opening angle of the pair.

The two dominant sources of lepton pairs detected with HADES are the electromagnetic decay of π^0 mesons and photon conversion in the target, the RICH radiator and the carbon shell of the RICH:

- external conversion, i.e. pair creation: $\pi^0 \rightarrow \gamma(\gamma \rightarrow e^+e^-)$
- Dalitz decays of the π^0 meson: $\pi^0 \rightarrow \gamma e^+e^-$

At intermediate and high masses, the remaining (and interesting) pairs occur from:

- η Dalitz: $\eta \rightarrow \gamma e^+ e^-$
- Δ Dalitz, N^* Dalitz, ω Dalitz $\rightarrow \gamma e^+ e^-$
- pn Bremsstrahlung
- and vector meson decays: $\rho, \omega, \phi \rightarrow e^+ e^-$

In the following sub-sections we will concentrate on the analysis steps which have to be taken in order to identify lepton pairs coming from meson and baryon decays.

4.2 Origin of the background

In the final step of data processing, electron/positron tracks are combined into 3 groups of pairs e^+e^+, e^-e^- and e^+e^-. The aim is to extract the spectral distribution of true pairs by subtracting from all pairs those which are formed by combining tracks originating from different decays. To achieve this a pairing is done by creating all possible combination of electron and positron tracks from the same event. Integrating over all events, spectra of unlike-sign and like-sign pairs are obtained. The total spectrum of unlike-sign pairs consists of the true pairs which are of interest, as well as of the uncorrelated ones, which are combinatorial background. Fig.4.1 shows the obtained invariant mass distribution for the like-sign and unlike-sign pairs.

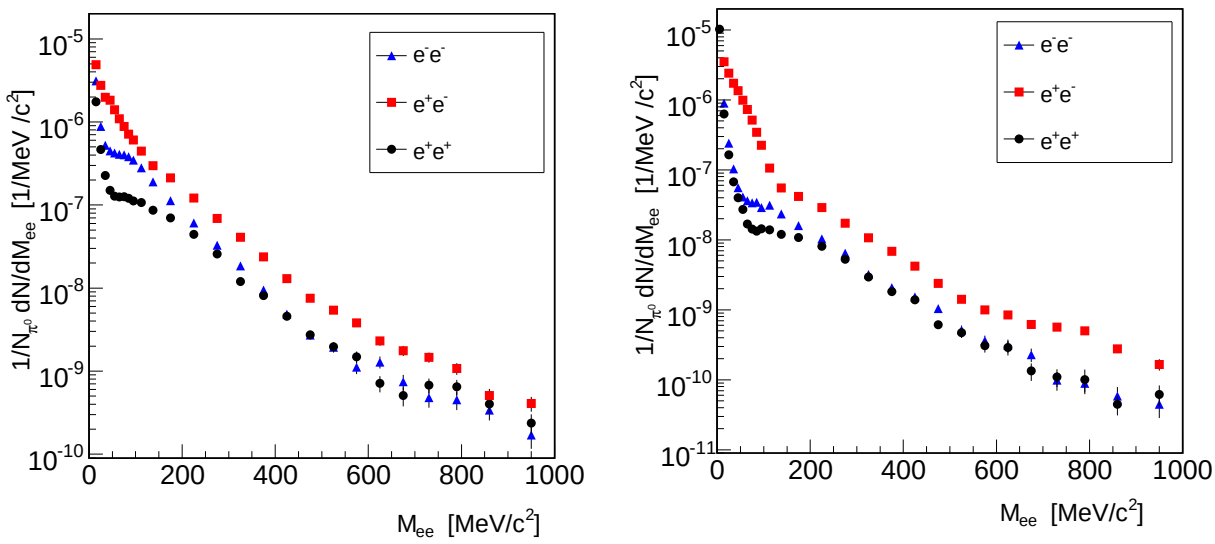

(a) Experiment (b) Simulation

Figure 4.1: Distribution of the invariant mass of like-sign and unlike-sign pairs.

The background pairs can be classified in the following way:

- combinatorial pairs, made from true electron- and positron tracks
  - uncorrelated, where each leg of the pair comes from different decay source (see, Fig. 4.2),
  - correlated, where each leg comes from the different mother particle, but still from the same grandmother (see, Fig. 4.3)
- fake pairs, made from one or two fake electron positron tracks (see, Fig. 3.18).
  - misidentified hadrons,
  - tracks which occur in the analysis, but are not produced by a particle traveling along this track.

Like-sign pairs, e^-e^- and e^+e^+, are very unlikely (e.g, $\eta \rightarrow e^+e^-e^+e^-$, BR < $6 \cdot 10^{-5}$) to come from the same decay source and therefore mostly are created only by combining leptons from different decay vertices. Due to random combination of like-sign pairs, their invariant mass distribution should not have any structure, but rather smooth. However, as one can see in Fig.4.1, in the region of small invariant masses (M_{ee} < 100 MeV/c^2) a clear peak is visible. There are several reasons for such correlations of like-sign pairs. Fig. 4.2 shows an example of all combination for the like-sign and unlike-sign pairs.

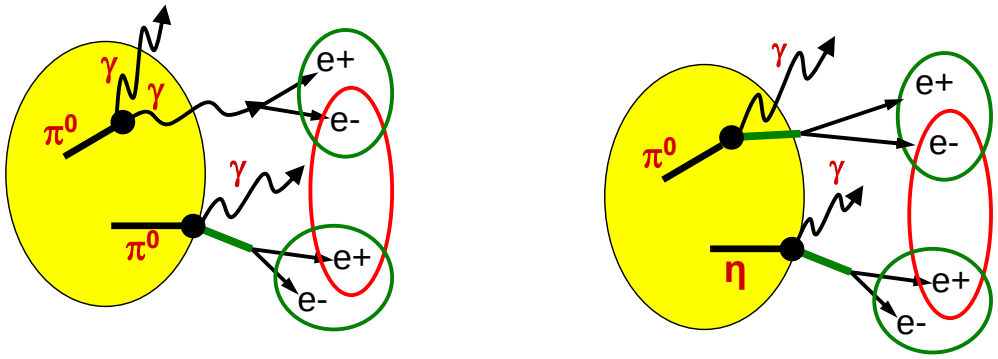

Figure 4.2: Example of the combinatorial pairs, created by combining tracks coming from the π^0 Dalitz and η Dalitz decays which happen inside one event.

4.3 Reconstruction of the background

As said before, the total unlike-sign pair spectrum ($N^{tot}_{e^+e^-}$) consists of correlated pairs which correspond to the real physical signal (S_{+-}) originating from the same decay, and of uncorre-

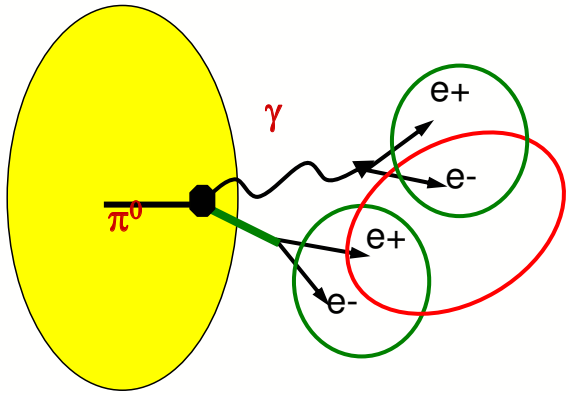

Figure 4.3: Example of a correlated combinatorial pair created by a single π^0 Dalitz decay. Green circles represent the true pairs, the red one shows the correlated background pair.

lated unlike-sign pairs randomly formed as combinatorial background ($CB_{e^+e^-}$). It is necessary to reconstruct the $CB_{e^+e^-}$ and to subtract it from $N^{tot}_{e^+e^-}$.

$$S_{+-} = N^{tot}_{e^+e^-} - CB_{e^+e^-} \tag{4.3}$$

One of the main sources of the combinatorial background is due to uncorrelated leptons from π^0 Dalitz and γ conversion pairs.

The reconstruction of the combinatorial background can be established by two methods:

- the like-sign same-event combinatorial background,
- the mixed-event technique.

The *like-sign pair same event technique* is based on the fact that the same-event combinatorial like-sign background is a good approximation for the combinatorial unlike-sign background, in the absence of strongly correlated like-sign pairs of physics origin. This technique has however the disadvantage that the statistics in the background spectrum is limited to the number of available events.

$$CB^{same}_{+-} = 2\sqrt{N_{e^-e^-}N_{e^+e^+}} \tag{4.4}$$

The geometrical mean has an advantage over the arithmetical one, that the pair efficiency can be factorized from the single efficiency:

$$\epsilon_{++} = \epsilon^2_+\epsilon_{+-} = \epsilon_+ \cdot \epsilon_-\epsilon_{--} = \epsilon^2_- \tag{4.5}$$

For the *mixed-event technique* [86], the pairs of the unlike-sign background are created by combining particle tracks from different events. Those pairs are uncorrelated by construction.

Compared to the same event like-sign method this method offers a much better statistical precision, since one can mix the tracks of each event with the tracks of many other events. As one can see, the like-sign as well as the mixed event technique have their own advantages and disadvantages, depending on the particular environment.

In the present analysis both methods have been used for the background determination. In the low-mass region, where contribution from correlated background is still visible, the like-sign same-event method has been used (M_{ee} < 0.15 GeV/c^2). Starting from invariant mass M_{ee} > 0.15 GeV/c^2 the opposite-sign mixed event strategy has been used, to compensate for the decreasing statistics at high invariant masses.

Fig.4.4 and Fig.4.6 show a comparison of the background obtained with both methods (for the like-sign pairs) as a function of invariant mass, opening angle (θ_{ee}), transverse momentum ($P_\perp$) and rapidity (Y) after efficiency correction (how the efficiency correction is done will be described in the next section). For the presentation of the opening angle, rapidity and transverse momentum distributions a cut for the lower value of the invariant mass has been applied (M_{ee} < 0.15 GeV/c^2). These distributions are normalized on each other in the following ranges:

- invariant mass 0.15 MeV/c^2 < M_{ee} < 0.5 GeV/c^2
- opening angle $40^o < \theta < 100^o$
- transverse momentum 0.15 GeV/c < $P_\perp$ < 0.5 GeV/c
- rapidity 0 < Y < 1.99

For the low invariant-mass region differences between the two distributions are clearly visible. This can be traced back to the correlated background problem. This kind of correlation cannot be reproduced in the event mixing method, since everything is happening inside one decay mother (see, Fig. 4.3). For the masses above π^0 region reasonable agreement between the same event and the mixed event background is observed. Applying condition for the masses above the π^0 mass, one gets also a good agreement in the opening angle distribution, as well as in the $P_\perp$ and Y.

However before the combinatorial background can be subtracted, several conditions have to be applied to suppress the fake lepton pairs from the like-sign, as well as from unlike-sign pairs. The rejection strategy will be described in the following subsection.

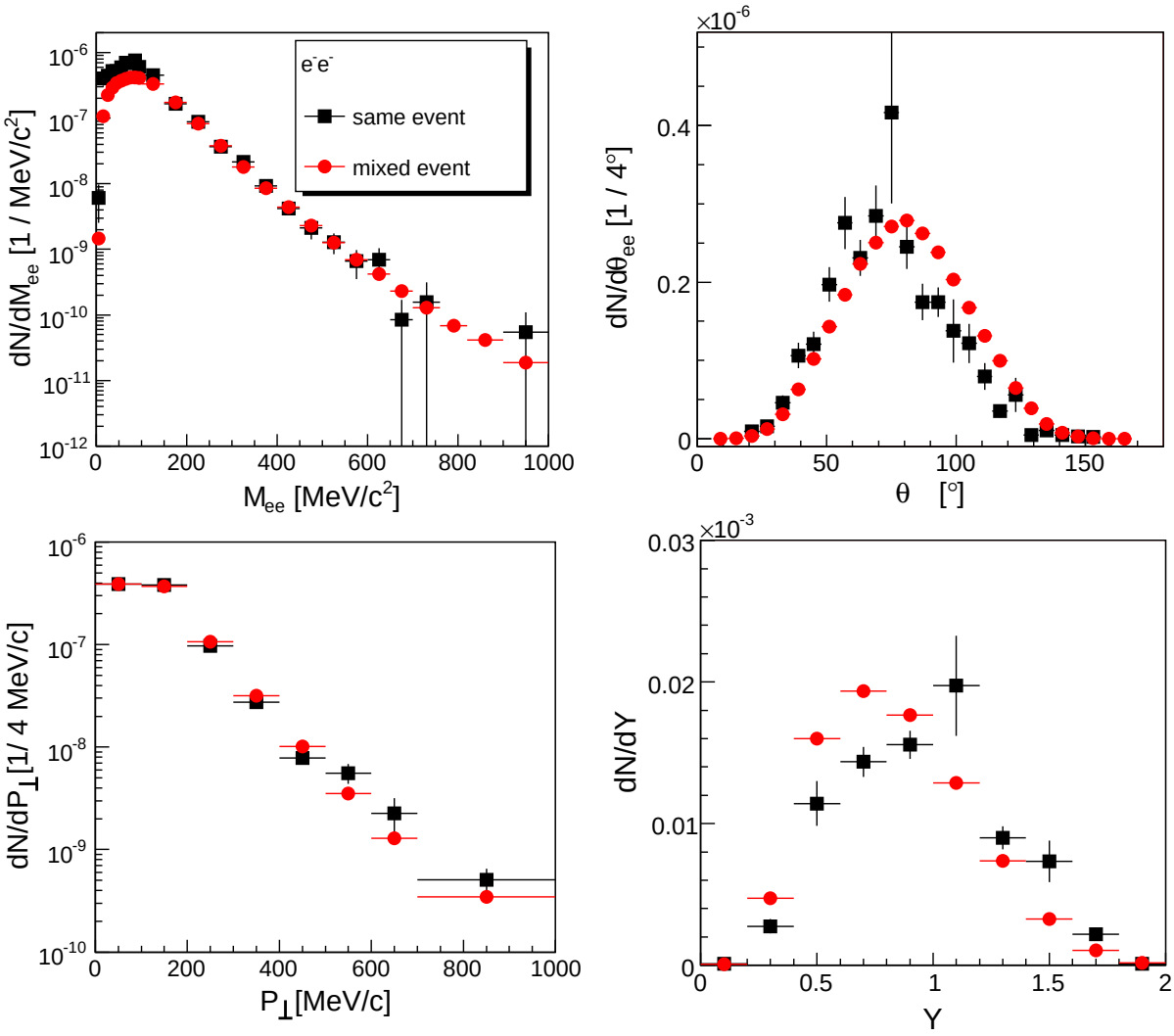

Figure 4.4: Comparison between the experimental like-sign (e^-e^-) same event (squares) and mixed event (dots) pair distributions.

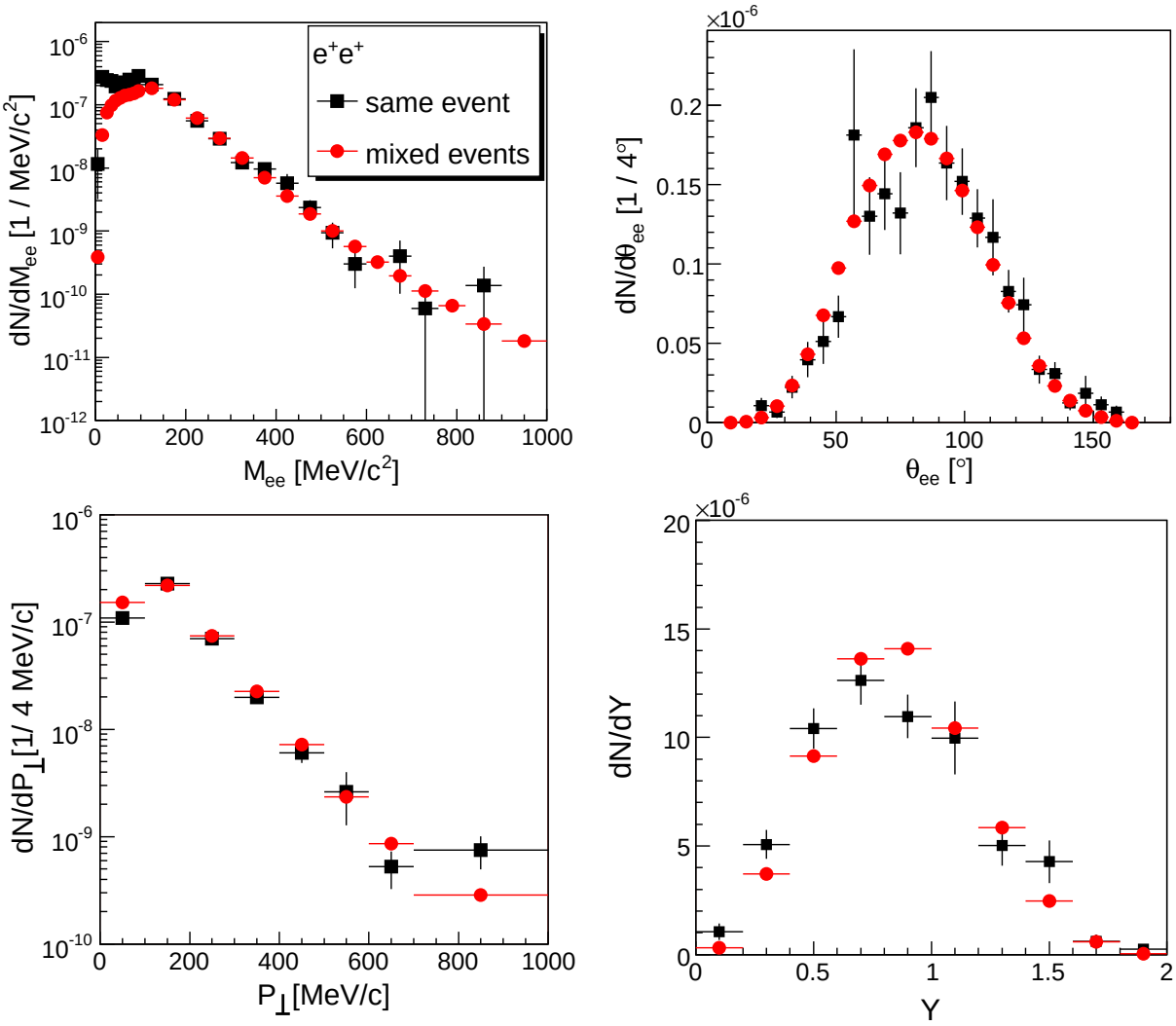

Figure 4.5: Comparison between the experimental like-sign (e^+e^+) same event (squares) and mixed event (dots) pair distributions.

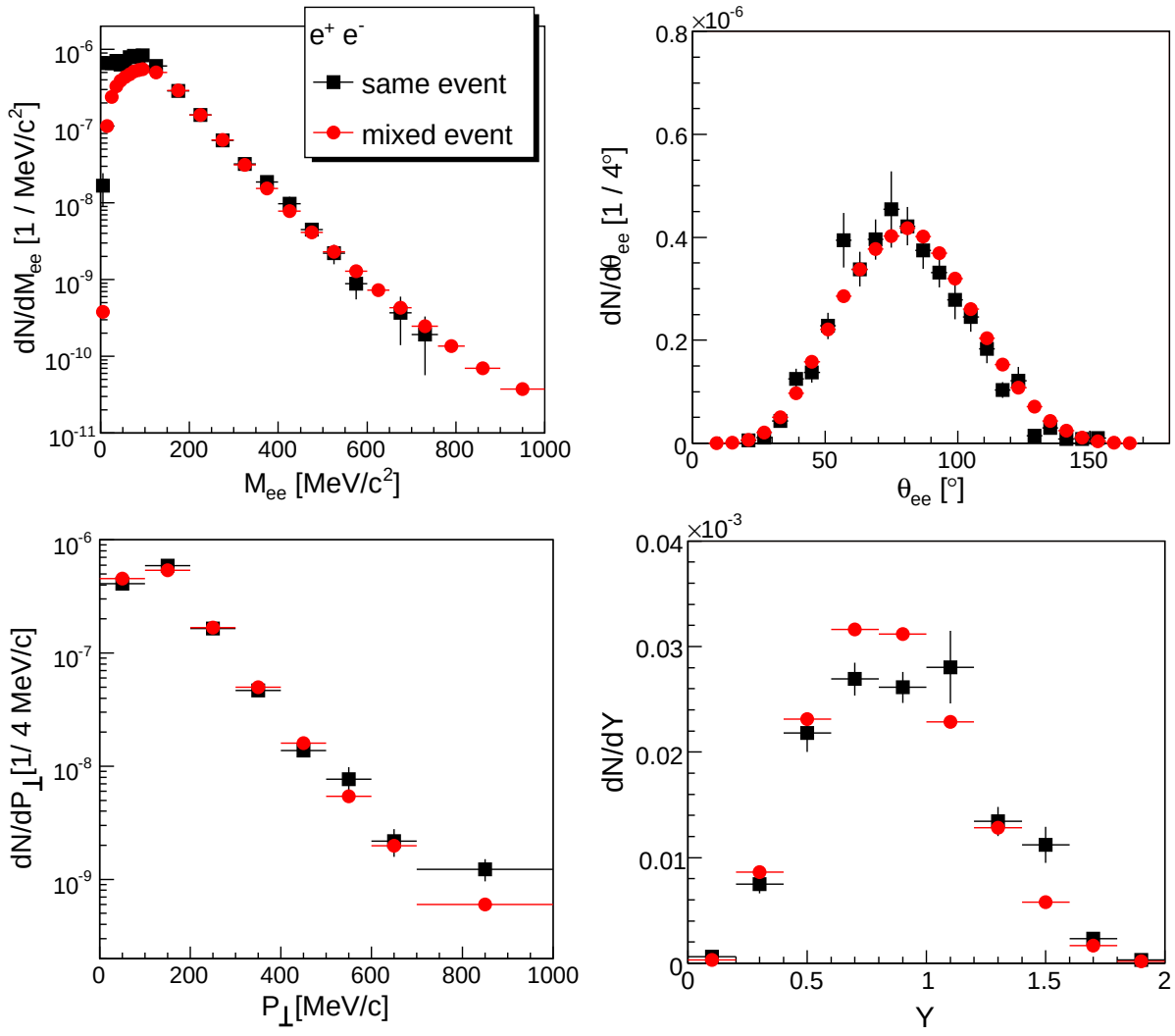

Figure 4.6: Comparison between the experimental like-sign same event (squares) and unlike-sign mixed event (dots) backgrounds.

4.4 Background rejection strategy

The final goal of the pair analysis is to reconstruct the distribution of signal pairs. Since the signal is obtained from a subtraction of background pairs from the total pairs measured, a good signal to background ratio is essential for the quality of the result. Therefore, the analysis strategy described below is based on applying condition on the reconstructed pairs such, as to mainly suppress background pairs but mostly keeping the signal ones.

To motivate a pair selection it is worthwhile to recall some aspects of di-leptonic decays. Lepton pairs can be considered as being decay products of an intermediate virtual photon. Such a state is characterized by its energy and momentum, for which its mass can be computed, which, since it's a virtual photon, can take any positive value independent from each other. In the decay the two leptons go on the mass shell and any excess of energy is converted into relative motion of the two leptons. Hence, if the energy excess is small, the relative momentum is also small. Since most of the states decay with some forward momentum in the laboratory, the momenta of the leptons are boosted and lepton pairs with small relative momentum will appear in laboratory with moderately small opening angle. External pair conversion can also be understood in this context. A photon is scattered off some charge thereby turning into a virtual state which subsequently materializes by decaying into a lepton pair. Since the virtuality is typically very small, also the relative motion of the electron pair is small.

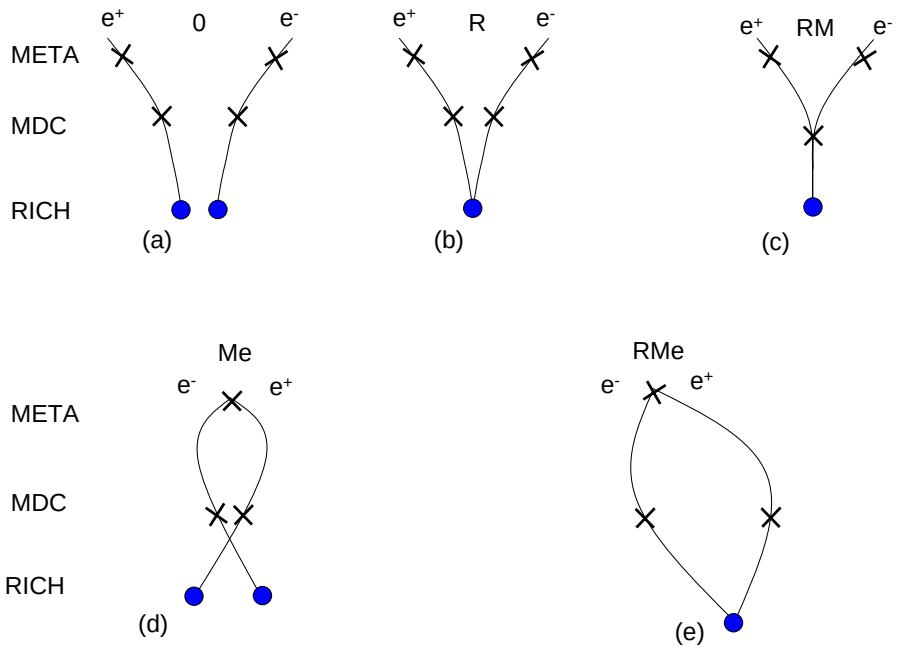

Figure 4.7: Schematic picture of different topology of the e^+e^- pairs indicating the possible double hit configurations: (b) - common hit in RICH, (c) - common hit in RICH and MDC, (d) - common hit in META, (e) common hit in RICH and META

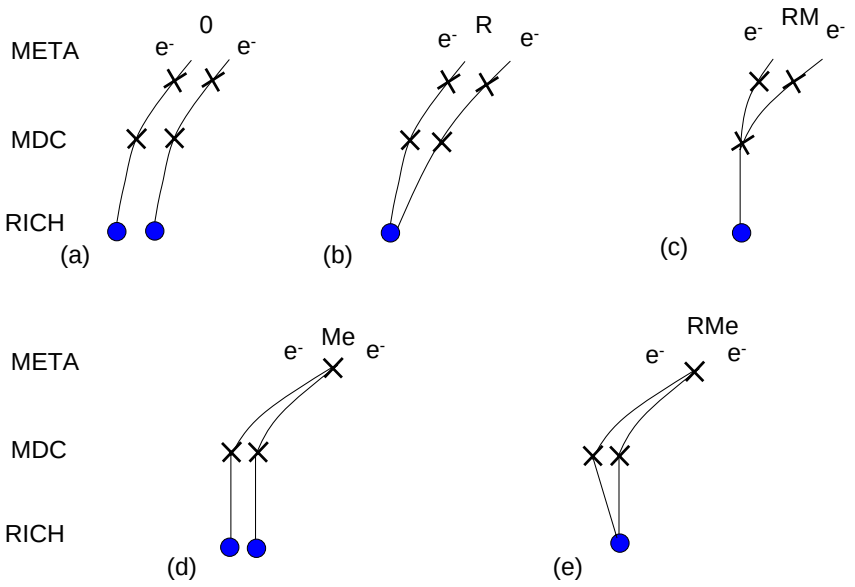

Figure 4.8: Schematic picture of different topology of the e^-e^- pairs indicating the possible double hit configurations: (b) - common hit in RICH, (c) - common hit in RICH and MDC, (d) - common hit in META, (e) common hit in RICH and META

One can classify pairs into two categories (see, Fig. 4.7, 4.8):

- open pairs: two separate rings are identified in the RICH and each ring is matched to a track with an individual META hit (Fig. 4.8 a),
- close pairs: only one ring matched with
  - two track segments, both connected to an own META hit (Fig. 4.8 b),
  - only one track segment, matched with two META hits (Fig. 4.8 c),
  - two track segments with only one META hit (Fig. 4.8 e).

The cuts are motivated by both, the phase space population of various decay pairs, as well as by detector characteristics. Before the cuts are described in details, I will define a terminology:

- *direct* cuts will be referred to as cuts acting on single pairs. In this case such a pair is not counted. However tracks which compose such a pair are still allowed to contribute to other pairs in the event,
- *recursive* cut, in this way we will reject not only this single pair from the sample on which the cut acted on, but also all other pairs which include one of the two tracks of the removed pair. There are two reasons for introducing such strategy:

– A pair, which has been cut by a condition on opening angle, is most likely a true pair coming from γ conversion or π^0 Dalitz decay [87]. Those particles should not be used in any other pair.

– If a pair is built from particle tracks which are sharing the same hit in any of the detectors, one of the tracks is likely to be a fake or misidentified hadron. Therefore these tracks should not be used for pairing anymore. Even if both of them are identified as leptons, one might be a fake.

The recursive way of cutting guaranties high purity of the tracks remaining in the sample, however at the price of a reduced efficiency. Fig. 4.9 shows in the schematic way how the recursive and the direct cuts act on the pair tracks.

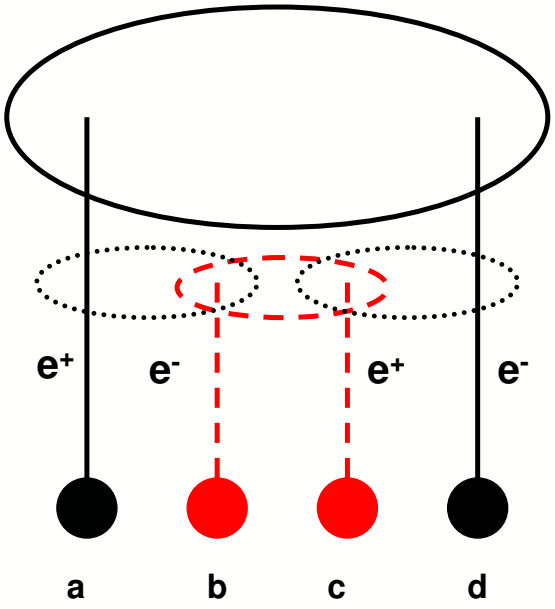

Figure 4.9: Schematic way of the direct and recursive cutting. Single lepton tracks (a), (b), (c) and (d) create all possible unlike-sign pairs inside one event. Let's assume that the pair (b,c) do not fulfill one of the cutting condition. Automatically it will be removed from the sample together with the tracks. In this way also another pairs, such as (a,b) and (c,d) will never contribute to the spectrum. The only pair which will survive the recursive cutting is (a,d). If we would cut in the direct way, also two another pairs would stay in the sample.

In summary, the best strategy to reject contributions from conversion processes and also partly from π^0-Dalitz decays is to cut recursively on the opening angle of the pair. Figure 4.10 shows the opening angle distribution for various simulated sources.

Based on Monte Carlo simulations, an opening angle cut $\theta_{e^+e^-} > 9^o$ has been applied. As one can see, this value also removes contributions from π^0 Dalitz and η Dalitz decays. However this is necessary to suppress the γ conversion pairs which are one of the main sources of combinatorial background.

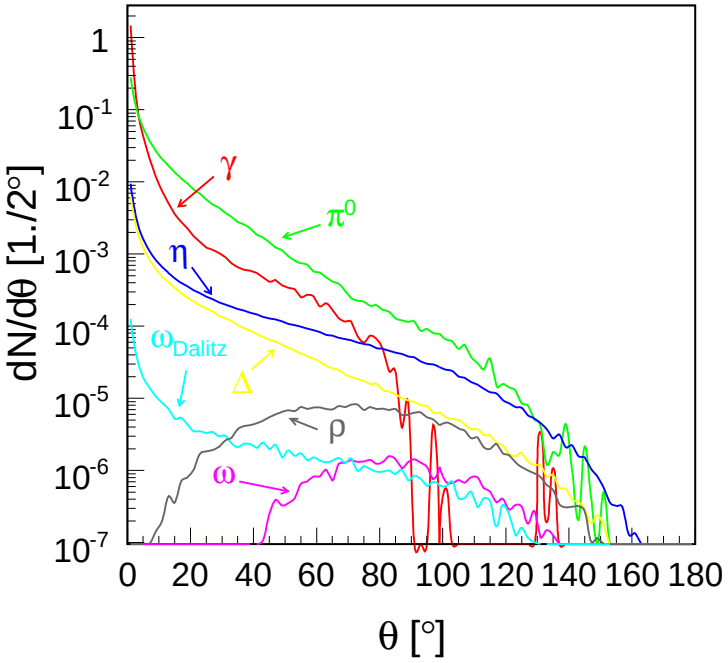

Figure 4.10: Opening angle distribution for various lepton sources.

In addition, on the level of the dilepton analysis two additional cuts were applied:

- *Double-hit rejection*: the two tracks of a pair are not allowed to share a hit in one of the detectors with any other track. Each detector hit should be unique. Fig. 4.11 (a) shows the average multiplicities of the different cases of double hit in the detectors for like-sign and unlike-sign pairs. Most frequent case for e^+e^- pairs is RM (common RICH and MDC hits $\sim$ 62%) and R case (common RICH ring $\sim$ 15%). For the like-sign pairs the most frequent cases are RM (common RICH and MDC hits), RMe (common RICH and META hits) and R case. For both like-sign and unlike-sign pairs, the pairs with separated lepton track (0) are 15 - 24 % of all pairs.

- *Close-pair candidate rejection*: within an angle of 10^o around the track building a pair we search for tracks which have negative χ^2 and have been removed in the earlier step of the analysis. It could happen that one of the legs from the constructed pair is coming from a γ conversion process and the partner has not been properly reconstructed. In such a case, pairs including this track will not be accepted in the pair analysis. Typical distribution of the opening angle of such a case in shown in Fig. 4.11 (b), with the vertical line showing the applied cut value.

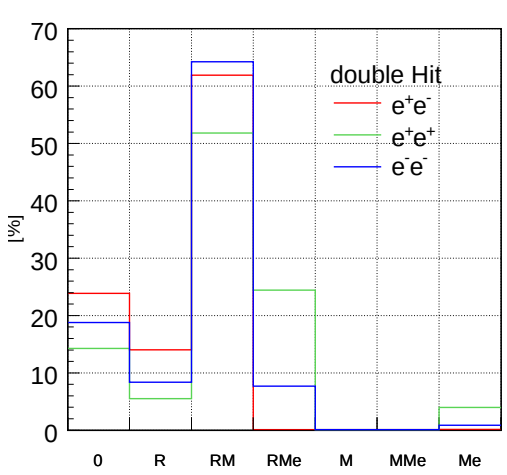

(a) Multiplicity of the pair topologies in measured data for like-sign and unlike-sign pairs. For definition of the various topologies, see 4.8, 4.7.

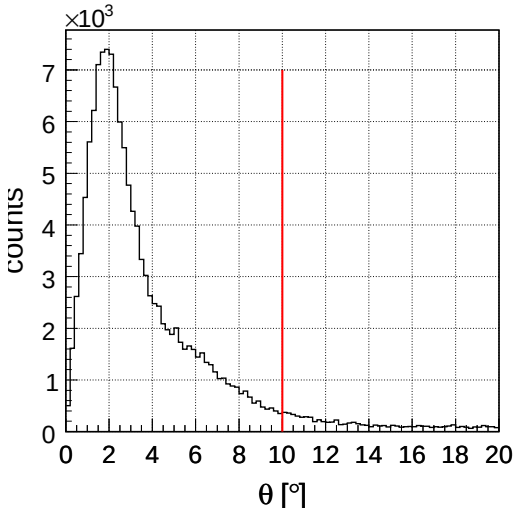

(b) Opening angle between a lepton pair and closest not fitted lepton.

Figure 4.11:

Using information which is available in the Monte Carlo (asking if the pair comes from the same mother particle), one can determine how well the signal (S_{+-}) and the background (CB_{+-} - like-sign same event) are reconstructed in the analysis.

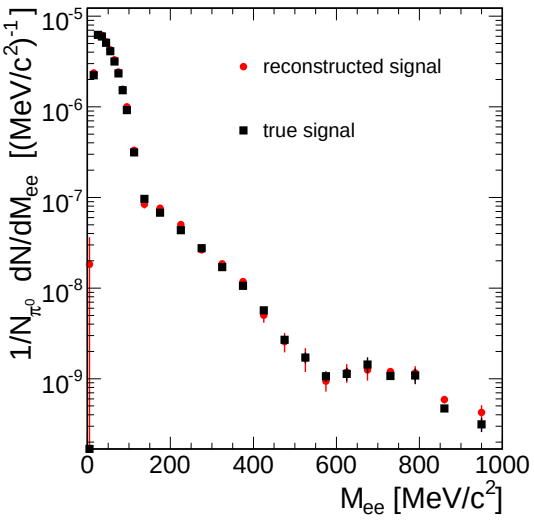

(a) True and reconstructed signal.

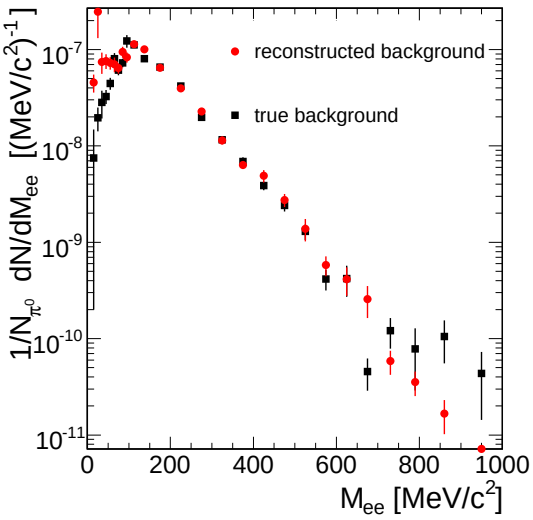

(b) True and reconstructed background.

Figure 4.12: Comparison of the true with reconstructed signal and background in the analysis of simulated events.

Figure 4.12 shows the simulated true (red dots) and reconstructed (black triangles) S_{+-} and CB_{+-} spectra. The reconstructed and the true signal show very good agreement. This is also visible in Fig 4.13 where the purity defined as the ratio of the true signal over the reconstructed one, is shown. One can see that after all cuts have been applied, the purity of the reconstructed pair signal is above 95%. The pair purity is thus much larger than the single lepton purity as was discussed in chapter 3.

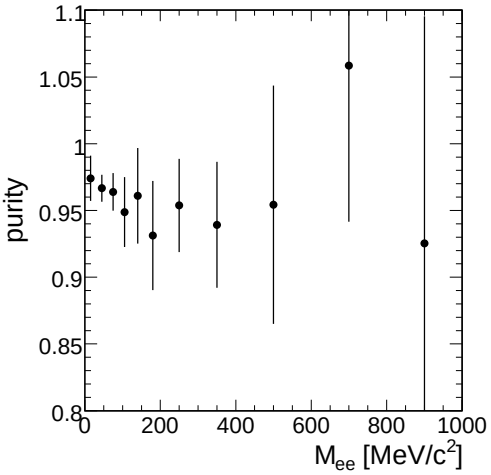

Figure 4.13: Purity of the pair signal as function of the invariant mass.

However, the reconstructed background shows a significant deviation from the true one in the low mass region (M_{ee} < 0.15 GeV/c^2). This can be explained by correlations of like-sign pairs discussed in section 4.2.

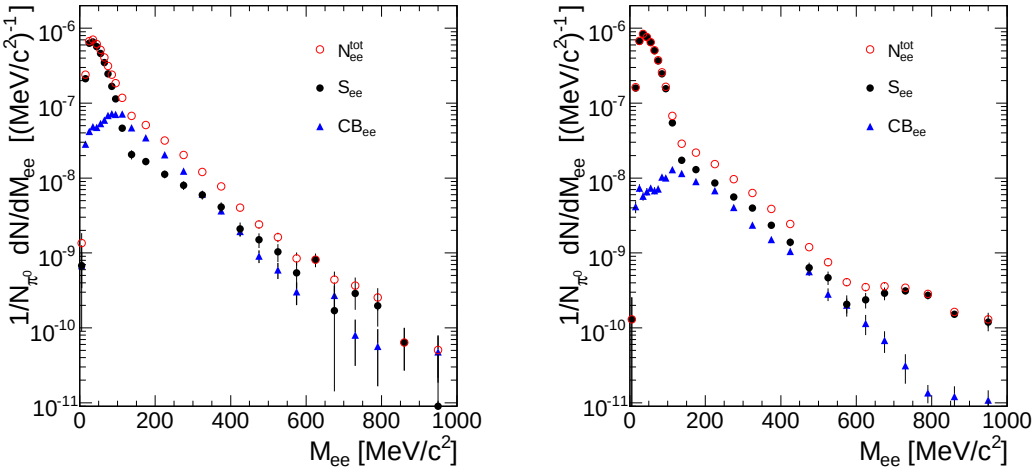

(a) Experiment (b) Simulation

Figure 4.14: Comparison of the uncorrected pair spectra.

On this level of the analysis one can say that the cuts used for the combinatorial background

suppression are under control. This gives us confidence to apply the same analysis procedure for the HADES experimental data.

The resulting spectra of the reconstructed unlike-sign pairs (N_{ee}^{tot}), combinatorial background (CB_{ee}) and signal (S_{ee}) after background subtraction as a function of invariant mass for the simulation and the experiment are shown on Fig. 4.14. The spectra are not yet corrected for detector and reconstruction inefficiency. One can clearly see that after background subtraction the shape of the experimental signal is very similar to the simulated one. For small masses (M_{ee} < 0.15 GeV/c^2) we see a clear feature of the signal coming from π^0 Dalitz decay, followed by a large exponential drop-off towards higher invariant masses.

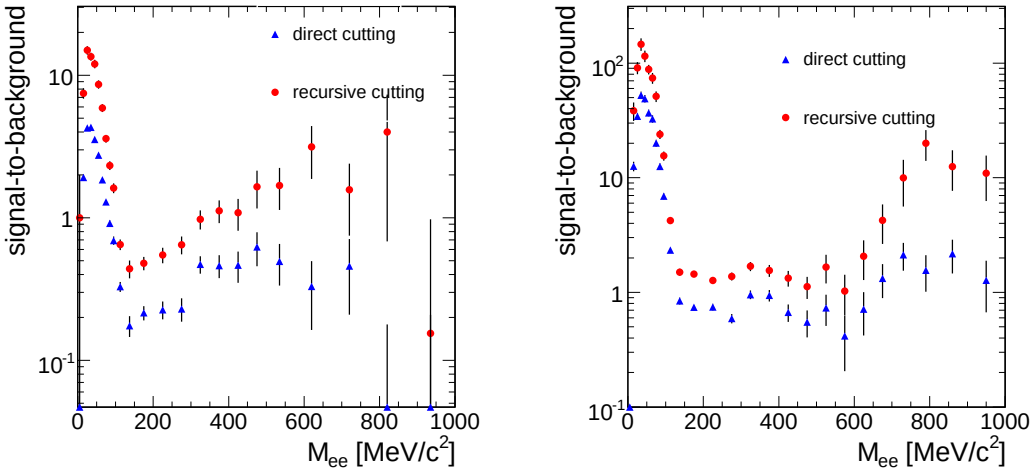

(a) Experiment. (b) Simulation.

Figure 4.15: Signal-to-background ratio as a function of invariant mass.

A very important property of the data is the signal to background ratio (see Fig. 4.15). One can observe for the PLUTO simulation that for the small invariant mass region the signal-to-background ratio is slightly above 100 and in the experiment it is smaller by a factor of 10. Above the π^0 Dalitz region (M_{ee} > 0.15 GeV/c^2) the ratio is dropping below 1 and then again increasing with higher masses. The ratio stays around 1 for the intermediate masses region and above 1 for M_{ee} > 0.6 GeV/c^2. The observed factor of 10 difference in the experimental signal-to-background ratio compared to simulation is caused by the fact, that in the PLUTO simulation only leptons were included. There is no contribution to the combinatorial background coming from misidentified hadrons. It is also important to note that the recursive cutting improved the quality of the data (i.e. the signal-to-background) by a factor 2-3. Despite its slightly lower efficiency, this cutting strategy is therefore preferred. Tables 4.1 and 4.2 show the reduction of the true signal in the PLUTO simulation and the experimental data, respectively. The true signal is displayed separately for each source mother to show which one is mostly affected by the given cut.

For the experiment, all integrals of the signal and background have been investigated in 3 regions of the invariant mass:

- M_{ee} < 0.15 GeV/c^2 (low)
- 0.15 GeV/c^2 < M_{ee} < 0.55 GeV/c^2 (intermediate)
- M_{ee} > 0.55 GeV/c^2 (high)

The following notation for the cut numbers is used in Tables 4.1, 4.2, where cut_n contains cut_{n-1}:

- reference: no cut applied,
- cut1: opening angle 9°,
- cut2: cut1 + double-hit rejection,
- cut3: cut2 + close-pair candidate.

cut_{nr}	π^0_{Dalitz}		$\gamma_{conversion}$		η_{Dalitz}		Δ_{Dalitz}		ω_{Dalitz}	
		[%]		[%]		[%]		[%]		[%]
ref	37800	100	24500	100	1630	100	110	100	2.42	100
1	11100	29	120	0.48	848	52	51.4	51	1.38	57
2	10900	28	118	0.46	838	51	50.7	50	1.37	56

Table 4.1: Reduction of the true signal with the cut number in simulation (cut 3 has no effect in simulation).

One can see that the biggest reduction in the true signal is a result of the opening angle cut (cut1 - $\theta_{ee} > 9^o$). The yield of Dalitz decay is reduced by a factor of 2, while the number of the direct decays of mesons (ρ and ω) stays almost untouched. γ conversion in 99% is removed. Double-hit rejection (cut2) and the close-pair (cut3) do not have a big influence on the signal. The reason for this is the fact that the PLUTO simulation contains only leptons. The opening angle cut reduces it by a factor of 2 for masses up to 0.55 GeV/c^2 and by a factor of 3 in the high invariant mass region.

Analyzing the numbers in Table 4.2 one can see that the background is suppressed by 99%, while the signal is reduced only in the low and intermediate invariant mass region due to the opening angle cut. Figure 4.16 shows the reduction of the total signal and background, in all 3 mass regions as a function of cut number.

	cut_{nr}	M_{ee} < 0.15 GeV/c^2		0.15 < M_{ee} < 0.55 GeV/c^2		M_{ee}> 0.55 GeV/c^2	
		[10^3]	[%]	[10^3]	[%]	[10]	[%]
S_{ee}	ref	26.3	100	2.56	100	6.09	100
	1	21.1	81	1.64	64	5.77	94
	2	22.0	83	1.58	61	5.90	96
	3	22.6	86	1.54	60	5.73	94
CB_{ee}	ref	466	100	11.9	100	30.9	100
	1	13.0	2.8	3.43	28	4.92	15
	2	5.77	1.2	2.96	25	4.19	13
	3	4.64	1.0	2.37	20	3.26	10

Table 4.2: Reduction of the signal and the combinatorial background with the cut number for experimental data.

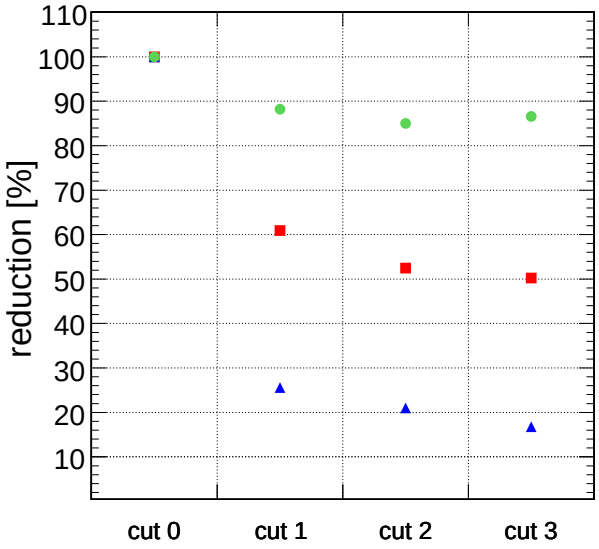

Figure 4.16: Reduction of the experimental signal and background in full invariant mass range (red squares and blue triangles, respectively) as a function of the cut number. In addition, the reduction of the signal above 0.55 GeV/c^2 (green circles) is plotted.

In total 23000 signal pairs have been reconstructed in the present C+C experiment, around 21000 in the π^0 Dalitz region and 2000 above. For any comparison with theoretical predictions, the measured distributions have to be corrected for detector and reconstruction inefficiencies. This will be described in the following subsection.

4.5 Efficiency corrections.

The probability to observe a produced dilepton entering the HADES acceptance is reduced by the HADES detection efficiency and the track reconstruction efficiency. To determine the absolute yield of dileptons, the total yield of unlike-sign pairs has to be corrected with the efficiency. In the analysis we assume, that the pair efficiency can be factorized into single-track efficiency of e^+ and e^-. Therefore, the pair reconstruction efficiency can be expressed in terms of the single-track phase space parameters: θ, φ and laboratory momentum (p).

The single track efficiency is calculated using a full spectrometer simulation. UrQMD is used as an event generator for the C+C collisions. In addition the "white"[1] single leptons are embedded into the Monte Carlo events. Each simulated event is propagated through a full spectrometer response simulation, which determines and applies the spectrometer acceptance. Those events are treated in the same way as the experimental ones. The full event reconstruction analysis (single lepton analysis) is done. In addition the effects of the pair cuts are taken into account, as the pair analysis (under certain conditions) removes single tracks from the sample.

The efficiency is then determined as the ratio of correctly reconstructed test particles to all test particles which were in the geometrical acceptance. Following this strategy, efficiency matrices have been computed with 20 bins in φ, 40 in θ and 80 in momentum. Several self-consistency checks have been performed to be sure that the efficiency is correctly determined (see Appendix 1).

Picture 4.17 shows the efficiency correction for e^- and e^+ averaged over all momenta and sectors.

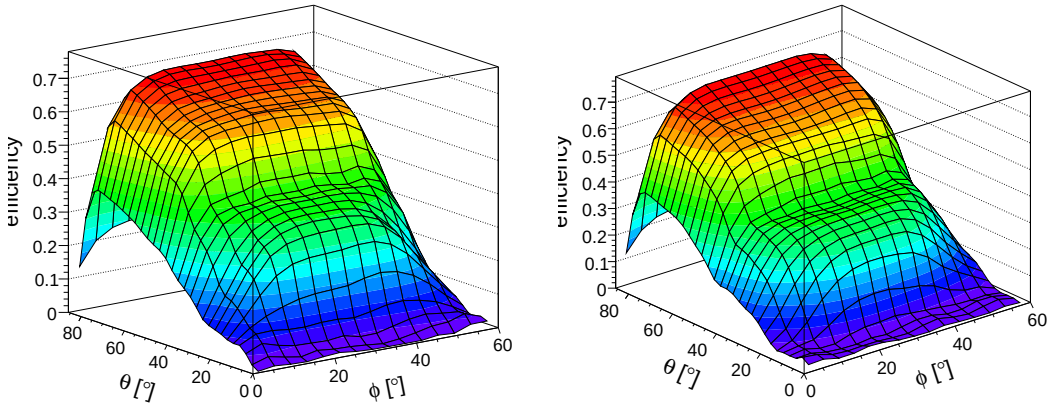

(a) electrons (b) positrons

Figure 4.17: Efficiency corrections for single leptons, averaged over all momenta and sectors.

On average, for low θ angles (θ < 50°) the efficiency is between 30 % - 40 % and for high θ it is around 70 %. The following plots (Fig. 4.18) show the uncorrected and corrected

[1] uniformly distributed in p, θ, ϕ

experimental invariant mass distribution and the ratio of the two distributions to visualize how big the efficiency correction is. From the ratio plot one can see that in the π^0 region it is about factor of 7, and for the high mass region it saturates between 4 and 6, within statistical errors.

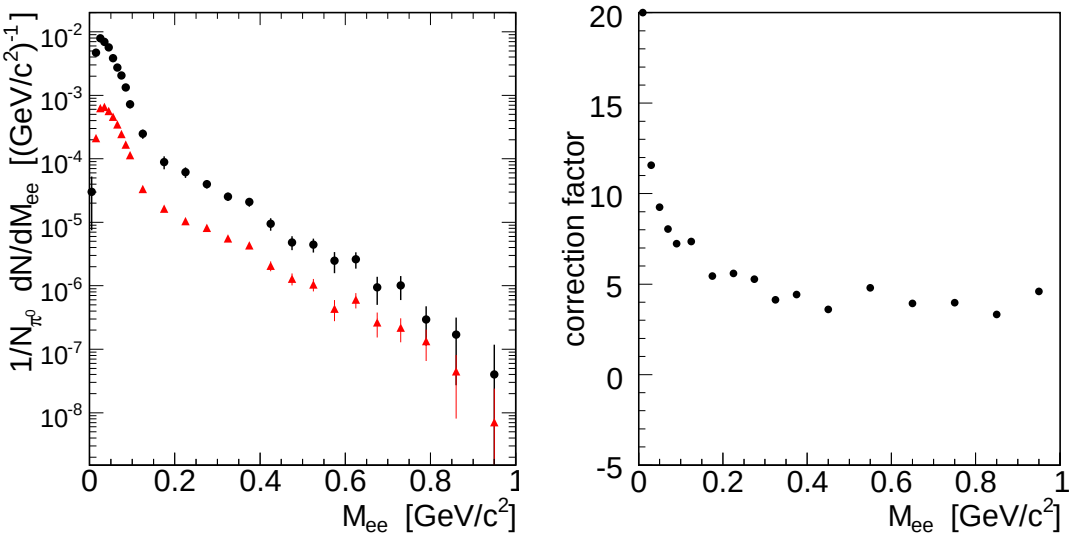

(a) (b)

Figure 4.18: Invariant mass spectrum for the uncorrected (red triangles) and the efficiency corrected spectra (black points) (a) and the ratio (b) of them. The statistical errors of the efficiency matrix are below 1%.

Before making a comparison of the HADES data to theory it is further important to determine the systematic errors the analysis procedure. The way how the systematic errors have been calculated and what the sources of the errors are, is described in the following section.

4.6 Systematic error estimation

The experimental uncertainties are due to both, statistical and systematic errors. The statistical errors are fluctuations in the measured data due to the counting statistics. Systematic errors, by contrast, are reproducible inaccuracies that tend to act consistently in the same direction. Systematic errors are due to our incomplete knowledge of the experimental conditions and analysis procedures.

The three main contributions to the systematics in the data analysis are the uncertainties in the efficiency corrections, in the normalization of the mixed-event (M_{ee} > 0.15 GeV/c^2) background and same-event like-sign (M_{ee} < 0.15 GeV/c^2) background and in the normalization of the dilepton yield with respect to the charged pions yield. These systematic errors coming from the analysis are taken into account. In the calculation the following errors have been established:

- 11% coming from the normalization to the π^0 multiplicity. The systematic error of the hadron analysis is a product of effects of the efficiency/purity corrections, and the extrapolation to 4π, based on UrQMD simulation,
- 10% coming from the CB_{ee} background subtraction. This is deduced from PLUTO + GEANT simulations investigating the ratio of reconstructed and true signal after background subtraction,
- 15% (at maximum) in the π^0 Dalitz region and 10% above originating from the self-consistency checks of the efficiency matrices (see Appendix. B, Fig. B.4).

All systematic errors have been treated as independent (i.e. added quadratically). For the final results the statistical errors and the systematic one have been added quadrature as well.

In the next chapter HADES data corrected for the efficiency will be compared with PLUTO calculations, as well as with various transport models like HSD, RQMD and UrQMD.

4.7 Normalization

The measured electron pair yield is normalized to the number of neutral pions produced in the same event sample (N_π^0):

$$\frac{1}{N_{\pi^0}}\frac{dN}{dM_{ee}} = \frac{1}{N_\pi \cdot \varepsilon_{LVL2}} \cdot \frac{dn}{dM_{ee}} \tag{4.6}$$

where:

- $\frac{dn}{dM_{ee}}$ is the number of measured e^+e^- pairs per mass interval (including efficiency correction),
- ε_{LVL2} is the efficiency of the LVL2 trigger algorithm.

The number of produced π^+ and π^- were deduced from the measured yield and extrapolated to full solid angle, taking into account the measured angular distributions (also found to be in agreement with UrQMD calculations). In the isospin symmetric system $^{12}C+^{12}C$, N_π is in fact expected to be a good measure of the π^0 yield. Table 4.3 shows the mean multiplicities of charged pions in the HADES acceptance. The correction factor to 4π is 1.42 (averaged for π^+ and π^-). The resulting yield of π^0 in 4π per LVL1 trigger event is 1.13. The pion multiplicity per number of participating nucleons M_π/A_{part} = 0.137$\pm$0.015 obtained in our experiment agrees with previous measurements of charged and neutral pions [88, 89] within the quoted errors, see Chapter 4.6.

This way of normalizing the pair spectra compensates to first order the bias caused by the implicit centrality selection of our trigger, as described in Chapter. 2.7.

Particle	π^+		π^-	
	EXP	SIM	EXP	SIM
in HADES acceptance	0.78 ± 0.08	0.78	0.81 ± 0.08	0.82

Table 4.3: Multiplicities of charged pions in the HADES acceptance. Quoted errors are systematical only, statistical ones are negligible.

4.8 Comparison of the HADES data with the PLUTO event generator

With this final result Fig. 4.18 in hand one might now like to ask to what extent the measured yield stems from the early phase of the collision, i.e before the hadronic fireball has frozen out.

Fig.4.19 shows the spectral distribution of electron pairs emitted in the reaction ^{12}C+^{12}C at 2 AGeV. The purpose of dilepton spectroscopy however, is to extract the contribution to the yield which stems from the early phase of the reaction. In this respect, it is important to compare the measured yield to an expectation, assuming that all pairs come from decays of hadrons after the interactions between them have ceased. Therefore, a simulation is carried out assuming that the hadrons populate the phase space like in the case of a thermalized system. It was shown that such an assumption is not too far from reality. This simulation is carried out in the PLUTO software framework [78, 79] (see also Appendix A). The hadronic final state is generated by using measured particle multiplicities and by assuming a thermalized source with a given temperature. Once the final state is generated event-wise by a Monte Carlo technique, hadrons (i.e. π^0,η) are decaying according to their free partial decay widths. Thereafter, the remaining electron and positron tracks are filtered with the HADES acceptance.

First we compare our experimental results with a pair cocktail (cocktail A) calculated from free π^0, η and ω meson decays. This cocktail represents these contributions emitted after the chemical freeze-out of the fireball. π^0 and η are particles with long lifetime and their yields have been measured in photonic decay channel (TAPS [88]), in case of π^0 it can be deduced from the yield of their charged state ($\pi^{\pm}$).

The π^0 multiplicity has been obtained by the analysis of the charged pions in the HADES spectrometer. The η multiplicity is taken from a measurement of the TAPS collaboration in the two-gamma decay channel [88, 90]. Due to uncertainties in the extrapolation of the measured data to the full phase space, the multiplicity has a systematic uncertainty of about 20$\%$. The production rates of the light vector meson ω are not known experimentally. Nevertheless we attempted to include vector meson production in our thermal model using the m_T scaling method [37].

Cocktail A is clearly not sufficient to explain the HADES dilepton yield at intermediate, as well as for the high masses (see Fig. 4.19). For masses below 0.14 GeV/c^2 one can observe very good agreement between PLUTO and the experimental dilepton yield, as expected from the way, the spectra are normalized (assuming, that no other source has a big contribution in

this region). However, in the η region, a factor of around 2 in yield is missing and therefore requires additional sources. Indeed, such contributions are expected from the decay of short-lived resonances, mainly from the Δ (1232) and the ρ, excited in the early phase of the collision. The di-electron pair production from the Δ resonance in the elementary collisions is not measured up to now. To include in the PLUTO cocktail pairs from $\Delta^{0(+)}$ -> Ne^+e^- decays, we assume that the Δ yield scales linearly with the π^0 yield. For the ρ meson, a similar assumption as for the ω meson was made. For the broad ρ meson (Γ = 150 MeV) this result in the spectral function is visible in Fig. 4.20. The full thermal cocktail (B) is shown in Fig. 4.20 as a long dashed line.

As it was expected, in the mass region above M_{ee} > 0.15 GeV/c^2 the yield has increased. However the data are not reproduced by PLUTO, but rather stay well below the data up to 0.7 GeV/c^2, where the main expected contributions are the two-body vector meson decays.

Transverse momentum and rapidity are additional observables, besides the mass, that can be used to discriminate different models, especially for intermediate and high masses. In addition, in the low mass region where agreement with the models is trivial (by normalization to π^0), such a comparison gives a further consistency check of the analysis procedures. Fig. 4.21 shows the rapidity distributions of the experimentally reconstructed di-electron pairs in comparison with the PLUTO cocktail. The obtained spectra, as it was expected, are centered around Y=0.9, due to the symmetry of the system (^{12}C+^{12}C). The small asymmetry is due to the HADES acceptance. For the invariant masses M_{ee} < 0.15 GeV/c^2, where the main contribution comes from the π^0 Dalitz decay, the rapidity distribution shows excellent agreement between the experimental and simulated data. In the region between 0.15 GeV/c^2 < M_{ee} < 0.55 GeV/c^2 the rapidity distribution reflects the trend observed in the invariant-mass spectra: a surplus of the data over the simulation, mostly for the middle and forward rapidity. For even higher masses, the surplus of the data is visible in the full rapidity range. Fig. 4.22 shows a comparison

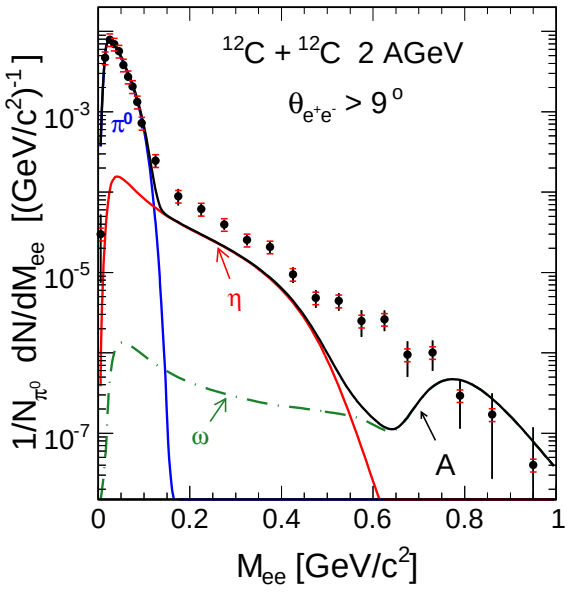

Figure 4.19: Comparison of the HADES dilepton mass spectrum to the PLUTO cocktail calculation, only for π^0, η and ω decays.

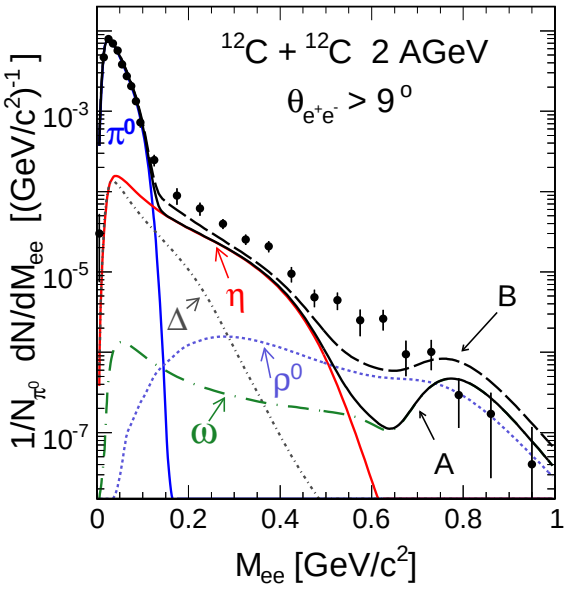

Figure 4.20: Comparison of the HADES data to the full PLUTO cocktail including Δ and ρ decays.

between the experimental and simulated distributions of the transverse momentum ($P_\perp$). As it was observed in the case of the invariant mass, as well as for the rapidity distribution (Fig. 4.20, 4.21) for the low-mass region we have good agreement between the experimental data and the cocktail. For the intermediate-mass region (150 MeV/c^2 < M < 550 MeV/c^2) the excess is not dependent on the transverse momentum of the pair. It is constant in the full $P_\perp$ region.

Table 4.4 shows the integrated yields of the experimental and simulated signal spectra (after background subtraction) for the three mass regions.

	M_{ee} < 150 MeV/c^2		$150MeV/c^2 < M_{ee} < 550MeV/c^2$		$M_{ee} > 550MeV/c^2$	
	EXP	SIM	EXP	SIM	EXP	SIM
	$[10^{-4}]$	$[10^{-4}]$	$[10^{-5}]$	$[10^{-5}]$	$[10^{-7}]$	$[10^{-7}]$
$P_\perp$	4.34 $\pm$ 0.08	3.91	1.45 $\pm$ 0.65	0.69	4.91 $\pm$ 0.84	1.75
Y	4.44 $\pm$ 0,08	3.91	1.51 $\pm$ 0.16	0.69	5.54 $\pm$ 0.86	1.75

Table 4.4: Transverse momentum ($P_\perp$) and rapidity (Y) integrated yields, for three regions in invariant mass (M_{ee}).

Within statistical errors the integrals in case of P_T and Y are equal, for the different mass regions. It is also visible that in the intermediate mass region the simulation is lower by a factor of around 2 in comparison to the experiment.

One should, however, emphasize that effects related to the in-medium propagation of broad resonances, related off-shell effects and multi-step processes, which play a crucial role at this energy, are not included in the PLUTO model. The main conclusions of the comparison to the thermal model is that this relatively simple-minded model is not able to explain our dilepton yields fully. It is necessary to make a comparison with more advanced transport models. In the

next chapter we would like to concentrate on the comparison of the HADES data with several transport models available at the moment, namely HSD, RQMD, UrQMD.

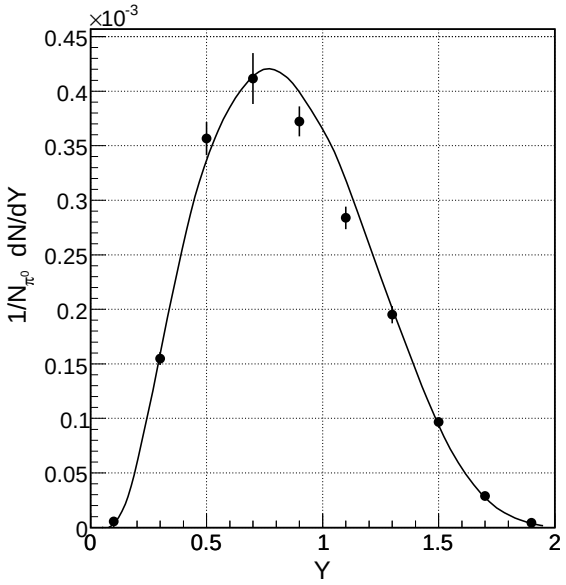

(a) M_{ee} < 0.15 GeV/c^2

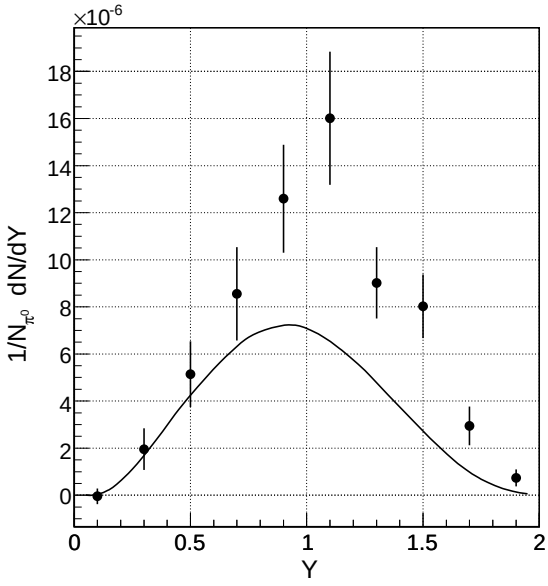

(b) 0.15 GeV/c^2 < M_{ee} < 0.55 GeV/c^2

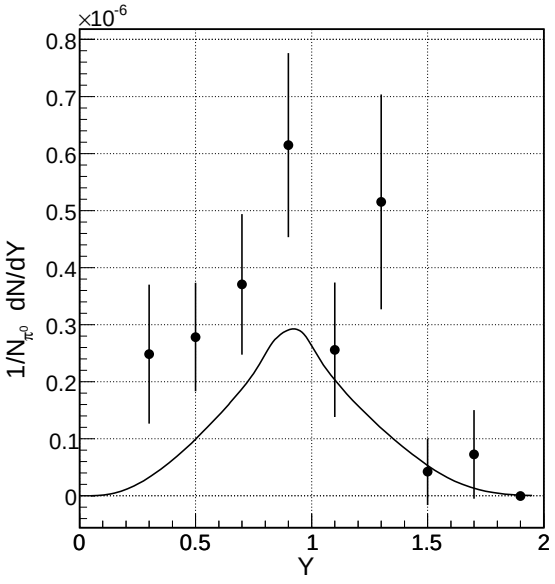

(c) M_{ee} > 0.55 GeV/c^2

Figure 4.21: Comparison of the rapidity distribution between the experimental data and the PLUTO simulation for a three regions in invariant mass.

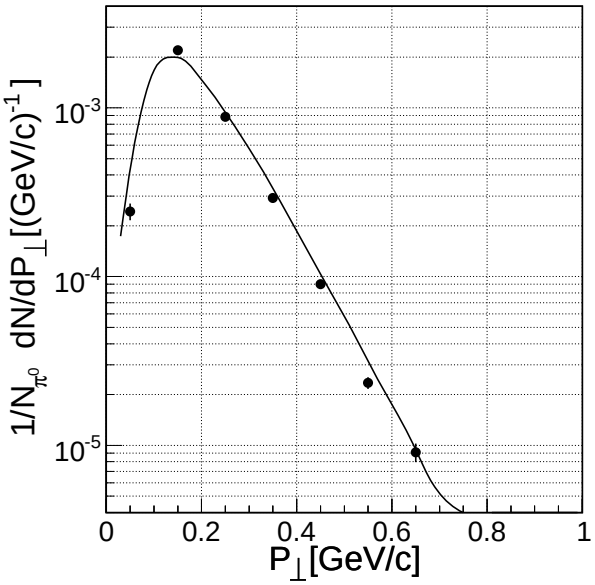

(a) M_{ee} < 0.15 GeV/c^2

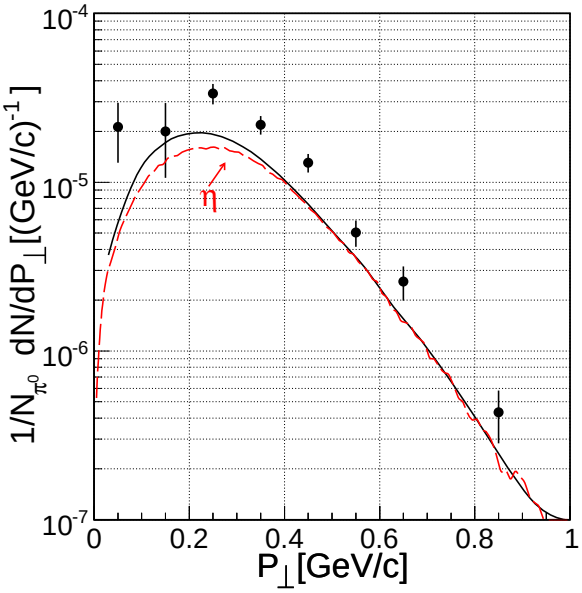

(b) 0.15 GeV/c^2 < M_{ee} < 0.55 GeV/c^2

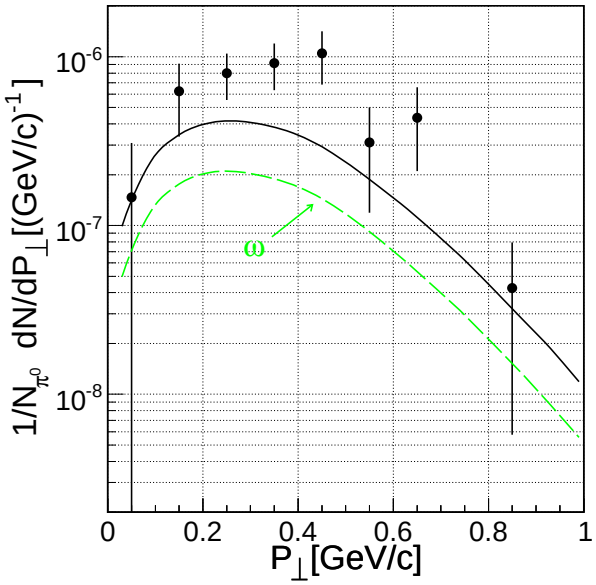

(c) M_{ee} > 0.55 GeV/c^2

Figure 4.22: Comparison of the HADES data (points) to the PLUTO cocktail (curves) as a function of $P_\perp$ for three regions in invariant mass (M_{ee}. Also shown are the simulated $P_\perp$ for η and ω in the corresponding mass region (dashed lines).

Chapter 5

Physics results and discussion.

In section 4.8, it was demonstrated that the hadronic cocktail based on a simple thermal model assumption is not enough to explain the observed dielectron yields, as well in the intermediate, as in the high-mass regions. This finding is an indication of additional sources contributing to the experimentally observed yield, as e.g. the Bremsstrahlung and the decay of short-lived resonances. A theoretical calculation of such a complete cocktail requires a fully microscopic treatment of the collision process.

5.1 Comparison of the HADES data with transport models.

A large effort has been made by theoretical groups (e.g. HSD [37], UrQMD [91, 73, 92, 93], RQMD [94]) to investigate the in-medium properties of the vector mesons based on microscopic transport model. As it was mentioned before, the light vector mesons are short-lived particles. Their life-times are $\tau \simeq 1.3$ fm/c for the ρ meson and $\tau \simeq 24$ fm/c for the ω. The lifetime of the ρ meson is significantly smaller then the lifetime of the fireball ($\tau \simeq 10$ fm/c). Hence, a ρ meson being produced in an early stage of the heavy-ion collision, decays likely inside the fireball volume, making it most sensitive to in-medium effects.

To evaluate how well available transport models reproduce "trivial" (known) sources, in the first step again only the π^0 and η calculation will be compared with the experimental data. Fig. 5.1 shows the comparison of the HADES data with theoretical calculations (HSD, RQMD, UrQMD) of the contributions from π^0 and η. In addition, the contribution from our thermal model (PLUTO) is superimposed, to show that the simple model is not so far away from the more advanced transport calculations. The generated theoretical cocktails have been filtered with the HADES acceptance, smeared according to the HADES momentum resolution and normalized to the respective π^0 multiplicities, obtained in the calculations.

As one can see, the agreement for the π^0 Dalitz between all models is quite good. For the η Dalitz they still agree within 20 $\%$, indicating that these models treat η production differently. The PLUTO event generator, constrained by data only, gives very similar results too.

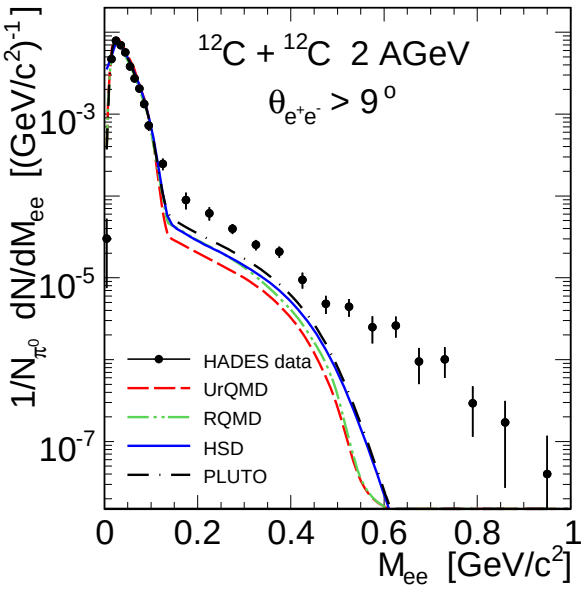

Figure 5.1: Experimental efficiency corrected data compared to transport model cocktails composed of free π^0 and η decays.

Fig. 5.2 shows a comparison of the experimental invariant-mass spectrum with full vacuum calculations of the transport models. First, in the low invariant mass region all calculations show agreement with the experimental data. Furthermore, at masses $0.15 < M_{ee} < 0.55$ GeV/c^2 all calculations slightly undershoot the intermediate mass region and show too much yield at masses $M_{ee} > 0.65$ GeV/c^2.

For the full comparison with the theory, as an example, the comparison between data and the HSD calculation for the $P_\perp$ and Y is shown in Fig. 5.3 and Fig. 5.4, respectively. The comparison is done for 3 bins of invariant mass.

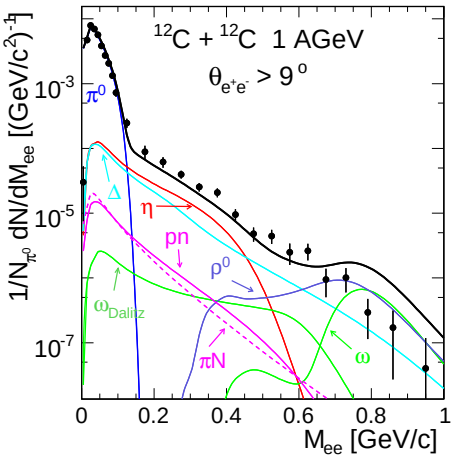

(a) HSD

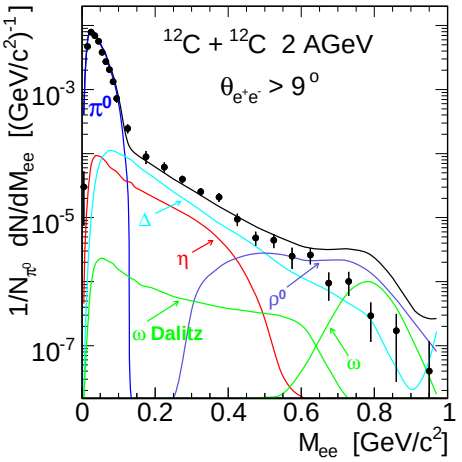

(c) UrQMD

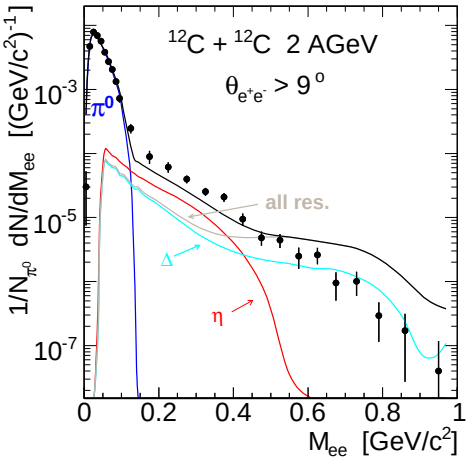

(b) RQMD [95]

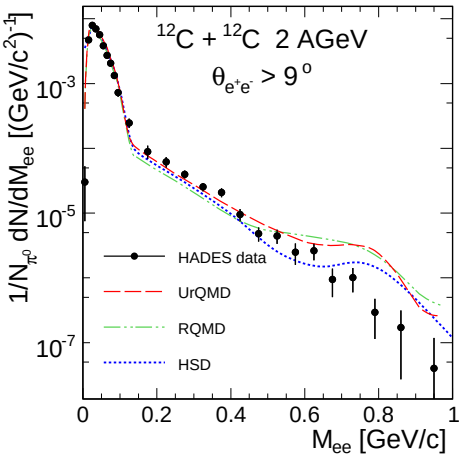

(d) HSD, RQMD, UrQMD

Figure 5.2: Comparison of the efficiency corrected HADES data with the vacuum calculation on the HSD (a), RQMD (b) and UrQMD (c) transport models.

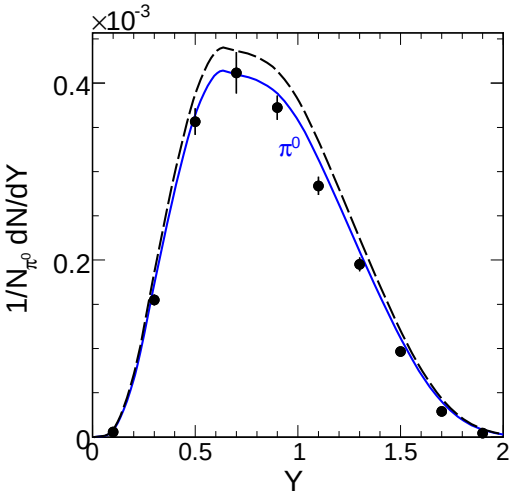

(a) M_{ee} < 0.15 GeV/c^2

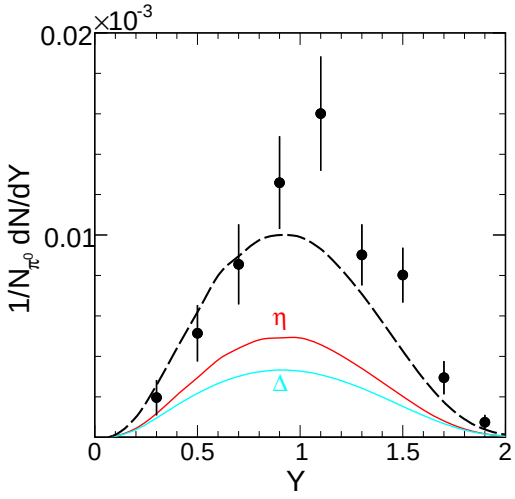

(b) 0.15 GeV/c^2 < M_{ee} < 0.55 GeV/c^2

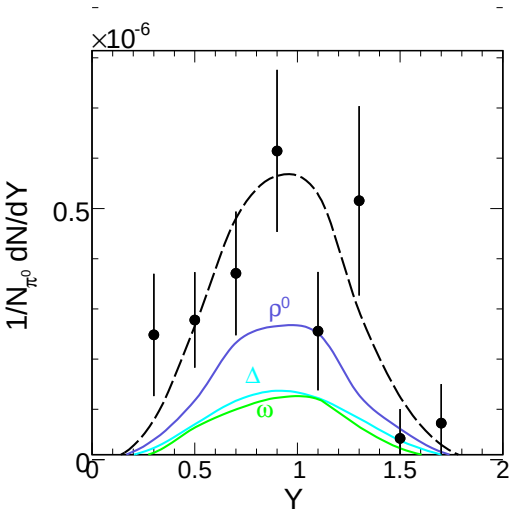

(c) M_{ee} > 0.55 GeV/c^2

Figure 5.3: Comparison of the rapidity distribution between experimental data and transport model calculation (HSD) for three bins in invariant mass.

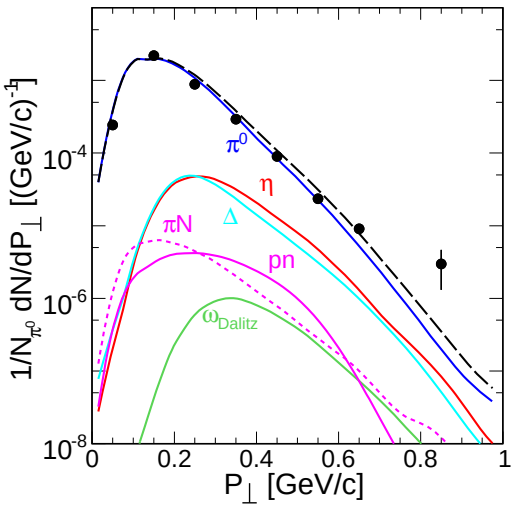

(a) M_{ee} < 0.15 GeV/c^2

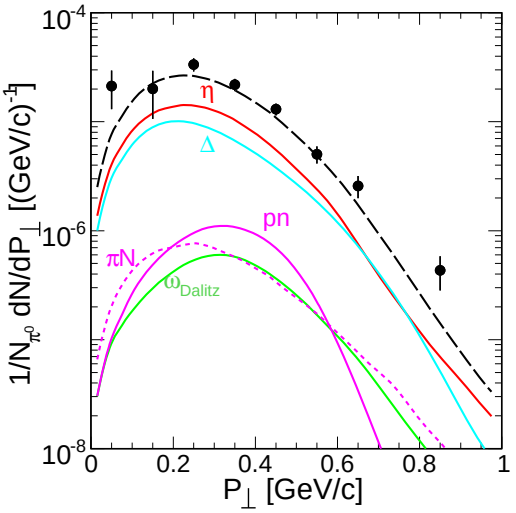

(b) 0.15 GeV/c^2 < M_{ee} < 0.55 GeV/c^2

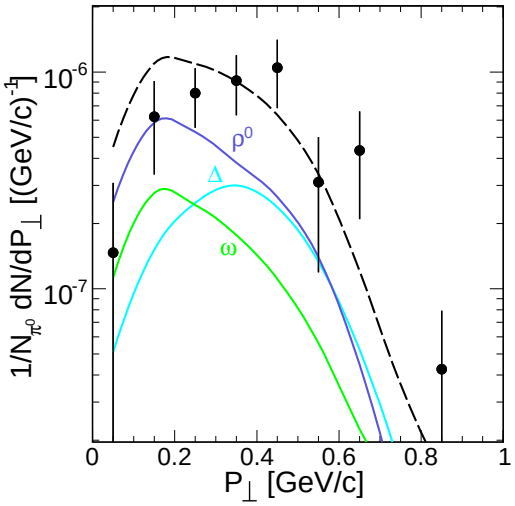

(c) M_{ee} > 0.55 GeV/c^2

Figure 5.4: Comparison of the transverse momentum distribution between experimental data and transport model calculation (HSD) for three bins in invariant mass.

Furthermore, the excess of the experimental yield can be quantified relative to the invariant mass distributions from simulation taking into account cocktail A (π^0, η and ω) only, shown in Fig. 4.19 as a solid line. Fig.5.5 shows the ratio obtained in this way as a function of invariant mass.

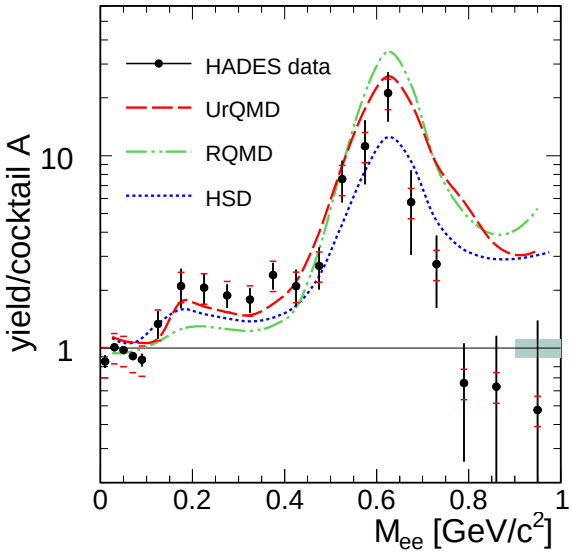

Figure 5.5: Ratio of the experimental data and transport model calculations to PLUTO cocktail A [96]. Statistical and systematical errors of the measurement are shown as vertical and horizontal lines, respectively. In addition the data have an overall normalization error of 11 %.

As it is expected from the normalization (and shown before), in the invariant mass region $M_{ee} < 0.15$ GeV/c^2, where the main contribution comes from the π^0 Dalitz decay and in smaller amount from η and Δ Dalitz, the ratio is close to 1. At higher masses ($M_{ee} \sim 0.6$ GeV/c^2) the ratio of the data and PLUTO cocktail A develops a pronounced maximum mainly due to the lack of ρ decay in the reference cocktail A. Especially the mass region between the η and the ω pole is expected to be dominated by the thermally populated low-mass tail of the ρ resonance. PLUTO cocktail B (Fig. 4.20), which includes Δ and ρ decays, shows indeed more yield, but still does not account for all of the observed pair yield. All transport models qualitatively reproduce the trend shown by the data around 0.6 GeV/c^2, but differ substantially in the amplitude. And at even higher masses all models consistently overshoot the pair yield. Summarizing, one can say that the vacuum calculations are not enough to explain the measured experimental yields. It is necessary to compare HADES data with in-medium calculations, which are presently provided by two of the available transport models. Fig. 5.6 shows a comparison of the experimental data with these theoretical calculations, which include in-medium modifications of the spectral functions.

In case of RQMD [95] the following in-medium effects are included into the calculations:

- extended VDM for ρ and ω decays [94] ,
- decoherence effects [95],
- dropping mass scenario (Brown-Rho scaling [12, 25]).

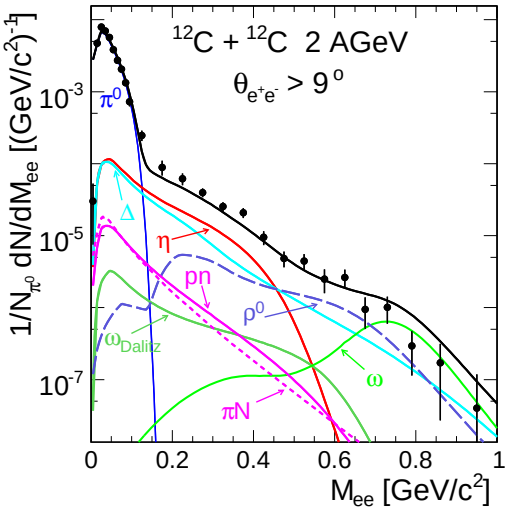

(a) HSD

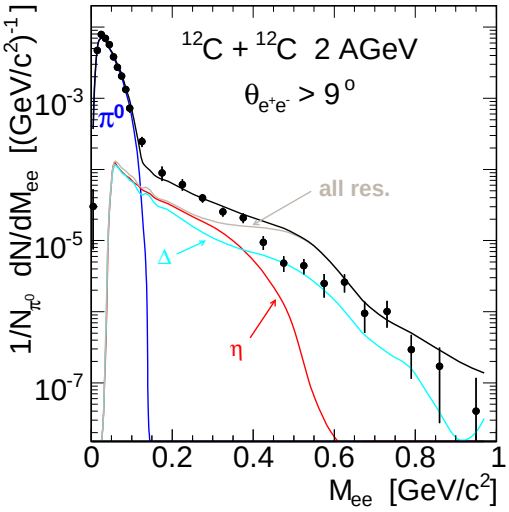

(b) RQMD

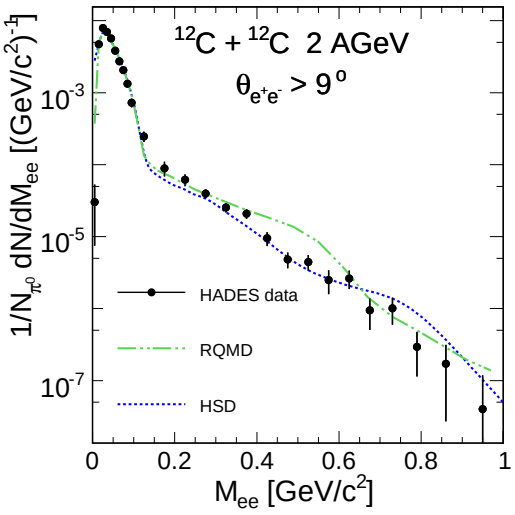

(c)

Figure 5.6: Comparison of the efficiency corrected HADES data with the in-medium calculations of the HSD (a), RQMD (b) transport models and both transport model calculation (c).

In the HSD calculations, the following in-medium effects were included:

- modeling of the spectral function of the vector mesons:
  - collisional broadening,
  - dropping mass scenario,
- off-shell propagation of dynamical spectra functions [97].

For a better understanding of the modifications of the invariant mass spectrum due to the in-medium effects with respect to the vacuum one, the vacuum and in-medium results for the HSD and RQMD are presented in Fig. 5.7 together with the HADES data.

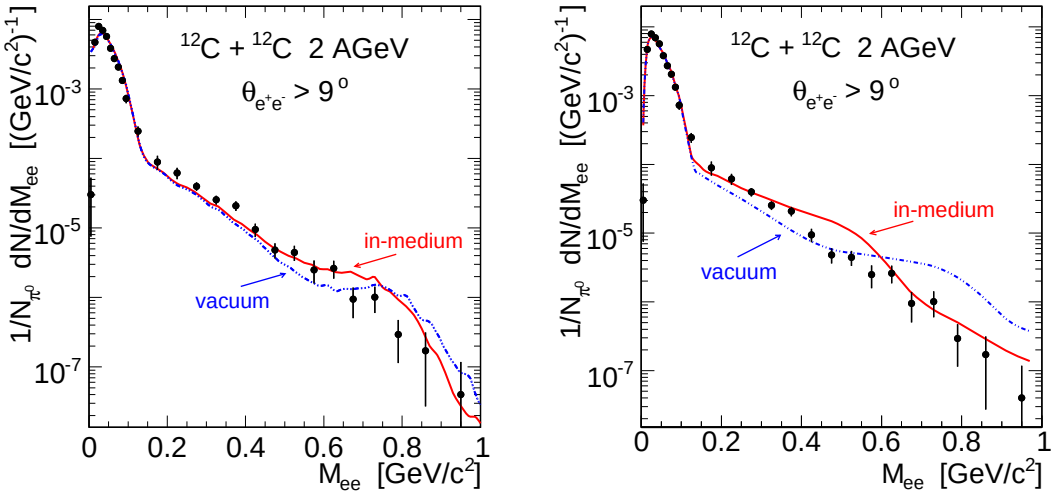

(a) HSD (b) RQMD

Figure 5.7: Comparison of the HADES data with vacuum (dashed line) and in-medium (solid line) full cocktail of HSD and RQMD transport models.

As a result in case of the RQMD one can observe a shift of the strength of the ρ meson towards smaller masses, giving better agreement in the high invariant-mass region (M_{ee} > 0.6 GeV/c^2), however for the masses below the model overestimates the data. Whereas for the HSD calculations, the broadening and shifting-mass scenario of the vector mesons clearly fills the gap between 0.4 - 0.6 GeV.c^2 and gives a better agreement with the experimental data.

None of the presented calculations are presently able to explain the experimental data over the full invariant mass region.

5.2 The DLS recall

On this level of analysis it is also interesting to compare our results with the measurement performed in the 80, 90's by the DLS collaboration at a beam energy of 1.04 AGeV [36]. In

both data sets one can determine the e^+e^- excess relative to the η Dalitz yield in the mass range of 0.15 - 0.55 GeV/c^2 and thus study its dependence on bombarding-energy. It has been assumed, that the HADES and DLS spectrometers provide a similar acceptance for the dilepton excess and the η Dalitz decay.

The DLS data and an appropriately filtered PLUTO cocktail generated for the beam energy of 1.04 AGeV, are shown in Fig. 5.8 (left panel) together with the HADES data at 2.0 AGeV (right panel).

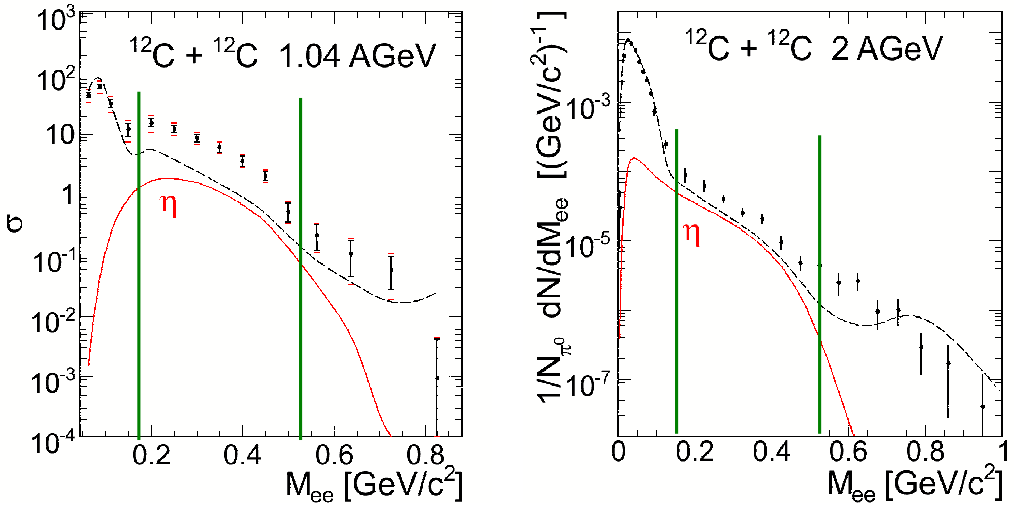

(a) DLS: C+C at 1.04 AGeV (b) HADES: C+C at 2 AGeV

Figure 5.8: Comparison of the experimental results with the η contribution.

Let us define the enhancement factor F(E) above the η component dependent on the beam energy E in the following way:

$$F(E) = \frac{Y_{tot}(E)}{Y_\eta(E)} = \frac{Y_\eta(E) + Y_{exc}(E)}{Y_\eta(E)} \tag{5.1}$$

$$\Rightarrow \frac{Y_{exc}(E)}{Y_\eta(E)} = F(E) - 1 \tag{5.2}$$

$$\Rightarrow Y_{exc}(E) = \frac{F(E) - 1}{Y_\eta(E)} \tag{5.3}$$

where Y_η(E) is the yield of the η component and Y_{tot}(E) is the yield of the experimental signal, in the intermediate mass region (0.15 < M_{ee} < 0.55 GeV/c^2), as indicated by the vertical lines (Fig. 5.8). The Y_{tot}(E) can be understood as the sum of the yield coming from the η Dalitz decay and other sources, which contribute to this region (Y_{tot}(E) = Y_η(E)+Y_{exc}(E)).

According to Eq. 5.3 one can has the following:

$$\frac{Y_{exc}(2.0)}{Y_{exc}(1.04)} = \frac{F(2.0)-1}{Y_{\eta}(2.0)} \cdot \frac{Y_{\eta}(1.04)}{F(1.04)-1} \tag{5.4}$$

$$\Rightarrow \frac{F(2.0)-1}{F(1.04)-1} \cdot \frac{Y_{\eta}(1.04)}{Y_{\eta}(2.0)} \tag{5.5}$$

System	Beam energy	F(E)	stat. error (%)	sys. error (%)
C+C	1.04 AGeV	6.5	$\pm$ 0.48 (7.4)	$\pm$ 2.1 (32)
C+C	2.0 AGeV	2.07	$\pm$ 0.21 (8.6)	$\pm$ 0.38 (19)

Table 5.1: Derived enhancement factor for the DLS and HADES measurements.

Knowing, from the TAPS [88, 90] measurements, that going from 1.04 to 2.0 AGeV beam energy the inclusive η production in C+C collision will increase by a factor 13 $\pm$ 3 (see, Fig. 5.9) and factor F(E) (see, Tab. 5.1). The energy scaling factor of the excess pair yields:

$$\frac{Y_{exc}(2.0)}{Y_{exc}(1.04)} = 2.5 \pm 0.5(stat) \pm 1.5(sys) \tag{5.6}$$

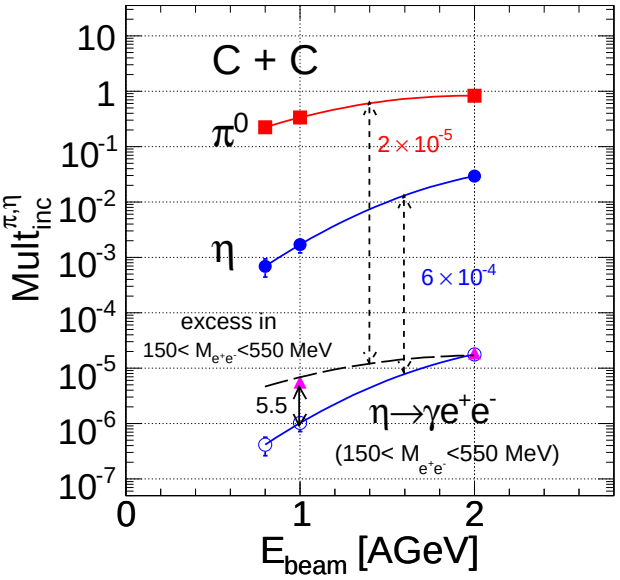

Figure 5.9: Excess dielectron multiplicity in the pair mass range of 0.15 - 0.55 GeV/c^2 (triangles) extracted from HADES data versus the beam energy. Also shown are excitation functions of inclusive η (blue) and π^0 (red) production taken from literature [88, 90]

This energy scaling of the excess yield is very close to the known scaling of pion production found by TAPS, i.e:

$$\frac{Y_\pi(2.0)}{Y_\pi(1.04)} = 2.3 \pm 0.3(stat) \tag{5.7}$$

It suggests that the pair excess is indeed driven by pion dynamics, involving e.g. Δ and ρ excitations. This finding is illustrated in Fig. 5.9, which shows the energy scaling of the excess yield together with the behavior of the η and π. It is clearly apparent that the excess scales like pion production, rather than like η production.

Thus the 'solution' of the DLS puzzle is the presents of a source of e^+e^- which so far was not accounted for. This source has the same beam energy dependence as pion production.

Chapter 6

Conclusions

One of the fundamental question that can be addressed in heavy-ion experiments is the role of chiral symmetry breaking in the formation of hadrons. According to this scenario , the otherwise light bare quarks with a mass of few MeV/c^2, dynamically acquire a "constituent" quark mass of $\sim$ 300 MeV/c^2 by coupling to QCD condensates. This generation of mass should also have an influence on the mass of the hadrons formed by those quarks. As demonstrated by model calculation, the QCD condensate should eventually melt when the temperature and/or density of nuclear matter formed in a heavy ion collision goes up.

As a consequence the mass of vector mesons such as ρ, ω, ϕ should also drop in the same medium. In order to investigate the behavior of the mass of vector mesons, one can study dilepton decays of mesonic states.

This thesis presents the final results of the HADES measurement of di-electron pair production in 2 AGeV C+C collisions, which was performed in the year 2002 and the result published ar 2006 [96].

The thesis presents a detailed description of the analysis strategy. Final experimental distributions of invariant mass, transverse momentum and rapidity have been compared with the PLUTO event generator and with more advanced theoretical calculations. Due to the limited mass resolution (10 % in the ω pole region) and the limited experimental statistics beyond $\sim$ 500 MeV/c^2 the longer-lived vector mesons (ω, ϕ) could not be resolved.

The comparison with theoretical calculations shows that the observed di-electron yield cannot be fully explained. Vacuum calculations in the invariant mass region, where the dominant source is the π^0 Dalitz decay show very good agreement with the experimental data. However in the intermediate mass region, the data show an excess above the theoretical calculations. For even higher masses (M_{ee} > 0.6 GeV/c^2) the theoretical calculations overshoot the data. After including medium modification of the spectral functions, better agreement in the high mass region is observed. For the intermediate mass region, the theoretical calculations are much closer to the data, but do still not fully reproduce the experimental yield.

Another result presented in this work is the energy scaling of the experimental yield above

the η component. Based on the known production and decay rates of the η meson, it has been shown that the observed excess in the mass region between 0.15 < M_{ee} < 0.55 GeV/c^2 is consistent with the yield observed by the DLS collaboration if one assumes an excess yield scaling like pion production. It suggests that the pair excess is driven by pion dynamics, involving Baryon resonance excitations. However a direct comparison with the DLS data will become possible only once the analysis of the HADES data from C+C at 1AGeV beam energy is available.

Very recently, it has been realized, that in the former calculations of the HSD transport model (so called photon soft approximation) proton-neutron bremsstrahlung was underestimated by almost a factor of 4 in comparison to new One Boson Exchange Model calculations performed by B. Kaempfer and L. P. Kaptari [98]. Fig. 6.1 shows the invariant mass spectra of the HADES data with corrected HSD calculations.

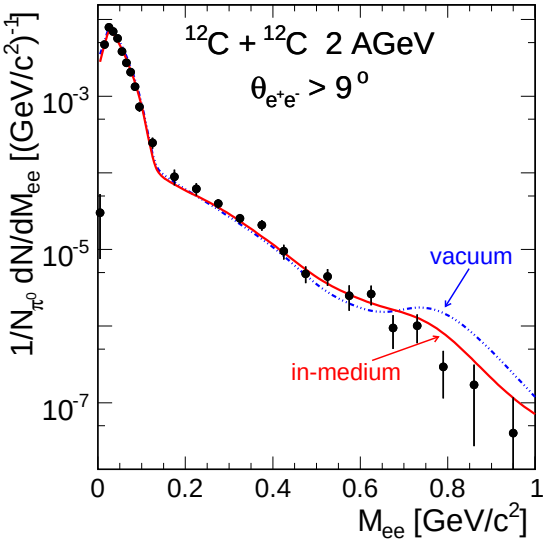

Figure 6.1: Comparison of the experimental invariant mass spectra with the new HSD calculations.

Chapter 7

Zusammenfassung

Das Studium der Eigenschaften von Hadronen, wie zum Beispiel effektive Massen, Zerfallsbreiten, elektromagnetische Formfaktoren, in Kernmaterie verschiedener Dichte und Anregungsenergie, ist von höchstem Interesse. Es wird erwartet, dass die partielle Restauration der chiralen Symmetrie der QCD bei endlichen Temperaturen oder Dichten der umgebenden Kernmaterie zu einer Reduktion der Massen von Vektor-Mesonen führt. Die QCD Summen-Regeln [1, 2] und hadronische Modelle [3-6] sagen vorher, dass sich die Masse und Resonanzbreite von Vektormesonen wie zum Beispiel ρ , ω und ϕ, in Kernmaterie messbar ändertn. Um solche Effekte zu untersuchen, sind die Vektormesonen bestens geeignet. Das sehr kurzlebige ρ-Meson (τ = 1,3 fm/c) zerfällt größtenteils noch im Kern oder einer vergleichausgedehnten Reaktionszone. Dies gilt teilweise auch für die langlebigeren ω- (τ = 23 fm/c) und ϕ- (τ = 44fm/c) Mesonen, deren Lebensdauer in Kernmaterie verkürzt sein kann.

Vektor-Mesonen lassen sich in Photonen-, Hadronen- und Schwerionen-induzierten Reaktionen erzeugen. Durch exklusive Messung ihrer Zerfallsprodukte lassen sich die oben genannten Effekte untersuchen. Da Photonen und Leptonen im Ausgangskanal nicht der starken Wechselwirkung unterliegen, sind sie bestens eignet, um den Zerfall von Teilchen in Kernmaterie zu untersuchen. Die Spektroskopien der direkten Photonen und Leptonen-Paare sind die vielversprechensten Werkzeuge für das Studium von Effekten in Kernmaterie.

Der HADES (High Acceptance Di-Electron Spectrometer) Detektor am Schwerionen-Synchroton (SIS) bei GSI ist ein Spekrometer der zweiten Generation und wurde dazu entwickelt, um leichte Vektor-Mesonen zu untersuchen, die in pp, pA und AA Stößen erzeugt werden. In Anbetracht der niedrigen Wahrscheinlichkeit für die Erzeugung nicht-trivialer Dileptonen waren die Hauptforderungen an seinen Aufbau: 1. hervorragende Trennung von Leptonen und Hadronen, 2. selektives Trigger System, 3. hohe Akzeptanz und Messung bei hohen Zählraten, 4. hohe Granularität zur Trennung bei hohen Teilchen-Multiplizitäten in Schwerionen-Reaktionen. und 5. gute Massenauflösung.

Das HADES-Spektrometer besteht aus folgenden Detektoren: einem Ringabbildenden Cherenkov Detektor (RICH) für den Nachweis von Elektronen dabei, aber blind gegenüber Hadronen, einem elektromagnetischen Pre-Shower Detektor und einer Flugzeitwand aus Plastikszintil-

latoren (TOF) zur Teilchenidentifizierung und Trennung von Hadronen und Leptonen. Die Spurrekonstruktion und die Impulsbestimmung der geladenen Teilchen erfolgt mit Hilfe von 4 Ebenen von Vieldraht-Kammern (MDC) und einem supra-leitenden Magneten bestehend aus 6 Spulen. Die Datenaufnahme wird in der ersten Stufe (LVL1) durch das schnelle Multiplizitätssignal der Flugzeitwand getriggert, in der zweiten Stufe (LVL2) durch die Kombination der elektronischen Bildverarbeitungseinheiten (IPUs) von RICH, Pre-Shower und TOF. Letzteres ermöglicht die Anreicherung von Leptonenpaaren im Datenstrom. Das HADES Spektrometer wurde in den letzten Jahren am Schwerionen-Synchroton SIS der GSI aufgebaut und getestet.

Die vorliegende Arbeit beschreibt ausführlich die Analyse und die abschließenden Ergebnisse der inklusiven Messung der Leptonenpaar-Produktion in C+C Stößen bei 2AGeV mit dem HADES Spektrometer. Die Resultate beruhen auf Ereignissen mit einer positiven LVL2-Trigger Entscheidung entsprechend einer Gesamtstatistik von 6,5 x 10^8 LVL1 Ereignissen. Die Elektron- und Positron-Kandidaten wurden selektiert durch die räumliche Korrelation von Treffern im RICH, den inneren MDC Kammern und im TOF oder den TOFino/Pre-Shower Detektoren. Um Hadronen zu unterdrücken, wurde zusätzlich ein Fenster auf die Geschwindigkeit β (v/c) gesetzt, sowie ein spezielles Verfahren zur Erkennung von Leptonen im Pre-Shower angewandt.

Die Zahl der positiv-geladenen Teilchen wird dabei stärker reduziert als die der negativ geladenen. Einer der Gründe dafür ist die Verunreinigung mit Protonen. Diese werden durch das Magnetfeld bevorzugt in den Pre-Shower Detektor abgelenkt, wo sie zusätzlich unterdrückt werden. Simulationen zeigen, dass die Reinheit von einzelnen Leptonen Spuren bei etwa 90%.

In der Analyse von Paaren werden die als Elektron und Positron identifizierten Spuren zu Paaren aus Teilchen gleicher Ladung, sowie Paaren von Teilchen ungleicher Ladung kombiniert. Die Gesamtzahl an Paaren ungleicher Ladung ($N^{tot}_{e^+e^-}$) besteht zum einen aus den interessanten Paaren mit korrelierten Teilchen ($S_{e^+e^-}$), als auch aus Paaren mit unkorrelierten Teilchen, die zum kombinatorischen Untergrund beitragen ($CB_{e^+e^-}$). Das Signal wird gebildet aus den Paaren, bei denen das e^+ und das e^- aus dem gleichen Vertex (Zerfall) stammen, während der Untergrund gebildet wird von Paaren, bei denen das e^+ und das e^- aus verschieden Zerfällen, also unkorrelierten Quellen, stammen. Die identifizierten Spuren einzelner Elektronen und Positronen werden kombiniert zu Paaren mit Teilchen entgegengesetzter Ladung (e^+e^-) und aus diesen wird die invariante Masse bestimmt:

$$M_{ee} = \frac{2}{c}\sqrt{p_{e^+}p_{e^-}}\sin\theta/2 \tag{7.1}$$

wobei p_{e^+}, p_{e^-} die rekonstruierten Impulse der Leptonen sind und θ der Öffnungswinkel zwischen den Richtungen der beiden Leptonenspuren. Externe γ Konversion ($\gamma \rightarrow e^+e^-$) und Dalitz-Zerfall von neutralen Pionen ($\pi^0 \rightarrow \gamma e^+e^-$) bilden den Hauptbestandteil an Paaren mit ungleicher Ladung. Solche Paare haben kleine Öffnungswinkel und bilden oft sich überlappende Spuren im MDC. Durch Bedingungen auf den Öffnungswinkel ($\theta > 9°$) und die Qualität der Spur-Rekonstruktion lassen sich diese Paare weitgehend unterdrücken. 4.14 (a) zeigt die resultierende Verteilung der invarianten Masse (offene Kreise), des Untergrundes (volle

Dreiecke) und des Signals (volle Kreise).

Für die Rekonstruktion des kombinatorischen Untergrundes wurden zwei verschiedene Methoden verwendet: im Massenbereich M_{ee} < 150 MeV/c^2 die Bildung von Paaren mit gleicher Ladung und im Massenbereich M_{ee} > 150 MeV/c^2 die sogenannte Event-Mixing Methode, bei der Paare ungleicher Ladung gebildet werden, die jedoch aus verschiedenen Ereignissen stammen. Abbildung 4.15 zeigt das so bestimmte experimentelle Signal zu Untergrund Verhältnis. Es ist im Massenbereich M_{ee} < 150 MeV/c^2 etwas größer als 10, im mittleren Massenbereich etwa 1 und größer 1 im Bereich M_{ee} > 600 MeV/c^2. Insgesamt wurden $\simeq$ 23000 Paare im Signal ($\simeq$ 2000 M_{ee} > 150 MeV/c^2) rekonstruiert.

Um die gemessene Verteilung mit theoretischen Vorhersagen vergleichen zu können, müssen die Daten bezüglich der Detektor- und Rekonstruktions-Ineffizienzen korrigiert werden. Für die Bestimmung der Rekonstruktions-Effizienz wurden in ^{12}C + ^{12}C Ereignisse die mit dem UrQMD Transportmodele gemeriest wurden, Leptonen Spuren eingebettet. Diese wurden mit gleichverteilten inversen Impulsen 1/p und isotroper Winkelverteilung erzeugt. Die Nachweiswahrscheinlichkeit wird daraus berechnet als Funktion der Ladung ($\varepsilon_{\pm}$), des Impulses (p), des Polar- (θ) und des Azimut-Winkels (ϕ). Sie berücksichtigt die Verluste bei der Leptonen-Erkennung und der Spur-Rekonstruktion. Die Daten wurden für jedes einzelne Leptonenpaar mit dem Wichtungsfaktor 1/$E_{\pm}$ korrigiert, wobei $E_{\pm}$=$\varepsilon_{+}\varepsilon_{-}$ bei den entsprechenden Impuls und Emissionswinkeln ist. Der kombinatorische Untergrund wurde in gleicher Weise behandelt und dann subtrahiert, um die mit der Nachweiswahrscheinlichkeit korrigierte Verteilung der Signale zu bestimmen. Die geometrische Akzeptanz des HADES Spektrometers für Paare wurde analog zur Paar-Effizienz als das Produkt der Akzeptanzen der beiden einzelnen Leptonen berechnet $A_{\pm}$(p,θ,ϕ).

Abbildung 4.20 zeigt die experimentelle, bezüglich der Nachweiswahrscheinlichkeit korrigierte Verteilung der invarianten Massen für C+C bei 2 AGeV. Die Daten werden verglichen mit dem PLUTO Cocktail A, bei dem nur der Zerfall freier π^0, η and ω Mesonen berücksichtigt wurde. Dieser Cocktail repräsentiert alle Beiträge nach dem Ausfreiren des Feuerballs. Der Dalitz-Zerfall von π^0 und η wurde bereits von der TAPS Kollaboration experimentell bestimmt. Für die Produktionsrate der ω-Mesonen wurde ein $m_{\perp}$ - Skalierungs-Ansatz verwendet. PLUTO ist ein schneller Event-Generator, der von einer thermischen Verteilung im Phasenraum ausgeht. Bei kleinen Massen (M_{ee} < 150 MeV/c^2) stimmt die experimentell bestimmte Zahl der Dileptonen gut mit den PLUTO-Resultaten überein. Im mittleren Massenbereich (150 MeV/c^2 < M_{ee} < 550 MeV/c^2) und bei höheren Massen (M_{ee} > 550 MeV/c^2) liegt dagegen die PLUTO-Verteilung deutlich unterhalb der experimentellen Daten. Ein solches Verhalten weist darauf hin, dass in diesem Massenbereich zusätzliche Komponenten beitragen, wie zum Beispiel der Zerfall von Resonanzen mit kurzer Lebensdauer, insbesondere des Δ(1232) und des ρ aus der Anregung in der frühen Phase des Stoßes. Um im PLUTO-Cocktail Paare aus dem $\Delta^{0(+)} \rightarrow Ne^+e^-$ Zerfall zu berücksichtigen, nehmen wir an, dass der Δ-Produktionsquerschnitt verknüpft ist mit dem des π^0. Wie schon für das wurde für das ein $m_{\perp}$-Skalierungs-Ansatz gewählt, der bei so breiten Teilchen (Γ = 150 MeV) den Anteil bei niedrigen Massen stark erhöht. Abbildung 4.8 zeigt den vollen PLUTO-Cocktail. Wie erwartet, erhöht sich im mittleren Massenbereich die Zahl der Dileptonen-Paare und insbesonders die

hohen Massen werder durch den Zweikörper-Zerfall von ρ-Mesonen populiert. Dennoch können die zusätzlichen Beiträge aus Resonanzen den Verlauf nicht vollständig beschreiben. Zur besseren Darstellung des Unterschiedes zeigt Abbildung 5.6 das Verhältnis der experimentellen Daten und des PLUTO-Cocktails. Zusätzlich zeigt die gestrichelte Linie das Verhältnis des vollen PLUTO-Cocktails B und des Cocktails A.

Eine zusätzliche Observable ist der transversale Impuls ($P_\perp$) des Paares. Abbildung 4.22 zeigt die Verteilung des transversalen Impulses für drei verschieden Massenbereiche. Bei kleinen invarianten Massen stimmen die experimentellen Daten gut mit den PLUTO Simulationen überein. Im mittleren und hohen Massenbereich sind die experimentellen Daten höher, zeigen allerdings keine starke Abhängigkeit von $P_\perp$.

Eine der Hauptschlussfolgerungen aus dem Vergleich mit dem PLUTO Event-Generator ist, dass dieses einfache Model die Dileptonenrate nicht vollständig beschreibt. Ein Vergleich mit komplexeren Transportmodellen ist daher notwendig. In der vorliegenden Arbeit werden die Daten auch mit verschiedenen, seit kurzer Zeit verfügbaren Transportmodellen (HSD, RQMD und UrQMD) verglichen.

Die vorliegenden Resultate erlauben es nicht, den von der DLS Kollaboration bei 1.04 AGeV gemessenen Überschuss an Paaren direkt zu verifizieren. Aus den DLS Daten und einem gefilterten PLUTO Cocktail bei der entsprechenden Energie ergibt sich ein uberschassfaktor F(1.04)=6.5$\pm$0.5(stat)$\pm$2.1(sys)) im η Massenbereich (0.15 GeV/c^2 < M+ee < 500 GeV/c^2). Analog wurde auch der Überschussfaktor F(2.0)=2.07$\pm$0.21(stat)$\pm$0.38(sys) aus den hier vorliegenden Daten bestimmt bei 2 AGeV. Er kann auf folgende Art definiert werden:

$$F(E) = \frac{Y_{tot}(E)}{Y_\eta(E)} = \frac{Y_{exc} + Y_\eta}{Y_\eta(E)} \tag{7.2}$$

Aus TAPS Messungen ist jedech bekannt, dass sich die inklusive η Produktion in C+C Stößen beim Übergang der Energie von 1.04 auf 2.0 AGeV um einen Faktor 13$\pm$3(stat) erhöht. Der Skalierungsfaktor für den Überschuss an Paaren $\frac{Y_{exc}(2.0)}{Y_{exc}(1.04)}$ lässt sich aus den Einzelfaktoren (F(2.0) und F(1.04)) berechnen. Daraus folgt:

$$\frac{Y_{exc}(2.0)}{Y_{exc}(1.04)} = 2.5 \pm 0.5(stat) \pm 1.5(sys) \tag{7.3}$$

Der Überschuss an Paaren ist vergleichbar mit der DLS Messung bei 1.04 AGeV, wenn man annimmt, dass die Skalierung mit der Energie ähnlich ist wie die der Pionen Produktion ($\frac{Y_{\pi^0}(2.0)}{Y_{\pi^0}(1.04)}$ = 2.3 $\pm$ 0.3(stat)). In naher Zukunft werden auch die von HADES gemessenen Daten für C+C bei 1.0 AGeV verfügbar sein, was dann einen direkten Vergleich mit den DLS Daten erlaubten wird.

Appendix A

The PLUTO event generator

The PLUTO even generator [78, 79] is an "experimentalist's" tool to simulate particle emission from hadronic reactions. Realistic models of the resonance populate on, hadronic and electromagnetic decays are implemented. The PLUTO hadronic cocktail provides a reference for comparison with the yield observed in AA collisions. The event generator uses vacuum spectral functions for any hadronic resonance. The spectral functions are calculated explicitly, and are subsequently used for sampling masses. In case of the long-lived particles (narrow masses) the mass is fixed at the pole mass and the energy E is sampled as a relativistic Boltzmann distribution:

$$\frac{dN}{dE} \propto Boltzmann(E) \propto \exp^{-\frac{E}{T}} \tag{A.1}$$

where E is the center of mass energy and T can be associated to the pion temperature at the pion freeze-out in heavy-ion collisions. It has been observed that pion spectra slightly deviate from a single Boltzmann distribution and are better fitted to a superposition of two Boltzmann distributions:

$$\frac{dN}{dE} = C_1 \exp^{-\frac{E}{T_1}} + C_2 \exp^{-\frac{E}{T_2}} \tag{A.2}$$

For the short-lived, broad resonances the energy E and mass M are sampled concurrently as:

$$\frac{d^2N}{dEdM} \propto Boltzmann(E) \cdot Breit - Wigner(M) \tag{A.3}$$

Table A.1 presents inverse slope parameters obtained from different experiments for the C+C system at the beam energy of 1 - 2 AGeV.

The simulation requires prior knowledge of the different particle multiplicities, the widths of all decays including di-electrons in the final state, and a description of decay kinematics for

E_{beam} (AGeV)	Particle	T_1 (MeV)	T_2 (MeV)
1	π^+, π^-	45 ± 3	62 ± 3
2	π^+, π^-	40 ± 3	86 ± 3

Table A.1: Inverse slope parameters for C+C at 1 and 2 AGeV energies [1].

all relevant particles. Events generated with PLUTO contain the decays of π^0, η, ω, ϕ, ρ and Δ. The cross section for the soft meson decay (π^0 Dalitz and η Dalitz) are known quite well for A+A collisions and measured by several experiments: TAPS, KAOS, FOPI. All other cross sections have been estimated with the m_T-scaling method.

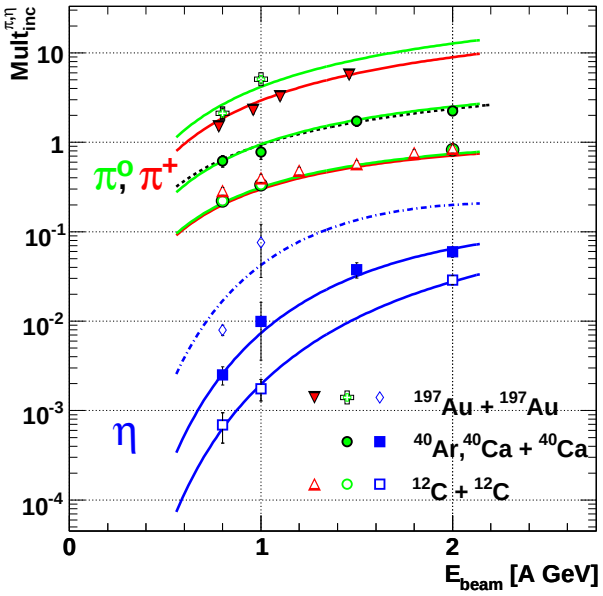

Figure A.1: Inclusive π and η production cross sections in the C+C, Au+Au and Ca+Ca systems as function of the bombarding energy. Symbols represent data [90, 99], solid lines are log-log polynomial fits to the data. The dashed curve corresponds to the $\sigma^{\pi^-}_{inc}$ parametrization of Nagamiya et al. [100].

To simulate events from A+A collisions PLUTO produces particles with momentum distributions corresponding to an equilibrated thermal source. Information about the degree of equilibration can be obtained from m_T-spectra:

$$m_T = \sqrt{p_T^2 + m^2} \tag{A.4}$$

where p_T is a transverse momentum of a particle with the mass m. The figure A.2 shows in a schematic way the $m_T - scaling$. This scaling allows to estimate production the cross sections of mesons, based on a universal curve which is measured for other mesons. The Δ production cross-section is directly related to the π^0 one and has been estimated to be a factor of 3/2 larger (assuming that all pions come from the Δ) [101].

The lower limit of each distribution represents the rest mass of the corresponding meson. The figure A.1 [88, 90] assumes the same slope of the distribution i.e. same temperature, as well for the π^0, η as for the ω meson.

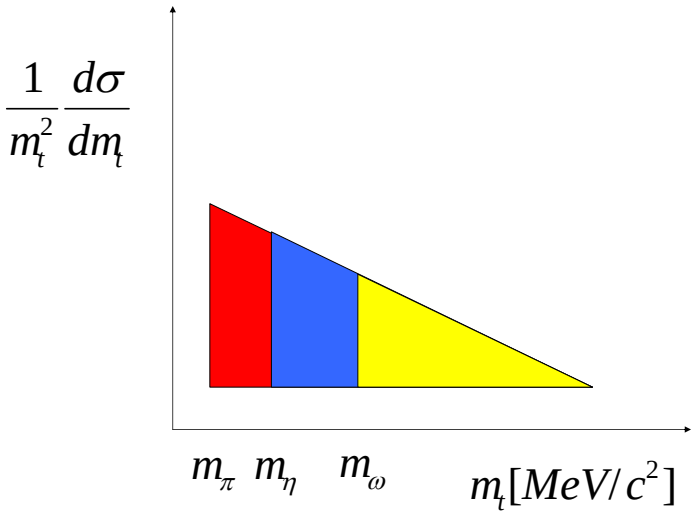

Figure A.2: Schematic view for the $m_T - scaling$

The inclusive production multiplicities of the π^0 and η have been measured by the TAPS collaboration via their 2 gamma decay mode. The TAPS measurement covered a wide range of the reactions with beam energies from 0.8 up to 2 GeV. Fig. A.1 shows the measured cross-sections (represented by the different symbols) and the polynomial fits to the data points (solid line).

The Boltzmann temperature T_B of the thermal sources in PLUTO has been chosen to be T_1 = 40 MeV and T_2 = 80MeV for the π^0 and T = 80MeV for all another sources. Figures A.3, A.4 show respectively the invariant mass, rapidity and transverse momentum distributions for the HADES data and PLUTO cocktail with different parametrization of the temperature.

The sensitivity of the accepted dilepton yield to various source parameterizations was studied in a broad range of parameters. It was found that the normalized pair spectra change by less than 10 $\%$ for a reasonable range of parameters. A similar test has been done for the isotropic and non-isotropic angular distributions and for the blast (for details see [102]).

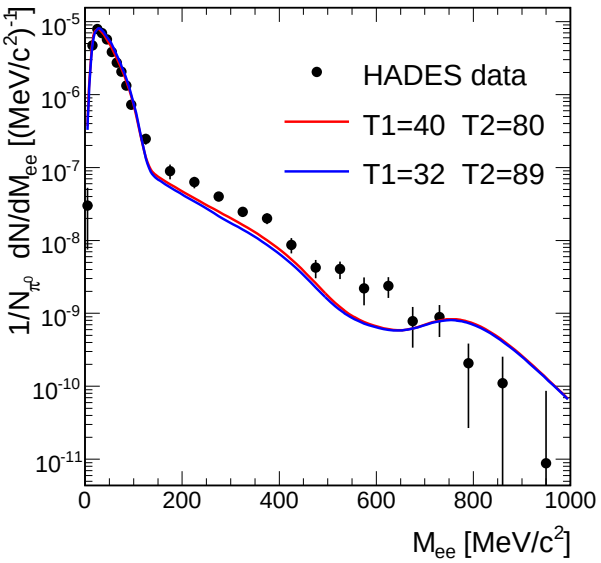

Figure A.3: Invariant mass spectrum for different parametrization.

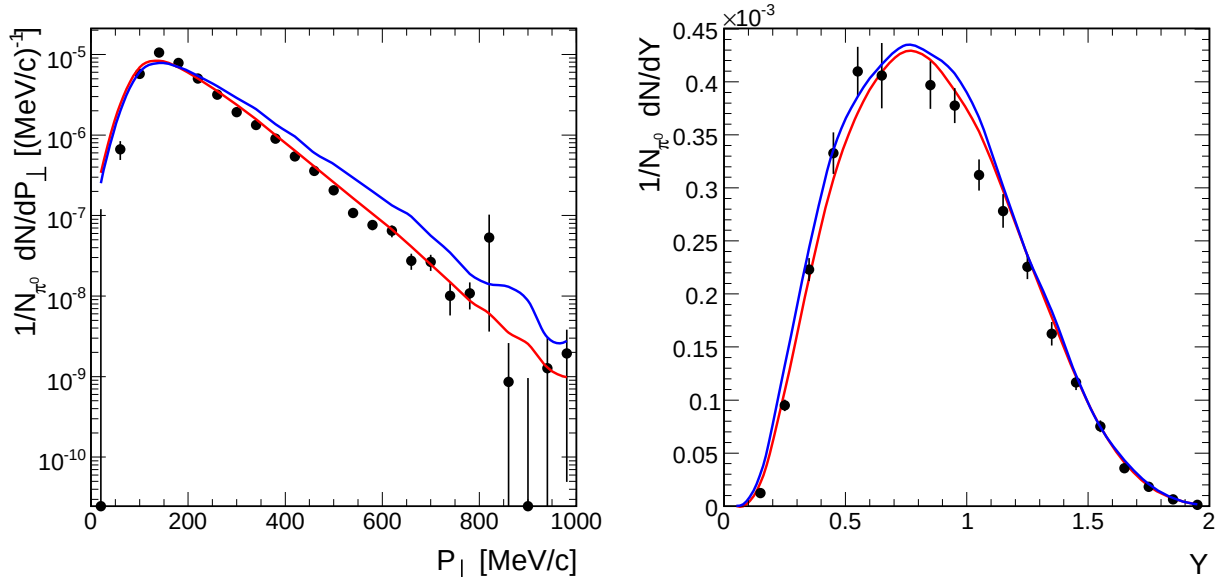

(a) (b)

Figure A.4: Transverse momentum (a) and rapidity (b) for different temperature parametrization (T1=40 MeV, T2=80MeV -red line and T1=32 MeV, T2=89 MeV - blue line)

Appendix B

Investigation of the systematic errors introduced by the reconstruction method

In order to validate the single-lepton efficiency matrices, several self consistency checks have been performed. Checks have been done with the PLUTO generator (PLUTO events have been put through the HGeant and reconstructed in the analysis described in chapters 3 and 4), where only signal pairs from all hadron sources and conversion inside the target and the RICH radiator were included. Fully reconstructed and background-subtracted unlike-sign signal pairs have been compared with the signal pairs from the PLUTO generator filtered with the HADES geometrical acceptance and folded with the reconstruction inefficiencies. If the purity of the signal after the full event reconstruction process is 100%, the two distributions should agree as function of any variable (i.e invariant mass, rapidity, transverse momentum and opening angle).

Due to the fact that the efficiency matrices were produced with UrQMD generated events, but the self-consistency checks were performed using the PLUTO events, an additional correction factors had to be taken into account: 6% for each single leg, due to the fact that hadrons can interfere with electron tracks during reconstruction and produce losses which are absent in case of the PLUTO simulation (it is applied only for PLUTO simulated events and is used only during the self consistency checks). The reason for choosing the PLUTO generator instead of UrQMD which is more realistic is the computing time. To process UrQMD events equivalent to statistics which is necessary to perform the analysis takes few months of the computing time. It has been proven that the results obtain with the PLUTO event generator are close to the UrQMD one.

Figure B.1 shows the comparison of the invariant mass, transverse momentum, rapidity and opening angle distributions for the two cases. As one can easily see, for the small mass region $M < 150 MeV/c^2$ we have a discrepancy which is directly connected to the small opening angles problem.

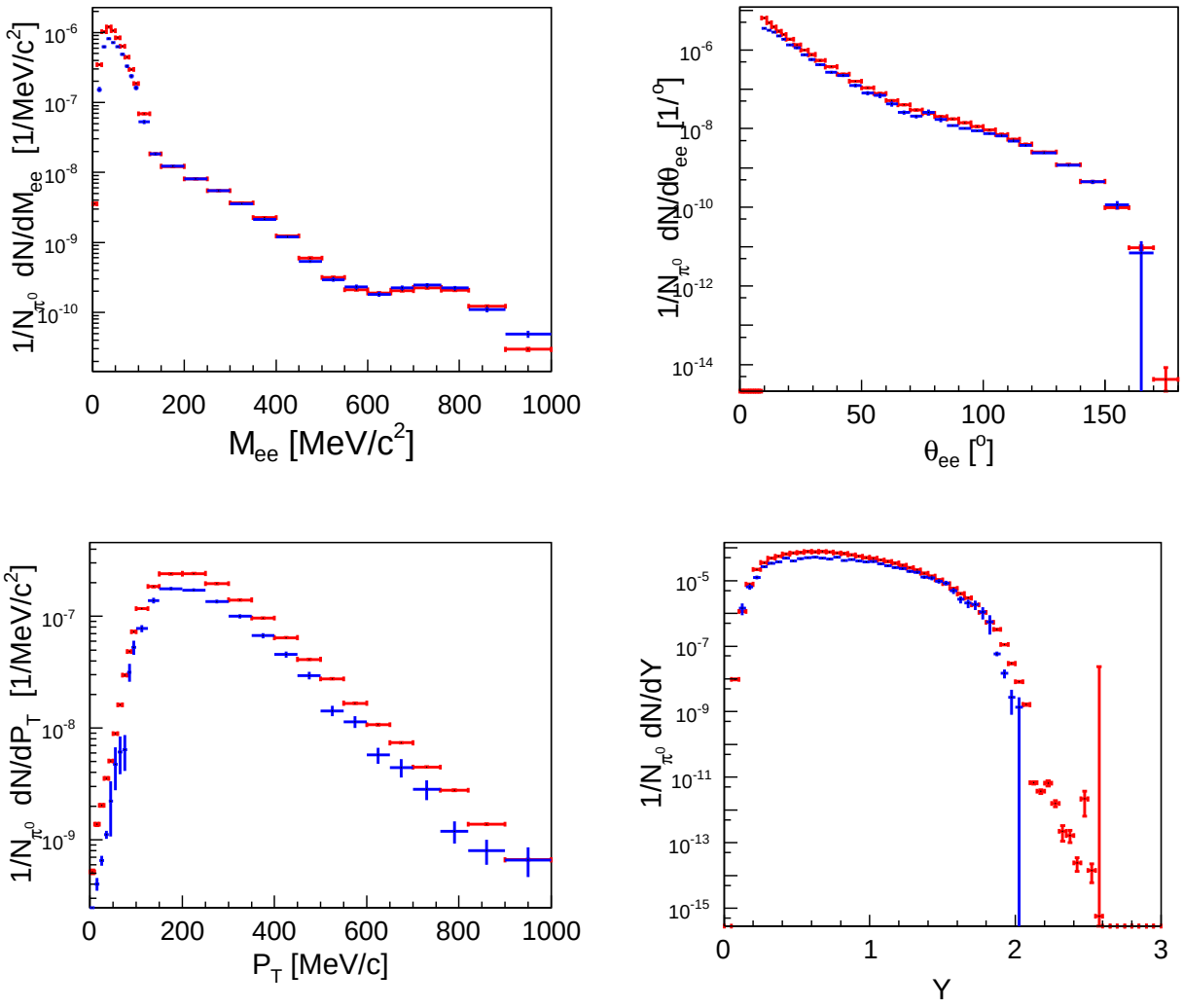

Figure B.1: Comparison of pair distributions obtained from the PLUTO events, filtered with the inefficiency and acceptance from the fully analyzed raw spectrum. Red line - reconstructed signal, blue - signal filtered with efficiency and acceptance.

Plotting the ratio of the opening angle of the signal pairs after applying an opening angle cut ($\theta > 9^o$, cutting in the sense of a direct cut) to the same distribution but after all pair cuts have been applied in the analysis (including recursive cutting), one can explore reductions of the signal due to the pair cuts. Since the only physics cut applied in the data analysis is the

opening angle cut, one would expect a constant (independent of the opening angle) ratio which only reflects (small) losses due to the presence of the C+C environment. In contrast to this assumption, one observes a dependance on angle up to the $\theta_{ee} \sim 40^o$ (see Fig. B.2).

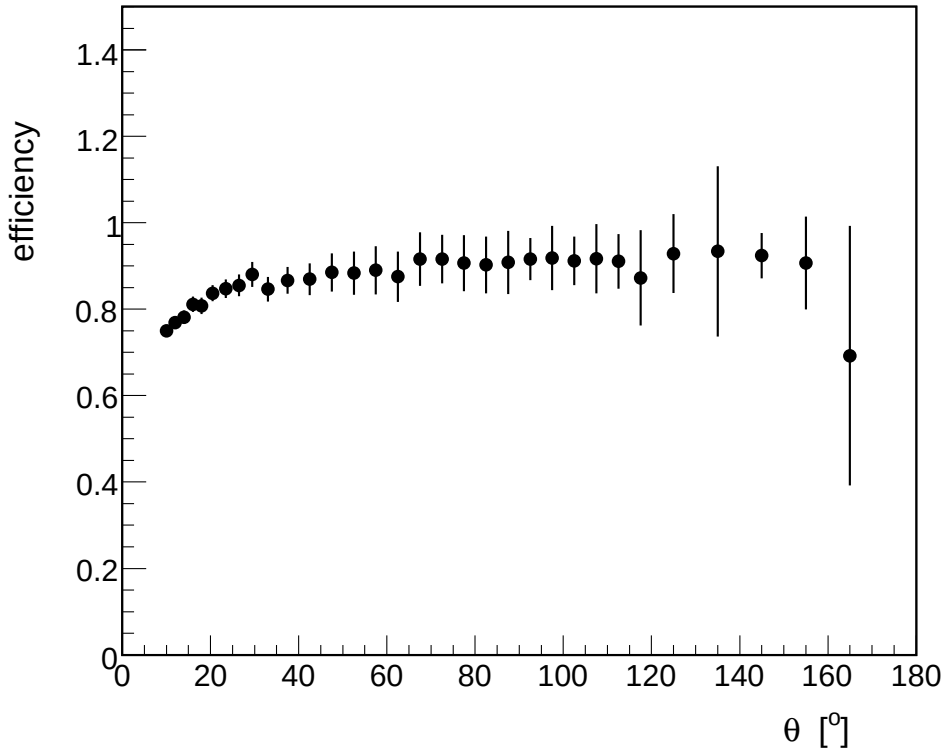

Figure B.2: Angular dependence of the signal pairs as a function of opening angle

To understand the reason for this kind of dependence several checks have been performed showing that the recursive way of cutting introduces this effect. It can be in principle traced to the appearance of ghost tracks created preferentially close to a true track. One could decide not to apply the recursive way of cutting, but this would reduce the signal-to-background ratio by a factor 2 at least.

Fig. 4.3 shows the signal-to-background ratio in the case when only direct cuts have been applied and in case of recursive way of cutting. In the recursive way of cutting the ratio in comparison to the direct case has significantly improved. In π^0 Dalitz region it is better by 2 - 4 times and by 2 - 3 above π^0. This fact convinced us to keep that particular removing strategy. In order to correct for correlations appearing in the pair efficiency on opening angle, a correction factor depending on the opening angle was introduced via:

$OA_{corr} = \frac{a}{\theta_{e^+e^-} * b+1} + c.$

After introducing all of the corrections, the self consistency check provides much better results. The remaining 20% discrepancy for the low invariant mass region is absorbed within our quoted systematical errors.

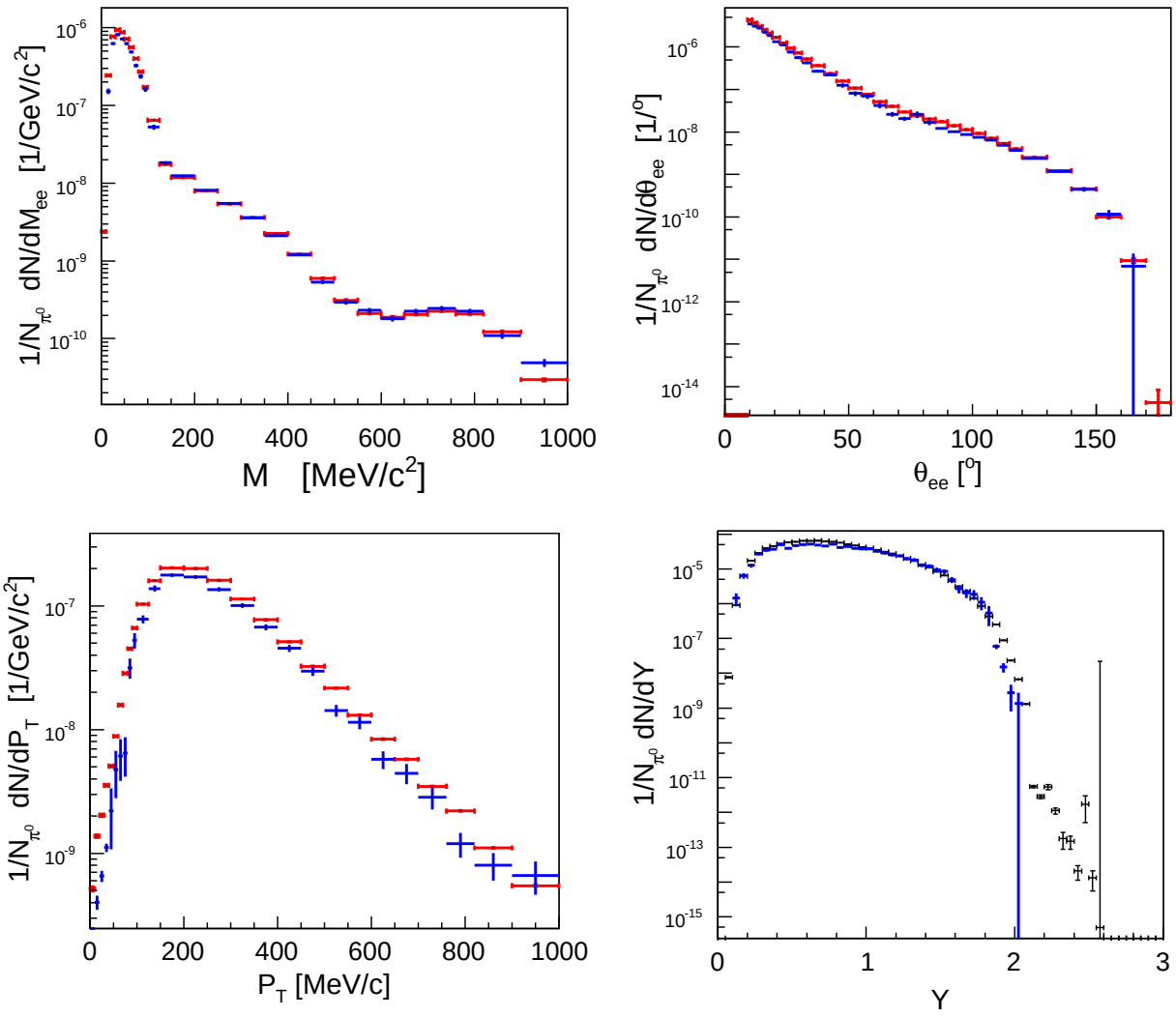

Figure B.3: Self consistency after all corrections have been applied

Fig. B.4 shows the ratio of the reconstructed and filtered with efficiency and acceptance signals.

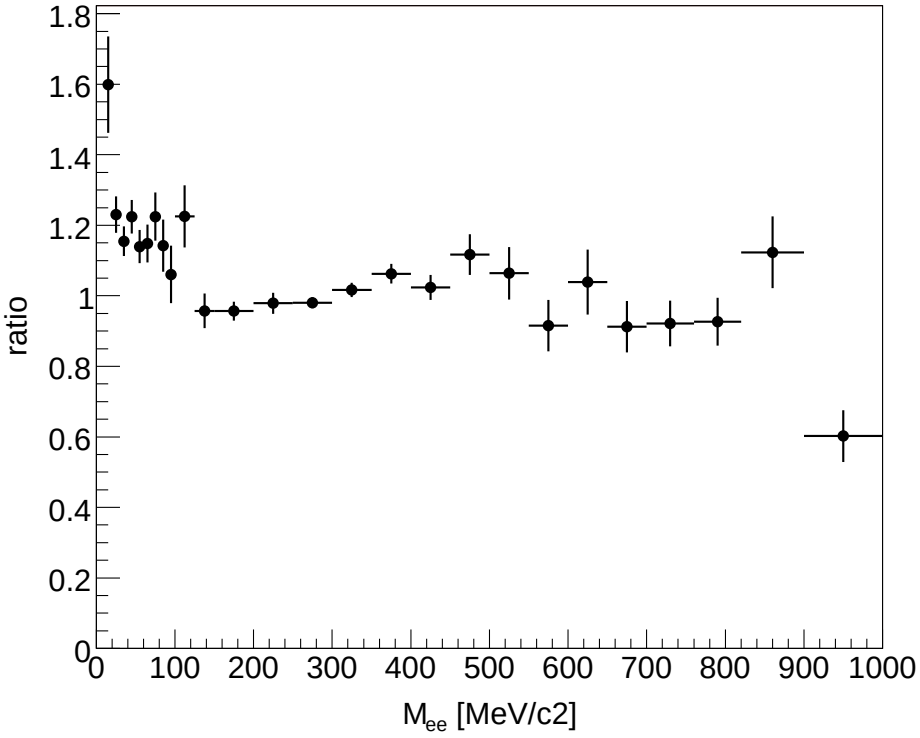

Figure B.4: Ratio of the reconstructed and filtered with acceptance and efficiency signals as a function of invariant mass.

Discrepancies which are visible in the $P_\perp$ distribution are directly connected with the low mass region. Applying cut M_{ee} > 150 MeV/c^2 gives as perfect agreement in this case distribution (for details see [103]).

Appendix C

Geometrical acceptance

The acceptance can be defined as a probability for a particle emitted in the collision to cross the active volumes of the spectrometer's detectors. This includes the effect of the particle's deflection in the magnetic field which depends on momentum. In order to make a simple estimation of the acceptance, the Monte Carlo method based on HGEANT has been used. Events with uniform distributions in p, ϕ and θ were generated and tracked with the HGEANT assuming a 100 $\%$ detector efficiency. Then the reconstructed distributions were compared with the original ones. By dividing the distributions obtained before and after the reconstruction process we get a matrix indicating what is the acceptance for each bin in p, ϕ and θ. The geometrical acceptance is a 3 dimensional matrix for different single particle species and polarities. The 3 dimensions have been chosen as momentum (p), polar angle (θ) and azimuthal angle (ϕ) in the laboratory system.

Fig. C.1 shows projections on momentum, azimuthal and polar angle axis as for electrons. One can see that on average the acceptance for electrons is around 80 $\%$.

For the given momentum, polar and azimuthal angles of the particle, the geometrical acceptance can be defined as:

$$Acc(p,\theta,\phi) = \frac{N_{acc}^{p,\theta,\phi}}{N_{tot}^{p,\theta,\phi}} \tag{C.1}$$

where $N_{tot}^{(p,\theta,\phi})$ and $N_{acc}^{p,\theta,\phi})$ are total number of tracks and tracks which have been detected in the HADES spectrometer, respectively.

Fig. C.2 shows the pair acceptance. The pair acceptance is rather flat and reflects the losses due to finite solid angle coverage. However, at low masses the acceptance strongly depends on transverse momentum. One can see that for low mass and low transverse momentum we have a hole in the acceptance. This fact is directly connected with the small opening angle cut applied in the analysis.

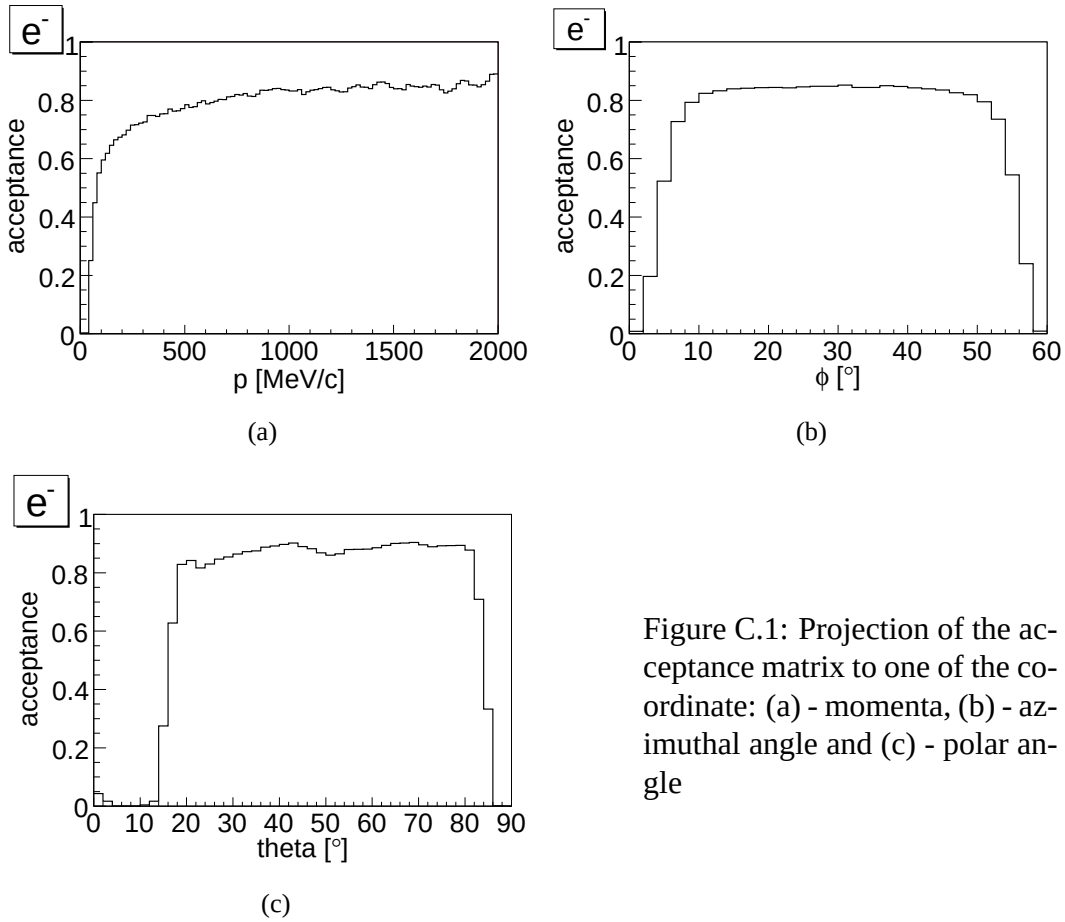

Figure C.1: Projection of the acceptance matrix to one of the coordinate: (a) - momenta, (b) - azimuthal angle and (c) - polar angle

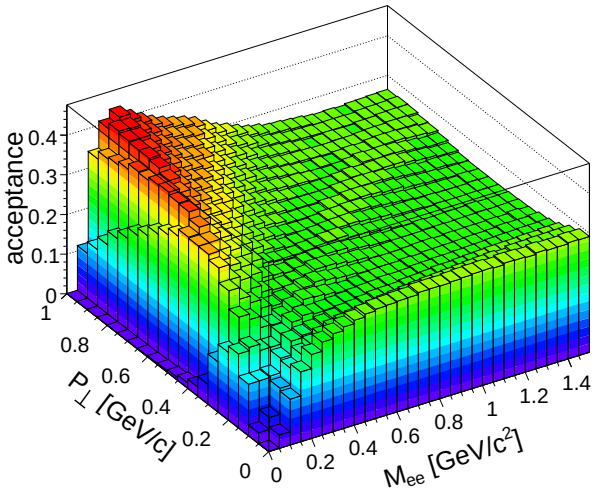

Figure C.2: Acceptance for e^+e^- pairs (with opening angle $\theta_{e^+e^-} > 9°$) of the HADES spectrometer as a function of their invariant mass and transverse momentum.

Appendix D

Study of the LVL2 trigger efficiency

Results presented in the thesis are based on the analysis made with events trigged by the LVL2 trigger (see section 2.8). The LVL2 trigger is operated online and accordingly it is not possible to recover events which have been discarded. Therefore, it is important to correctly estimate the efficiency of the trigger both for the single-electron and for the di-electron cases.

Since the interest of the HADES detector are e^+e^- pairs, and the LVL2 trigger is designed for the reconstruction of such a signature, the efficiency of the trigger could be defined as the fraction of e^+e^- pairs reconstructed with the LVL2 analysis. The dilepton efficiency therefore simply results from the single lepton efficiency ($\epsilon_{pair} = \epsilon^2_{single}$) folded with the propre phase-space. However the event efficiency of the trigger, which is the proper relevant quantity for the LVL2, since the trigger selects events, not leptons is clearly higher ($\epsilon_{pair} = 2\epsilon_{single} - \epsilon^2_{single}$) since the event is triggered even if the only one lepton is found (for details see, [69]).

The relative efficiency of LVL2 with respect to LVL1 can be estimated as the ratio between the number of leptons/dileptons found in LVL2 events and the number of leptons/dileptons found in LVL1 events.

To estimate the relative bias of the LVL2 trigger in the LVL1 data sample, the lepton and dilepton analysis was performed on LVL1 and LVL2 events and the shapes of following distributions were compared. Figures D.1 and D.2 show respectively the azimuthal and polar emission angle distributions separately for the electrons and positrons and for the Tofino/PreShower and Tof system.

	Tofino/PreShower	Tof
e^+	57 %	71 %
e^-	50 %	71 %

Table D.1: Second level efficiency for leptons in both systems.

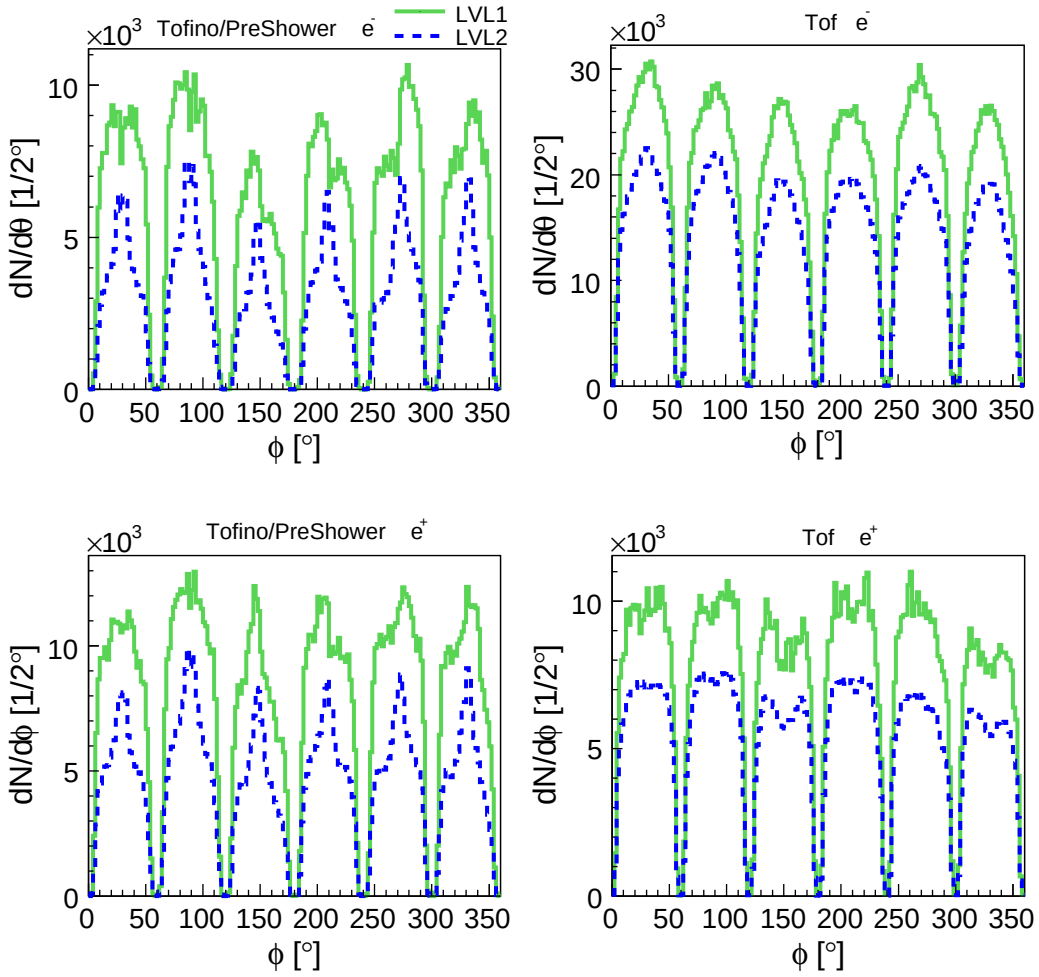

Figure D.1: Azimuthal emission angle distribution of leptons for LVL1 (green solid) and LVL2 (blue dashed) events.

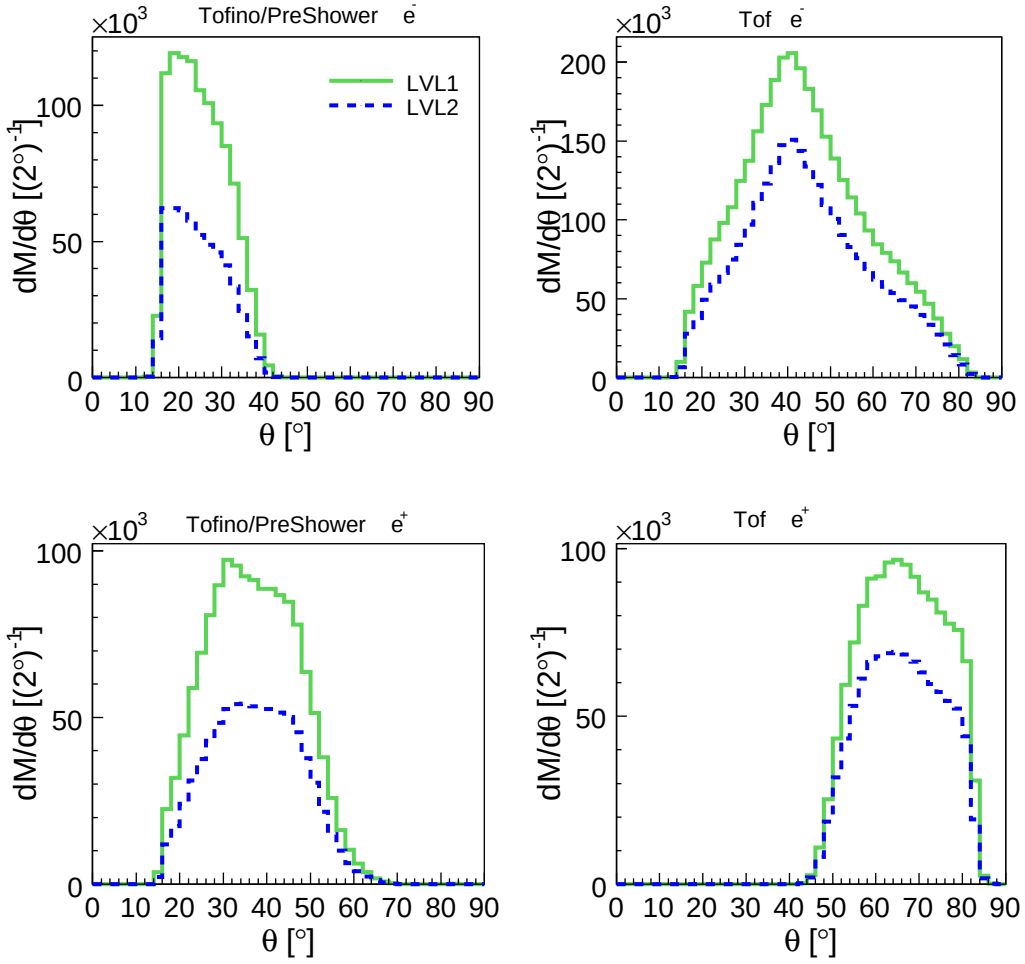

Figure D.2: Polar emission angle distribution of leptons for LVL1 (green solid) and LVL2 (blue dashed) events.

One can see that the efficiency is not equal for the two systems. It is about 20 % lower for the Tofino/PreShower than for the Tof. For the full HADES spectrometer, the efficiency of the LVL2 trigger was estimated as 65 % for single leptons.

Fig. D.3 shows the efficiency of the LVL2 trigger for like-sign and unlike-sign pairs as a function of the invariant mass, rapidity and transverse momentum (after all dilepton cuts). The efficiency for the dilepton was estimated to be on average 92 % ($\epsilon_{e^+e^+} \sim 93\%$, $\epsilon_{e^-e^-} \sim 89\%$,$\epsilon_{e^+e^-} \sim 96\%$), and has been taken into account during the normalization.

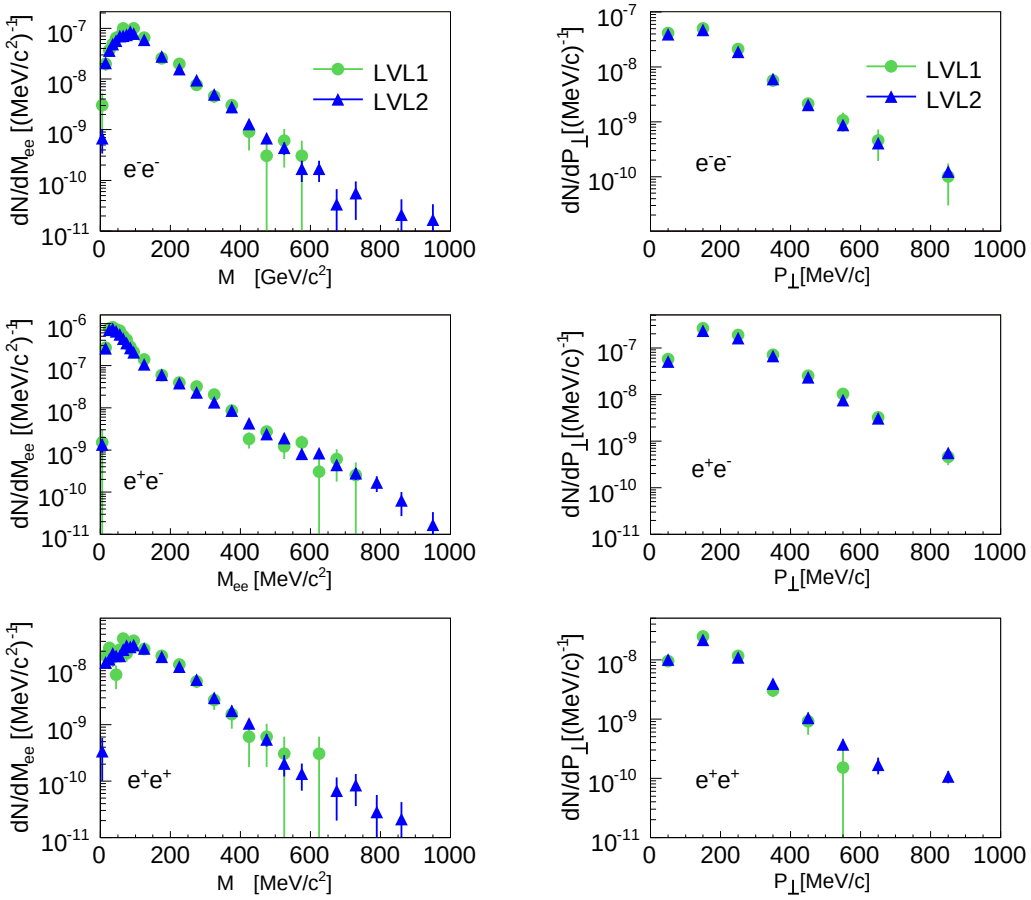

Figure D.3: Comparison of the invariant mass (a) and transverse momentum (b) distributions of the dileptons for LVL1 and LVL2 events.

In the LVL2 events an enhancement by a factor of 7.5 is found in the lepton yield and by a factor of 11 in the dilepton yield with respect to the LVL1 events.

Appendix E

Matching windows

As it was mentioned in chapter 3.4, the spatial correlation between RICH hits and inner MDC hits has been investigated for each sector of the HADES spectrometer as a function of the lepton momentum. Figures E.2 and E.3 show typical distributions of $\Delta\theta$, $\Delta\phi$, respectively.

The correlation signal is fitted with a Gaussian function (red line); the background is fitted with the sum of a second Gaussian (blue line) and a constant (magenta line). To get the proper modeling of the background, the random correlation between RICH and MDC hits of different sectors has been computed. From the fit to the uncorrelated background, one retrieves nearly identical standard deviation over full momentum range of around 3 °. With that knowledge the constrains for the background in the fit of the correlated RICH-MDC hits has been used.

Material	C_4F_10	Mirror	CKF Tank
Radiation length X_0 [cm]	3200	30	30
x(θ = 15^{circ}) [cm]	38.5	0.21	0.04
Θ_0(θ = 15^{circ})[°]	1.42	0.37	0.42
x(θ = 15^{circ}) [cm]	67.6	0.21	0.04
Θ_0(θ = 85^{circ})[°]	1.93	0.37	0.42

Table E.1: Radiation length and multiple scattering angle of the radiator components in the RICH detector for electrons with momentum p=0.5 GeV/c.

A part of the resolution, visible in the width of the signal Gaussian can be explained by the multiple scattering inside the RICH detector. In the present discussion only the multiple scattering taking place between the phone emission point and the MDC is of relevance. In table E.1 sources of the multiple scattering in the RICH detector are listed. The multiple scattering can be described with the following formula [104]:

$$\theta_0 = \frac{13.6MeV}{\beta cp} z \sqrt{\frac{x}{X_0}} [1 + 0.038 \ln(x/X_0)] \tag{E.1}$$

where p, β, and z are the momentum, velocity, and charge number of the incident particle, and x/X_0 is the thickness of a scattering medium in radiation lengths, c is the velocity of light.

Fig. E.1 shows the multiple scattering angle as a function of the lepton momenta for the different component of the RICH volume. The total multiple scattering changes like 1/p from 2° up to 0.32° for momenta between 100 and 600 MeV/c. To compare the result with the width of the Gaussian signal from the experiment, the detector resolution should be taken into account. The angular resolution of the MDC detector is much better than the RICH, and therefore can be neglected. Knowing the contribution of the multiple scattering for the high momenta leptons (600 MeV/c) one can determine the RICH resolution contributing to the total width of the signal Gaussian to be around 0.7°. The theoretical θ ($\sqrt{\theta_0^2 + \sigma_{RICH}^2}$) composed of the total multiple scattering (black line) and RICH resolution (green line) is plotted as a black dashed line. This can be directly compared with the width of the experimental signal represented by the red line.

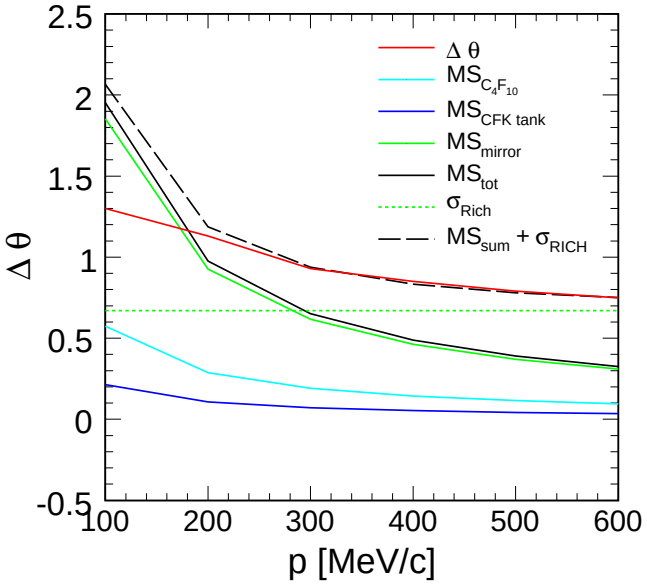

Figure E.1: Comparison of the theoretical and experimental widths of the signal.

For the momenta below 200 MeV/c experimentally deduced resolution diverges from the theoretical resolution. The reason for the discrepancy is understood and can be attributed to fitting procedure itself. The width of the background function and the signal function dominated by the multiple scattering of the low momenta particle can not be resolved by the fit in a proper way. The background fit cannot be fixed correctly because the range given to the correlation is limited. In addition the track reconstruction procedure selects systematically good tracks in the reconstruction.

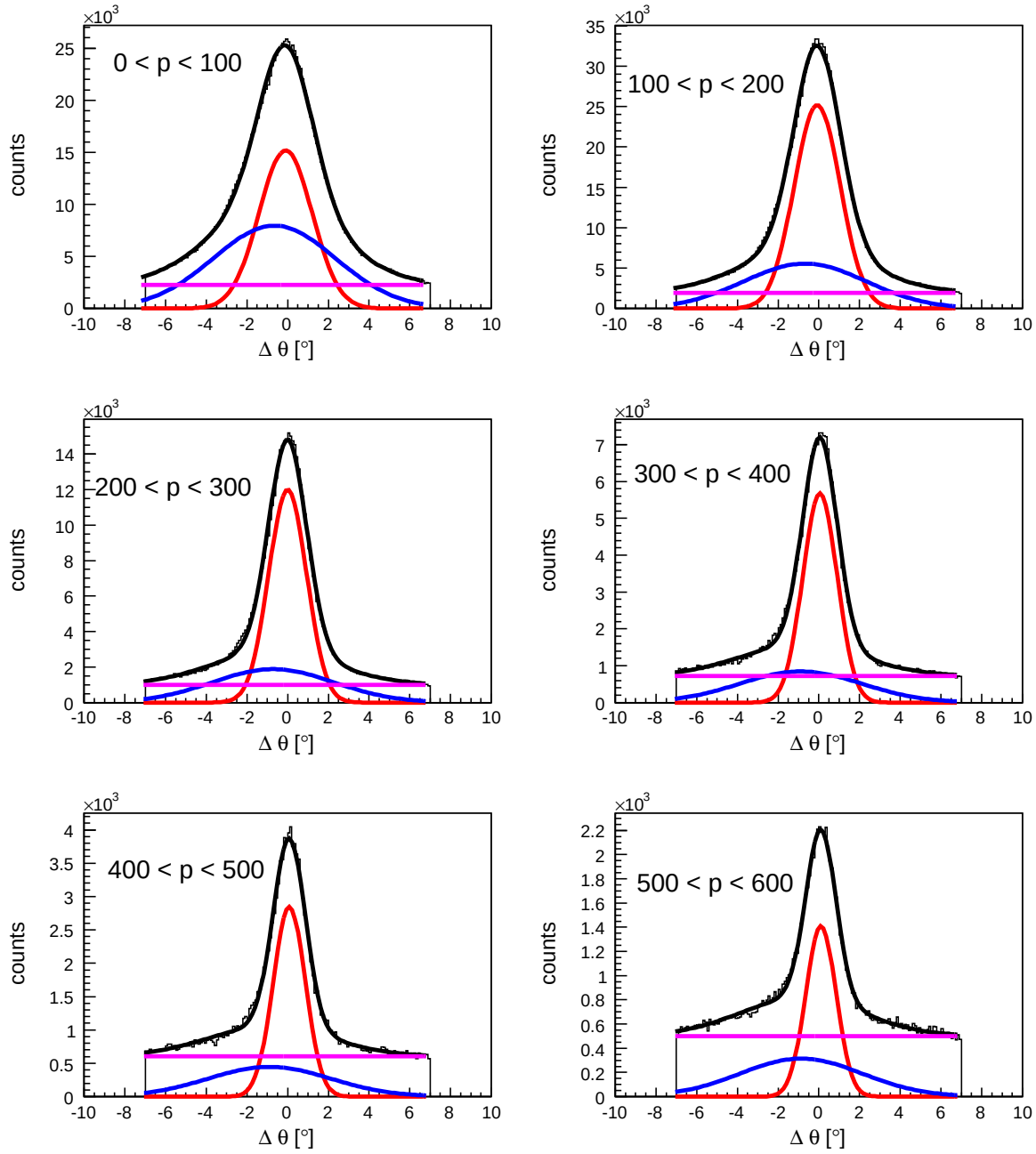

Figure E.2: Azimuthal correlation of RICH and inner MDC hits for all sectors together as a function of momentum

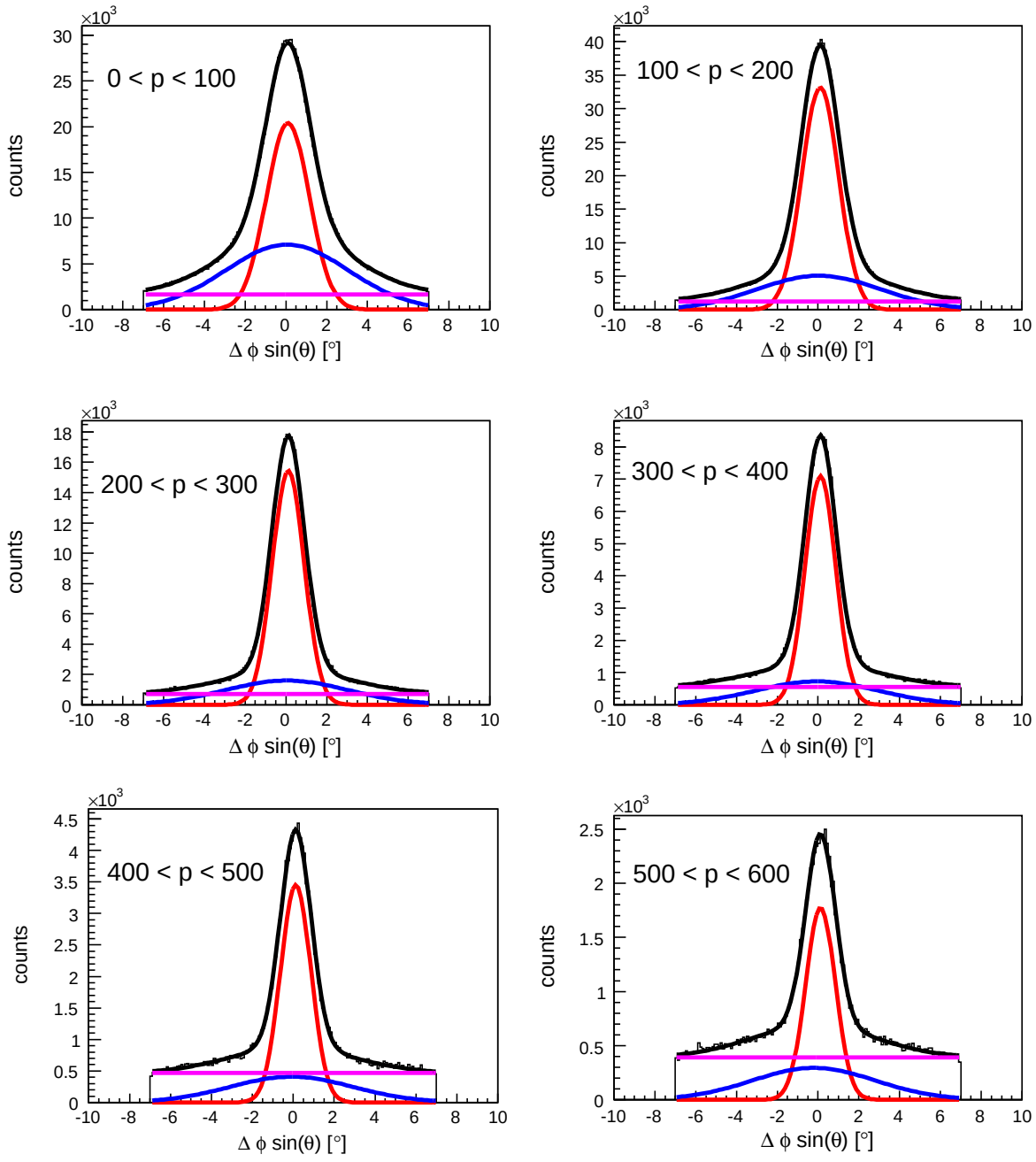

Figure E.3: Polar correlation of RICH and inner MDC hits for all sectors together as a function of momentum

Bibliography

[1] A. Föster. *Pionenproduction und thermische Konzepte in relativistischen Scherionenreactionen*. Master thesis, Technische Universität, Darmstadt, 1998. vi, 92

[2] P. Braun-Munzinger, J. Stachel. *J. Phys.*, A28:1971, 2002. 2

[3] P. Braun-Munzinger, J. Stachel, J. P. Wessel, N. Xu. *Phys. Lett*, B 365(1), 1996. 2

[4] P. Braun-Munzinger et al. *Nucl. Phys.*, A681:119, 1 2001. 1, 2

[5] P. Braun-Munzinger and J. Stachel. *Nucl. Phys.*, A 638:3, 1998. 1, 2

[6] P. Braun-Munzinger, J. Stachel, J. P. Wessel, N. Xu. *Phys. Lett.*, B344:43, 1995. 2

[7] P. Braun-Munzinger, I. Heppe, J. Stachel. *Phys. Lett.*, B465:15, 1999. 2

[8] R. Rapp and J. Wambach. Chiral symmetry restoration and dileptons in relativistic heavy-ion collisions. *Adv. Nucl. Phys.*, 1(25), 2000. 1, 3, 5, 6, 7

[9] V. Metag. *Acta Phys. Polonica*, B27:3175, 1996. 1

[10] V. Metag. *Prog. Part. Nucl. Phys.*, 30:75, 1993. 1

[11] W. Weis. *Nucl. Phys.*, A 610:35c–48c, 1996. 2

[12] G. E. Brown and M. Rho. Scaling effective Lagrangians in a dense medium. *Phys. Rev. Lett.*, 66:2720, 1991. 3, 5, 6, 7, 79

[13] V. Koch. Introduction to chiral symmetry. *LBNL Report 38000*, 1995. 3

[14] R. Rapp and J. Wambach. Theoretical interpretation of low-mass dileptons. *Nucl. Phys.*, A638:171c, 1998. 3

[15] T. Hatsuda and S. H. Lee. Qcd sum rules for vector mesons in nuclear medium. *Phys. Rev.*, C46:R34, 1992. 3, 9

[16] Y. Koike and A. Hayashigaki. *Prog. Theor. Phys.*, 98:631, 1997. 3

[17] M. Asakawa and C. M. Ko. *Nucl. Phys.*, A560:399, 1993. 3

[18] M. Asakawa and C. M. Ko. *Nucl. Phys.*, A572:737, 1994. 3

[19] S. Kling, N. Kaiser and W. Weise. Chiral Phase Transition In The SU(3) Nambu and Jona-Lasinio Model. *Phys. Lett.*, B 249:386–390, 1990. 3

[20] R. Rapp G. Chanfray and J. Wambach. *Nucl. Phys. A*, 617(472), 1997. 3, 6, 7

[21] B. Friman M. Herrmann and W. Norenberg. *Nucl. Phys.*, A560:411, 1993. 3

[22] K. Tsushima K. Saito and A. W. Thomas. *Nucl. Phys.*, A609:339, 1996. 3

[23] C. M. Shakin and W. D. Sun. *Phys. Rev.*, C 48:339, 1994. 3

[24] Sergey Yurevich. *Electron-Pair Production in 158 AGeV/c Pb-Au Collisions from CERES*. Phd thesis, Heidelberg, Germany, 2006. 5

[25] G. E. Brown and M. Rho. *Phys. Rept.*, 333:269, 1996. 5, 6, 79

[26] G.E.Brown and M.Rho. *Phys. Rept.*, 85:363, 2002. 5, 6, 7

[27] R. Rapp and H. van Hees. *Phys. Rev. Lett.*, 97(102301), 2006. 5, 6

[28] D. Adamova et al. (CERES Collaboration). *arXiv:hep-ex/0611022 v1*, 2006. 5

[29] R. Arnaldi et al. (NA60 Collaboration). First Measurement of the rho Spectral Function in High-Energy Nuclear Collisions. *Phys. Rev.*, 96:162302, 2006. 6

[30] M. Floris et al. (NA60 Collaboration). *nucl-ex/0606023*, 2006. 6

[31] R. Rapp G. Chanfray and J. Wambach. *Phys. Rev. Lett.*, 76(368), 1996. 6, 7

[32] T. Renk and J. Ruupert. Non-pertubative finite t broadening of the rho meson and dilepton emission in heavy ion-collisions. *Phys. Rev.*, C71, 2005. 6

[33] K. Dusling and D. Teany. *arXiv:hep-th/0604071*. 6

[34] G. Roche et al. (DLS Collaboration). First Observation of Dielectron Production At The Bevelac. *Phys. Rev. Lett.*, 61:1069–1072, 1988. 7

[35] G. Roche et al. (DLS Collaboration). Dielectron production in Ca+Ca collisions at 1-AGeV And 2-AGeV. *Phys. Lett.*, B229:228, 1989. 7

[36] R. Porter et al. Dielectron cross section measurements in nucleus nucleus reactions at 1.0 AGeV,. *Phys. Rev. Lett.*, 79:1229, 1997. 7, 8, 81

[37] E. Bratkovskaya et al. Dilepton production and m_t-scaling at BEVALAC/SIS energies. *Nucl. Phys.*, A634:168–189, 1998. 7, 8, 69, 74

[38] E. Bratkovskaya and C.M.Ko. Low-mass dileptons and dropping rho meson mass. *Phys. Lett.*, A445:265–270, 1999. 7

[39] C. Fuchs and A. Faessler. Dilepton and vector meson production in elementrary and heavy ion reactions. *Nucl. Phys.*, A755:499=502, 2005. 9

[40] D. Trnka et al. *Phys. Rev Lett.*, 94:192203, 2005. 9

[41] C. Djalali et al. *Contribution to the Quark Matter 2006 conferance*. 9

[42] M. Naruki et al. Experimental Signature of Medium Modification for rho and omega Mesons in the 12 GeV p+A Reaction. *Phys. Rev. Lett.*, 96(092301), 2006. 9

[43] K. Ozawa et al. Observation of $\rho//\omega$ Meson Modification in Nuclear Matter. *Phys. Rev. Letter*, 86:5019–5022, 2001. 9

[44] M. Sekimoto et al. *Nucl. Inst. & Meth. A.*, 516:390, 2004. 9

[45] K. Ozawa et al. Modification Of Vector Mesons In Nuclear Matter Measured In 12-GeV p+A Reaction At KEK-PS. *Nucl. Phys.*, pages 535–538, 2002. 9

[46] T. Hatsuda and S. H. Lee. QCD Sum Rules, Scattering Lenght and the Vector Meson Medium. *Phys. Rev.*, C52:3364, 1995. 9

[47] P. Salabura et al. HADES - a high acceptance di-electron spectrometer. *Nucl. Phys. B*, B(44):701, 1995. 12

[48] E. Berdermann et al. The Use of CVD Diamond for Heavy-Ion Detection. *Proc. of the 7th Int. Conf. on New Diamond Science Technology (ICNDST-7), Diamond and Related Materials, Hong Kong, July 2000*, 10:1770–1777, 2001. 14

[49] E. Gerdermann et al. Diamond detectors for Heavy-Ion Measurements. *Proc. of the XXXVI Intern. Winter Meeting on Nucl. Physics, Bormio*, 1998. 14

[50] M. Ploskon. Eksperymenty z diamentowymi detektorami na wiazkach ciezkich jonow przy relatywistycznych energiach. Master thesis, IF Uniwersytet Jagiellonski, Krakow, Poland, 2001. 14

[51] M. Bömer et al. Lepton identification with Csl based RICH of HADES. *Nucl. Inst. and Meth.*, A471:25–29, 2001. 15

[52] K. Zeitelhack et al. The hades rich detector. *Nucl. Inst. and Meth.*, A433:201, 1999. 15

[53] L. Fabietti. *Studies of the e+e- pair acceptance in the dilepton spectrometer HADES*. Phd thesis, Technische Universität München, 2003. 15, 32, 35

[54] P. A. Cherenkov. *Phys. Rev.*, 52:378, 1937. 15

[55] H. Bokemeyer et al. Development of low-mass drift chambers for the HADES spectrometer. *Nucl. Instrum. Meth.*, A 477:397–400, 2002. 16

[56] C. Garabatos et al. Optimisation of low-mass drift chambers for HADES. *Nucl. Instrum. Meth.*, A 412:38–46, 1998. 16

[57] C. Müntz et al. The HADES Tracking System. *Nucl. Instrum. Meth.*, A535:242–246, 2004. 16

[58] Thomas Bretz. Magnetfeldeigenschaften des Spektrometers HADES. Master thesis, Technische Universität München, 1999. 17, 18

[59] C. Agodi et al. The HADES Time-Of-Flight wall. *Nucl. Inst. and Meth*, A492:14–25, 2002. 18

[60] P. Tlusty et al. The Time Of Flight Detector For HADES. *Acta Politechnika*, pages 38–49, 1998. 18

[61] A. Godi et al. The HADES Time-Of-Flight wall. *Nucl. Instrum. Meth.*, A494:14–25, 2002. 20

[62] P. Fonte et al. Development of large area and of position-sensitive timing RPCs. *Nucl. Instr. Methods*, A(478):170–175, 2001. 20

[63] Diego Gonzalez-Diaz. Phd thesis, Santaigo, Spain, 2006. 20

[64] Marcin Jaskula. *Widma masowe lekkich mezonow uzyskane spektrometrem HADES*. Phd thesis, Jagiellonian University, Krakow, Poland, 2001. 20

[65] A. Balanda et al. Development of a fast pad readout system for the hades shower detector. *Nucl. Inst. and Meth*, A417:360, 2004. 20

[66] W. Przygoda. Badanie komor drutowych dla detektora spectrometru hades. Master thesis, IF Uniwersytet Jagiellonski, Krakow, Poland, 1995. 20

[67] A. Balanda et al. Performance of the Pre-Shower Detector for HADES. *Nucl. Instrum. Meth.*, 2003. 20

[68] M. Traxler. *Real-Time Dilepton Selection for the HADES Spectrometer*. Phd thesis, Justus-Liebig-Universität Gießen, 2001. 22, 23

[69] A. Toia. *Performance of the HADES Spectrometer for Dilepton Identification in the Reaction $C + C$ at $1 - 2\ AGeV$*. Phd thesis, Justus-Liebig-Universität Gießen, 2004. 22, 23, 102

[70] J. Lehnert. *Echtzeit-Mustererkennung zum Elektronennachweis mit einem RICH-Detektor in relativistischen Schwerionenkollisionen*. Phd thesis, Justus-Liebig-Universität Gießen, 2000. 22, 23

[71] M. Petri. *Entwicklung eines kombinierten Auslese- und Echtzeit-Triggersystems zum Nachweis von Elektronen/Positronen-Signaturen in einem elektromagnetischen Schauerdetektor*. Phd thesis, Justus-Liebig-Universität Gießen, 2000. 23

[72] HADES Trigger Homepage in Gießen. http://pcpig.physik.uni-giessen.de/hades/hades.htm, 2000. Internetangebot der HADES Kollaboration in Gießen. 23

[73] S. A. Bass et al. Microscopic models for ultrarelativistic heavy ion collisions. *Prog. Part. Nucl. Phys.*, 41:225–370, 1998. 24, 74

[74] HYDRA. HYDRA - HADES analysis package; http://www-hades.gsi.de/;. 28

[75] ROOT. An Object Oriented Data Analysis Framework; http://root.cern.ch/;. 28

[76] HGEANT. HADES Simulation Package; http://www-hades.gsi.de/;. 28

[77] GEANT. Detector Description and Simulation Tool; http://consult.cern.ch/writeup/geant/; Online User Guide. 28

[78] M. A. Kagarlis. Pluto++. *GSI Report*, 2000-2003. 29, 69, 91

[79] PLUTO. Pluto++, A Monte Carlo simulation tool for hadronic physics; http://www-hades.gsi.de/;. 29, 69, 91

[80] M. Sánchez-García. *Momentum reconstruction and pion production analysis in the HADES spectrometer at GSI*. Phd thesis, Universidade de Santiago de Compostela, 2003. 30, 31

[81] P. V. C. Hough. *Methods and means for recognition complex patterns*. U.S. Patern 3 069 654, Dec. 1962. 32

[82] W. Przygoda. *Identifikacja czastek e^+e^- za pomoca detectora RICH w spektometrze HADES*. Phd thesis, IF Uniwersytet Jagiellonski, Krakow, Poland, 2002. 32

[83] J. Pietraszko. *System pozycyjnie czulych komor drutowych do identifikacji elektronow i pozytronow w spektrometrze HADES*. Phd thesis, IF Uniwersytet Jagiellonski, Krakow, Poland, 2001. 36

[84] Jacek Otwinowski. *Pomiar widm par e+e- wyprodukowanych w zderzeniach $^{12}C^{12}C$ przy energii $E_{kin} \leq 2.0$ AGeV przy uzyciu spektrometra HADES*. Phd thesis, Jagiellonian University, Krakow, Poland, 2003. 36

[85] Anar Rustamov. *Exclusive η Meson Reconstruction in Proton-Proton Collisions at 2.2 GeV with HADES Spectrometer and High Resolution Tracking.* Phd thesis, Technische Universität, Darmstadt, 2006. 47

[86] M. A. Gunar Hering. *Dielectron production in heavy ion collisions at 158 GeV/c per nucleon*. Phd thesis, Technical University, Germany, 2001. 52

[87] J. Bielčik. *Dilepton spectroscopy with HADES*. Phd thesis, Fachbereich Physik, Technische Universität Darmstadt, Darmstadt, 2004. 59

[88] R. Holzmann et al. Contribution of π^0 and η-dalitz decays to the dilepton invariant-mass spectrum in 1 agev heavy-ion collisions. *Phys. Rev.*, C56:2920–2923, 1997. 68, 69, 83, 93

[89] C. Sturm et al. *Phys. Rev. Lett.*, 86(39), 2001. 68

[90] R. Averbeck et al. Production of π^0 and η mesons in carbon-induced relativistic heavy-ion collisions. *Z. Phys.*, A359:65–73, 1997. 69, 83, 92, 93

[91] D. Schumacher. Theoretical Analysis of Dilepton Spectra in Heavy Ion Collisions at GSI-FAIR Energies. *Acta Phys. Hung.*, A 19/1, 2004. 74

[92] URQMD. The UrQMD Collaboration; http://www.th.physik.uni-frankfurt.de/ urqmd/;. 74

[93] M. Bleicher et al. Relativistic Hadron-Hadron Collisions and the Ultra-Relativistic Quantum Molecular Dynamics Model (UrQMD). *J. Phys.*, G25:1859–1896, 1999. 74

[94] C. Fuchs and A. Faessler. Dilepton production in elementary and in heavy ion reactions. *Prog. Part. Nucl. Phys.*, 53:59–75, 2004. 74, 79

[95] M. D. Cozma et al. Dilepton production at HADES: theoretical predictions. *nucl-th/0601059*, 2006. 76, 79

[96] G. Agakichiev et al. (HADES collaboration). Dielectron production in ^{12}C^{12}C collisions at 2 AGeV with HADES. *Phys. Rev. Lett.*, 98(052302), 2007. 79, 85

[97] E. Bratkovskaya. e^+e^- production in pA reaction at SIS energies. *Nucl. Phys.*, A 696:761–787, 2001. 81

[98] L. P. Kaptari B. Kaempfer. *Nucl. Phys.*, A764:338, 2006. 86

[99] R. Averbeck et al. *Phys. Rev.*, C67:024903, 2003. 92

[100] E. Moeller et al. S. Nagamiya, M.C. Lemaire. *Phys. Rev.*, C24:971, 1981. 92

[101] S. A. Bass et al. *Phys. Rev.*, C1995:3343, 1995. 92

[102] PLUTO. HADES analysis package; http://hades-wiki.gsi.de/cgi-bin/view/SimAna/PLUTOINFO;. 93

[103] EFF. http://hades-wiki.gsi.de/cgi-bin/view/SimAna/Selfconsistencycheck. 99

[104] S. Eidelman et al. *Phys. Lett.*, B 592(1), 2004. 106

Lebenslauf

Malgorzata Sudoł

Verdistrasse 33
64291 Darmstadt

Geburtsdatum:	27. Februar 1977
Geburtsort:	Stalowa Wola, Polen

1984-1992	Besuch der Grundschule N.10 in Stalowa Wola, Polen
1992-1996	Besuch der Oberstufe mit phys. math. Schwerpunkt der "Liceum Ogolnoksztalcace" in Stalowa Wola, Polen
May 1996	Abitur
1996	Beginn des Studiums an der "University of Maria Curie Sklodowska"
1999-2001	Anfertigung der Diplomarbeit mit dem Titel: "Emisja nucleonów z jader atomowych" bei Dr. hab Andrzej Baran
2001	Master of Physics (University of Maria Curie Sklodowska)
seit 2001	Doktorand am Institut für Kernphysik der Johann Wolfgang Goethe-Universität Frankfurt und an der Gesellschaft für Schwerionenforschung (GSI) bei Prof. Joachim Stroth

Acknowledgements

I dedicate this PhD to all the people who believed in me to the end.

My very special thanks I would like to express to my supervisor Prof. Dr. Joachim Stroth and to Dr. Romain Holzmann, who introduced me into the field of experimental nuclear physics and guided my work during all those PhD years. Their very broad experience, help and suggestions were absolutely crucial for me in carrying out this work. Thank you very much, both of you, to be brave and patient enough to read and correct this work from the very earlier stage.

I would like to acknowledge the debt i owe to my colleagues from GSI, people of the HADES collaboration: Yvonne Pachmayer, Tetyana Galatyuk , Dr. Jochen Markert, Dr. Wolfgang König, Dr. Jerzy Pietraszko, Dr. Christian Münz, Alexander Schmah, Dr. Peter Zumbruch and Simon Lang.

Yvonne, thank you very much for "sharing" bad with me every time we were together on conferences, collaboration meetings and so on. I hope we will continue this for longer time.

I would like to thank Dr. Ilse König for sharing office with me, and for her patience during my long conversations in polish by phone.

I would like to say many thanks to the polish part of the HADES collaboration, especially to Dr. Piotr Salabura, Dr. Tomasz Wojcik, Dr. Jacek Otwinowski and Dr. Witold Przygoda for their help in work and many discussions about the analysis. Marcin Wisniowski and Radek Trebacz, thank you very much for dropping my presents to my sister in Poland.

For friendly environment and for their great help i would like to thank Dr. Thomas Eberl and Dr. Laura Fabbietti and all others from Munich part of collaboration.

For truly happy time spend during these years in Germany I am very grateful to Monika Rebisz, Michal Pomorski, Renata Piromalli, Katarzyna i Zbigniew Tyminscy, Stanislaw Taschenov, Alberto Cribeiro, Giogios Tsiledakis, Juan Sabin, Jose Javier Valiente Dobon and many other people. Together with you i really discovered a new definition of friendship. Thank you for being enough patient to be my friend.

On the end i would like to thanks parents, sister and brothers for the support during all those years i spend out of our home.